WP 5 Project Deliverable D5.1

CFD Simulations of Fire Hazards in the Mont Blanc and Gleinalm Tunnel

Project Number	IST-2000-29266
Project Title	Virtual Real Time Fire Emergency Simulator
Deliverable Type	Report
Deliverable Class	Internal

Deliverable Number	D5.1
Title of Deliverable	CFD Simulations of Fire Hazards in the Mont Blanc and Gleinalm Tunnel
Nature of the Deliverable	Confidential
Contributing WPs	-
Contractual Date of Delivery	October 1st, 2002
Actual Date of Delivery	October 1st, 2002
URL	www.virtualfires.org
Authors	Wilhelm Brandstätter (CD) Emanuel Mawa-Isaac (CD) Christian Redl (CD)
Contact Details	Institute for Structural Analysis / SiTu Research Univ. Prof. Dipl.-Ing. Dr. techn. Gernot Beer Lessingstrasse 25/II 8010 Graz / Austria Tel.: +43 316 8736180 Fax: +43 316 8736185 Email: gernot.beer@ifb.tu-graz.ac.at

Abstract	A priori computations of fire hazards in two alpine tunnels have been performed. The objective was to illustrate the influence of different ventilation system operating conditions on flame and smoke propagation behaviour. A database containing the results of all computations has been made available.
Keywords	CFD, Simulations, Tunnel Fire

Contents

1. INTRODUCTION

As part of Workpackage 5 of Virtualfires a priori computations of fire hazards in two alpine tunnels have been performed. Various anticipated heat loads ranging from a single passenger car fire up to a tanker disaster have been investigated for characteristic sections of the Mont Blanc tunnel (France) and the Gleinalm tunnel (Austria) geometries. The objective was to illustrate the influence of different ventilation system operating conditions on flame and smoke propagation behaviour.

A database containing the results of all computations is now available to the project partners responsible for the visualisation part of Virtualfires. This document shall give additional information concerning the underlying computational models and a detailed discussion of the results for various fire hazard scenarios is presented. All results have been obtained using the commercial flow solver FLUENT [1].

In what follows first the underlying mathematical framework and the numerical method used to solve the fundamental conservation equations system is presented. Thereafter all the information relevant for setting up the two tunnel simulations is given.

2. MATHEMATICAL FRAMEWORK

2.1 Governing Equations

The behaviour of continuum (both solid and fluid) is governed by the so-called transport equations based on the following basic laws of physics expressing balance (conservation) of:

- mass,
- momentum (Newton's second law) and
- energy (First law of thermodynamics)

The preferred way of writing equations expressing these laws is in differential form valid for an arbitrary point within the continuum:

$$\frac{\partial \rho}{\partial t} + \frac{\partial}{\partial x_j}\left(\rho u_j\right) = 0 \tag{1}$$

$$\frac{\partial \rho c_l}{\partial t} + \frac{\partial}{\partial x_j}\left(\rho u_j c_l\right) = \frac{\partial}{\partial x_j}\left[D_l \frac{\partial c_l}{\partial x_j}\right] + S_{c_l} \tag{2}$$

$$\frac{\partial \rho u_i}{\partial t} + \frac{\partial}{\partial x_j}\left(\rho u_j u_i\right) = -\frac{\partial p}{\partial x_i} + \frac{\partial}{\partial x_j}\left[\mu\left(\frac{\partial u_i}{\partial x_j} + \frac{\partial u_j}{\partial x_i}\right) - \frac{2}{3}\mu \frac{\partial u_m}{\partial x_m}\delta_{ij}\right] + \rho g_i \tag{3}$$

$$\frac{\partial \rho h}{\partial t} + \frac{\partial}{\partial x_j}\left(\rho u_j h\right) = \frac{\partial}{\partial x_j}\left[\frac{\lambda}{C_P}\frac{\partial h}{\partial x_j}\right] + \frac{\partial p}{\partial t} \tag{4}$$

u_i is the velocity in direction x_i; ρ is density; p is pressure; g_i is the component of the gravitational acceleration vector in direction x_i; μ, D_l and λ are viscosity, diffusion coefficient of species l and heat conductivity respectively. S_{c_l} is the species source or sink.

In the case when the continuum is a mixture of various species:

- which are mixed at the molecular level
- which share the same velocity, pressure and temperature fields, and
- in which the mass transfer between phases takes place by convection and diffusion

the balance equation for the lth species concentration c_l or mass fraction defined as the ratio of the mass of the lth species m_l to the mass of the mixture m at a point

$$\mathbf{c_l} = \frac{\mathbf{m_l}}{\mathbf{m}} \tag{5}$$

has to be solved. Since from the definition of mass fractions (5) follows, that

$$\sum_{\mathbf{i}=0}^{\mathbf{N}} \mathbf{c_l} = 1 \tag{6}$$

it is not necessary to solve transport equations (2) for all the species. The species labelled by 0 is called *background* or *carrier fluid* and transport equations (2) are solved for the mass fractions of the *additional species* (labelled from 1 to N).

Finally the total enthalpy is defined by:

$$\mathbf{h} = \mathbf{C_p T} + \frac{1}{2}\mathbf{u_i^2} \tag{7}$$

In this equation $\mathbf{C_p}$ represents the specific heat at constant pressure and $\mathbf{T}$ is the temperature.

Apart from the assumption, that the dissipation of kinetic energy into heat can be ignored for low Mach number flows, the above equations contain no approximations.

2.2 Turbulence Modelling

Most engineering fluid flows are in a particular state of continuous instability, called turbulence, and can be said to be steady on an average basis only, since small scale, high frequency fluctuations of all the flow quantities, in both space and time, are always present. A flow exhibiting these macroscopic fluctuations is called *turbulent flow.* Otherwise, a well ordered flow, free of macroscopic fluctuations, is called *laminar.*

The turbulent flow is well described by the above equations. However, their numerical solution (*direct numerical simulation*, DNS) requires a mesh with spacing smaller than the length scale of the smallest turbulent eddies, and time steps smaller than the smallest time scale of turbulent fluctuations. This requires computer resources, which are not available at the present state computer technology (except for low Reynolds number flows in very simple geometries).

Alternatives are *large eddy simulation* (LES), in which only the largest unsteady motions are resolved and the rest is modelled, and the solution of *Reynolds averaged Navier-Stokes* (RANS) equations, where all turbulent effects on the mean flow are modelled as functions of mean fluid flow quantities. LES is just beginning to be used for complex flows; it is also very costly and the solution of engineering problems will have to rely on solving RANS equations for a long time in the future, especially when the flows can be considered statistically steady.

For the above reasons RANS equations have been used for the flow simulations performed within this study.

2.2.1 Reynolds averaged Navier-Stokes Equations

The RANS equations are obtained by using a statistical description of turbulent motion, formulated in terms of averaged quantities. One such description uses the Reynolds averaging, whereby each dependent variable is expressed as the sum of its mean, or time-averaged value $\overline{\phi}$, and fluctuating component ϕ'.

$$\phi = \overline{\phi} + \phi', \tag{8}$$

where

$$\overline{\phi}(\mathbf{r},\mathbf{t}) = \frac{1}{\tau}\int_{-\frac{\tau}{2}}^{\frac{\tau}{2}} \phi\,(\mathbf{r},\mathbf{t}+\xi)\mathbf{d}\xi, \tag{9}$$

and the time interval τ is large enough with respect to the time scale λ_t of the turbulent fluctuations, but small with respect to the scale of other time dependent effects (see Figure 1). This practice is termed "ensemble-averaging".

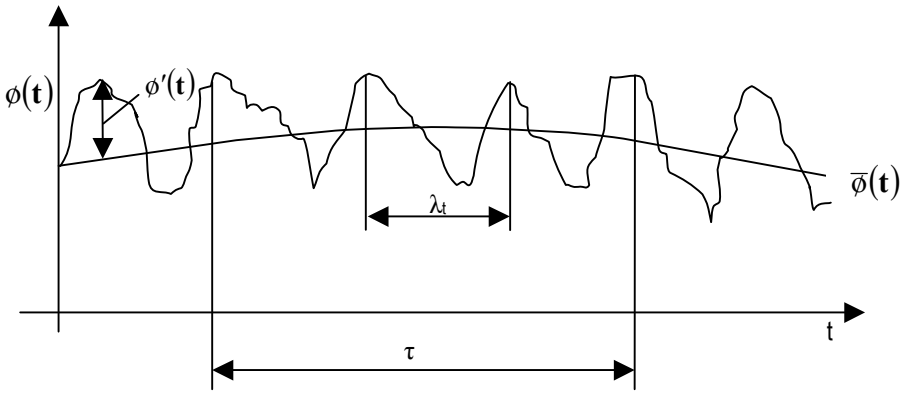

Figure 1: *Ensemble averaging procedure*

Applied to the governing equations of Section 2.1; the following equations for mass, energy and momentum balance in turbulent flows are obtained:

$$\frac{\partial\overline{\rho}}{\partial\mathbf{t}} + \frac{\partial}{\partial\mathbf{x_j}}\left(\overline{\rho}\,\overline{\mathbf{u}}_\mathbf{j}\right) = 0 \tag{10}$$

$$\frac{\partial\overline{\rho}\,\overline{\mathbf{c}}_\mathbf{l}}{\partial\mathbf{t}} + \frac{\partial}{\partial\mathbf{x_j}}\left(\rho\overline{\mathbf{u}}_\mathbf{j}\overline{\mathbf{c}}_\mathbf{l}\right) = \frac{\partial}{\partial\mathbf{x_j}}\left[\mathbf{D_l}\frac{\partial\overline{\mathbf{c}}_\mathbf{l}}{\partial\mathbf{x_j}} - \overline{\rho\mathbf{u}_\mathbf{j}'\mathbf{c}_\mathbf{l}'}\right] + \overline{\mathbf{S}_{\mathbf{c_l}}} \tag{11}$$

$$\frac{\partial \overline{\rho}\,\overline{\mathbf{u}}_i}{\partial t}+\frac{\partial}{\partial \mathbf{x}_j}\left(\overline{\rho}\,\overline{\mathbf{u}}_j\overline{\mathbf{u}}_i\right)=-\frac{\partial \overline{\mathbf{p}}}{\partial \mathbf{x}_i}+\frac{\partial}{\partial \mathbf{x}_j}\left[\mu\left(\frac{\partial \overline{\mathbf{u}}_i}{\partial \mathbf{x}_j}+\frac{\partial \overline{\mathbf{u}}_j}{\partial \mathbf{x}_i}\right)-\overline{\rho \mathbf{u}_j'\mathbf{u}_i'}-\frac{2}{3}\mu\frac{\partial \overline{\mathbf{u}}_m}{\partial \mathbf{x}_m}\delta_{ij}\right]+\rho \mathbf{g}_i \qquad (12)$$

$$\frac{\partial \overline{\rho}\,\overline{\mathbf{h}}}{\partial t}+\frac{\partial}{\partial \mathbf{x}_j}\left(\overline{\rho}\,\overline{\mathbf{u}}_j\overline{\mathbf{h}}\right)=\frac{\partial}{\partial \mathbf{x}_j}\left[\frac{\lambda}{\mathbf{C}_p}\frac{\partial \overline{\mathbf{h}}}{\partial \mathbf{x}_j}-\overline{\rho \mathbf{u}_j'\mathbf{h}'}\right]+\frac{\partial \overline{\mathbf{p}}}{\partial t} \qquad (13)$$

It is evident by comparing equations (1) to (4) with the above that the averaging procedure has produced equations where all instantaneous variables are replaced by their ensemble-averaged counterpart. Additionally new terms containing products of fluctuating quantities (so called "correlations") have appeared. In what follows the averaging signs (overbars) are retained only for the correlations and all dependent variables are considered as averaged values.

The averaging procedure produced a set of new unknowns in the momentum and energy conservation equations, respectively:

- Turbulent mass flux

$$\mathbf{q}_c^t=-\overline{\rho \mathbf{c}_l'\mathbf{u}_j'} \qquad (14)$$

- Turbulent momentum flux (Reynolds stress)

$$\mathbf{T}^t=-\overline{\rho \mathbf{u}_j'\mathbf{u}_i'} \qquad (15)$$

- Turbulent heat flux

$$\mathbf{q}_h^t=-\overline{\rho \mathbf{u}_j'\mathbf{h}'} \qquad (16)$$

Since these quantities are unknown, the averaged equations are accompanied by the so-called *turbulence models*, which provide these unknowns by expressing the correlations of the fluctuations in terms of the mean quantities. To do so, one has to rely on experimental data and knowledge obtained from DNS. No single model can be expected to reproduce well the effects of turbulence on the mean flow in all practical applications.

The most popular turbulence models are *eddy-viscosity models*, which postulate an analogy between the turbulent and viscous diffusion (Boussinesq eddy-viscosity hypothesis) and model the effects of turbulence by introducing turbulent diffusivity and viscosity coefficients:

$$\begin{aligned}
\mathbf{q}_c^t &\approx \rho \mathbf{D}_{l,t}\frac{\partial \overline{\mathbf{c}}_l}{\partial \mathbf{x}_j},\\
\mathbf{T}^t &\approx 2\mu_t\left(\frac{\partial \overline{\mathbf{u}}_i}{\partial \mathbf{x}_j}+\frac{\partial \overline{\mathbf{u}}_j}{\partial \mathbf{x}_i}\right)-\frac{2}{3}\left(\mu_t\frac{\partial \overline{\mathbf{u}}_m}{\partial \mathbf{x}_m}+\rho \mathbf{k}\right)\delta_{ij},\\
\mathbf{q}_h^t &\approx \lambda_t\frac{\partial \mathbf{T}}{\partial \mathbf{x}_j},
\end{aligned} \qquad (17)$$

where μ_t represents the turbulent viscosity and $\mathbf{k}$ stands for the turbulent kinetic energy (see below). These coefficients are non-linear functions of the flow parameters and usually vary several orders of magnitude within the flow region.

2.2.2 The $\kappa-\varepsilon$ model

The (standard) $\kappa-\varepsilon$ model is the most widely used eddy-viscosity model. It can be summarised as follows.

- $\mathbf{D}_l$, μ and κ are replaced by their so-called effective values:

$$\begin{aligned} \mathbf{D}_{l,\mathrm{eff}} &= \mathbf{D}_l + \mathbf{D}_{l,t}\ , \\ \mu_{\mathrm{eff}} &= \mu + \mu_t\ , \\ \lambda_{\mathrm{eff}} &= \lambda + \lambda_t \end{aligned} \tag{18}$$

  where $\rho\mathbf{D}_{l,t}$, μ_t and λ_t are the turbulent mass diffusivity, viscosity and conductivity, defined as:

$$\rho\mathbf{D}_{l,t} = \frac{\mu_t}{\sigma_{c_l}}, \quad \mu_t = \mathbf{C}_\mu \rho \frac{\mathbf{k}^2}{\varepsilon}, \quad \lambda_t = \frac{\mu_t \mathbf{C}_p}{\sigma_T}. \tag{19}$$

  Here; σ_{c_l}, $\mathbf{C}_\mu$ and σ_T are empirical coefficients (given in Table 1), and $\mathbf{k}$ stands for the kinetic energy of turbulence and ε for its dissipation rate.

The kinetic energy of turbulence κ and its dissipation rate ε are defined as:

$$\mathbf{k} = \frac{1}{2}\overline{\mathbf{u}_i'^2} \quad , \quad \varepsilon = \frac{\mu}{\rho}\overline{\left(\frac{\partial \mathbf{u}_j'}{\partial \mathbf{x}_i}\right)^2} \tag{20}$$

and are obtained by solving their respective transport equations:

$$\frac{\partial}{\partial \mathbf{t}}(\rho.\mathbf{k}) + \frac{\partial}{\partial \mathbf{x}_j}(\rho.\mathbf{u}_j.\mathbf{k}) = \frac{\partial}{\partial \mathbf{x}_j}\left(\frac{\mu_{\mathrm{eff}}}{\sigma_k}\frac{\partial \mathbf{k}}{\partial \mathbf{x}_j}\right) + \mu_{\mathrm{eff}}.\mathbf{G}_t - \frac{2}{3}\frac{\partial \mathbf{u}_m}{\partial \mathbf{x}_m}\left(\mu_{\mathrm{eff}}\frac{\partial \mathbf{u}_m}{\partial \mathbf{x}_m} + \rho.\mathbf{k}\right) - \rho.\varepsilon \tag{21}$$

$$\begin{aligned} &\frac{\partial}{\partial \mathbf{t}}(\rho.\varepsilon) + \frac{\partial}{\partial \mathbf{x}_j}(\rho.\mathbf{u}_j\varepsilon) = \frac{\partial}{\partial \mathbf{x}_j}\left(\frac{\mu_{\mathrm{eff}}}{\sigma_\varepsilon}\frac{\partial \varepsilon}{\partial \mathbf{x}_j}\right) + \frac{\varepsilon}{\mathbf{k}}\left\{\mathbf{C}_1\mu_{\mathrm{eff}}\mathbf{G}_t - \frac{2}{3}\mathbf{C}_1\frac{\partial \mathbf{u}_m}{\partial \mathbf{x}_m}\left(\mu_{\mathrm{eff}}\frac{\partial \mathbf{u}_m}{\partial \mathbf{x}_m} + \rho.\mathbf{k}\right)\right\} \\ &- \mathbf{C}_2\frac{\rho.\varepsilon^2}{\mathbf{k}} + \mathbf{C}_3\rho.\varepsilon\frac{\partial \mathbf{u}_m}{\partial \mathbf{x}_m} \end{aligned} \tag{22}$$

In the above equations

$$\mathbf{G_t} = \frac{\partial \mathbf{u_j}}{\partial \mathbf{x_i}}\left(\frac{\partial \mathbf{u_j}}{\partial \mathbf{x_i}} + \frac{\partial \mathbf{u_i}}{\partial \mathbf{x_j}}\right) \tag{23}$$

represents the generation rate of turbulent kinetic energy and $\sigma_{\mathbf{k}}, \sigma_{\varepsilon}, \mathbf{C}_1, \mathbf{C}_2$ and $\mathbf{C}_3$ are further empirical constants.

$\mathbf{C}_{\mu}$	$\mathbf{C}_1$	$\mathbf{C}_2$	$\mathbf{C}_3$	$\sigma_{\mathbf{k}}$	σ_{ε}	$\sigma_{\mathbf{T}}$	$\sigma_{\mathbf{k}}$	$\sigma_{\mathbf{c_1}}$
0.09	1.44	1.92	$-0{,}33$	1.0	1.3	0.9	0.9	0.9

Table 1: *The values of empirical coefficients in the standard* $\mathbf{k}-\varepsilon$ *model of turbulence*

3. Numerical Method

For all turbulent flow calculations the software package FLUENT [1] was used. FLUENT utilises a control-volume-based technique to convert the basic conservation equations (10) to (13) and (21) to (23) to algebraic equations that can be solved numerically. This control volume technique consists of integrating the governing equations about each cell of a computational mesh superimposed upon the flow field. The approach leads to discretised equations for each quantity of interest.

The first step in the analysis is to cast the aforementioned conservation equations into the general form

$$\frac{\partial}{\partial \mathbf{t}}(\rho\phi)+\frac{\partial}{\partial \mathbf{x_i}}(\rho \mathbf{u_i}\phi)=\frac{\partial}{\partial \mathbf{x_i}}\left(\Gamma_\phi \frac{\partial \phi}{\partial \mathbf{x_i}}\right)+\mathbf{S}_\phi \tag{24}$$

where ϕ stands for one of the physical variables, velocity $\mathbf{u_i}$, enthalpy $\mathbf{h}$, turbulent kinetic energy $\mathbf{k}$, or dissipation rate ε. Γ_ϕ is the effective (turbulent) diffusion coefficient. In the case, ϕ = 1, the above equation results in the continuity equation.

The external sinks and sources, i.e. all differential operators that do not fit into this generalised equation, are absorbed in the source term $\mathbf{S}_\phi$.

By integrating equation (24) over a small control volume of finite size, it follows that:

$$\frac{\partial}{\partial \mathbf{t}}\int_{\mathbf{V}} \rho\, \boldsymbol{\phi}\, \mathbf{dV}+\int_{\mathbf{A}} \rho \vec{\mathbf{u}}\, \boldsymbol{\phi}\, \overrightarrow{\mathbf{dA}}=\int_{\mathbf{A}} \Gamma_\phi \frac{\partial \boldsymbol{\phi}}{\partial \mathbf{x_i}} \overrightarrow{\mathbf{dA}}+\int_{\mathbf{V}} \mathbf{S}_{\boldsymbol{\phi}} \mathbf{dV}, \tag{25}$$

where $\vec{\mathbf{u}}$ is the velocity vector, $\vec{\mathbf{A}}$ is the surface area vector, and $\mathbf{V}$ the cell volume. This integration procedure is applied to each control volume or cell inside the computational domain. Discretising of the terms in the above equation and hence replacing each differential operator by its finite difference equivalent leads to:

$$\frac{\partial}{\partial \mathbf{t}}\int_{\mathbf{V}} \rho\, \boldsymbol{\phi}\, \mathbf{dV}=\frac{(\rho\boldsymbol{\phi}\mathbf{V})_{\mathbf{P}}-(\rho\boldsymbol{\phi}\mathbf{V})^{\circ}_{\mathbf{P}}}{\delta \mathbf{t}}, \tag{26}$$

$$\int_{\mathbf{A}} \rho \vec{\mathbf{u}}\, \boldsymbol{\phi}\, \overrightarrow{\mathbf{dA}}-\int_{\mathbf{A}} \Gamma_\phi \frac{\partial \boldsymbol{\phi}}{\partial \mathbf{x_i}} \overrightarrow{\mathbf{dA}}=\rho^*\left(\mathbf{u_j}^*\mathbf{s_j}\right)\phi^*+\Gamma_\phi{}^* \frac{\Delta\phi^*}{\Delta_\mathbf{j}} \tag{27}$$

and

$$\int_{\mathbf{V}} \mathbf{S}_{\boldsymbol{\phi}} \mathbf{dV}=(\mathbf{S}_1+\mathbf{S}_2\boldsymbol{\phi}_\mathbf{P})\mathbf{V}_{\mathbf{P}'}. \tag{28}$$

In the above equations the index $\mathbf{P}$ denotes the particular cell under consideration and the superscript "$\circ$" refers to the variable value at time $\mathbf{t} - \delta\mathbf{t}$.

All quantities marked with "*" are obtained by Interpolation between the node $\mathbf{P}$ and the corresponding neighbour node. $\mathbf{s_j}$ is the cell surface outward normal vector and $\frac{\Delta\phi^*}{\Delta_j}$ represents the central difference approximation of the derivative of ϕ in direction $\mathbf{j}$.

Assembling all the above expressions leads to the "linearized" form of the general conservation equation for a variable ϕ:

$$\mathbf{A_P}\phi_\mathbf{P} = \sum_{\mathbf{nb}} \mathbf{A_{nb}}\phi_{\mathbf{nb}} + \mathbf{A_P^\circ}\phi_\mathbf{P}^\circ + \mathbf{S}_\phi \qquad (29)$$

$\sum_{\mathbf{nb}}$ is the sum around all neighbour cells. The number of neighbours for each cell depends on the computational grid topology, but will be typically equal to the number of faces enclosing the cell (boundary cells being the exceptions).

The result of this procedure leads to a set of algebraic equations for each variable ϕ with a sparse coefficient matrix structure. Thus in a typical example for a flow domain containing 100.000 computational mesh cells for each variable ϕ (velocity component $\mathbf{u_i}$, enthalpy $\mathbf{h}$, turbulent kinetic energy $\mathbf{k}$ and dissipation rate ε) an equation system consisting of 100.000 unknowns or in total 600.000 equations have to be solved per iteration. Iterations are necessary since the coefficients $\mathbf{A_{nb}}$ in the above equation are functions of the a priori unknown velocity components $\mathbf{u_i}$.

Assuming that typically 20 iterations are necessary for convergence of the complete equation system for one time step, this means for the above example that 12.000.000 equations per time-step have to be solved. It is evident that for this powerful computing resources are necessary and even using them computation times of tens of hours are normal for solving a Computational Fluid Dynamics (CFD) problem.

Therefore one flow simulation within the tunnel of 150000 mesh cells required approximately 9 hours of CPU time on a DEC Alpha DS20.

4. General Considerations concerning Tunnel Fire Simulations

4.1 Turbulent Flame Spread

The detailed investigation of turbulent combustion processes including complex chemical reaction mechanisms on today's computing resources is prohibitive. Additionally there are a lot of uncertainties in every tunnel fire hazard study about the combustible materials involved. It is therefore common practise to replace the ignition and subsequent fire origin by a heat source in a predefined region. This region represents the burning car or heavy goods vehicle (HGV). As the geometrical shape of a single object has a negligible effect on the flow field inside the tunnel section modelled, the region where the fire originates from for simplicity is assumed to have a hexahedral shape.

Typical fire loads are in the order of a few [MW] for passenger cars and 20 to 30 [MW] for HGV. The worst scenario would be a tanker carrying liquid fuel representing a fire load of up to 200 [MW] [2].

As radiative heat transfer only effects the temperature level and not the smoke spreading behaviour, its influence on the exhaust gas extraction capabilities of the ventilation system is ignored. This simplification is also supported by recent studies which show, that radiation effects are only important in close vicinity to the fire [3].

4.2 Computational Model

Fresh Air Openings

At the fresh air openings a homogenous airflow corresponding to a certain volume flux is prescribed.

Exhaust Air Openings

An under-pressure is prescribed at the exhaust air openings to model the combustion gas extraction system.

Tunnel Portals

A certain pressure difference is set between both tunnel portals to account for the bariometric pressure difference and to induce a natural convection. It is not trivial to give typical values for the pressure difference because it is influenced by many factors and may change within hours. The main factors leading to a bariometric pressure difference are a difference in altitude of the tunnel portals and the weather conditions on both sides. The natural ventilation can be increased by wind blowing towards the tunnel portal.

Heat Source

A volume of 180 [m³] representing a HGV is placed in the tunnel. A constant heat release in terms of [W/m³] is described to account for the effects of a tunnel fire. Typical values are about 2 to 5 [MW] for a passenger car, 30 [MW] for trucks and up to 200 [MW] for tankers carrying combustible hydrocarbons [2].

Furthermore it should be mentioned [4] that a heat load of 30 [MW] generally is used to be representative for a design fire for tunnel ventilation system layout in most European countries.

Geometrical Model

For each test case, i.e. both the Mont Blanc and the Gleinalm tunnel, only a segment of 150 [m] length is considered in the simulation. This model consists of about 150 000 mesh cells for both cases. Except for the old ventilation system of the Gleinalm tunnel where the extraction openings are located every 6 [m] only one extraction opening is considered in each scenario.

4.3 Results Presentation

During combustion and subsequent flame propagation, temperatures well above 2000 [K] can be reached. However, since a temperature of 400 [K] is assumed to be mortal, all results subsequently presented are scaled to this critical value. Therefore temperatures above this level are shown in red. Furthermore in these scenarios where results are presented in form of three-dimensional isosurfaces additionally an isosurface of 350 [K] is displayed for easier interpretation of the results.

For visualisation purposes the results of each computational run are stored in time intervals of 0.04 [sec]. This means that 25 frames (pictures) are available to the Virtualfires visualisation partners for the display of events happening within one second in real time. Each time step contains approximately 27 [MB] and 86 [MB] of data for the Mont Blanc tunnel (case A) and the Gleinalm tunnel (case B) respectively. All results are stored on the fileserver of CD and accessible to the project partners via ftp.

5. Case A: Mont Blanc Tunnel

5.1 Introduction

The Mont Blanc Tunnel connects France and Italy beneath the Mont Blanc massif. The exact location can be seen from the map in Fig. 2.

Figure 2: *Mont Blanc region*

The tunnel is located at an altitude of about 1300 [m] with the Italian portal lying 107 [m] higher than the French one. The tunnel length is 11,600 [m] with a maximum slope of 2.4 [%] on the French side. The Mont Blanc tunnel is a two directional tube with an open cross section of about 46 [m²]. It was in operation for 34 years before a catastrophic fire occurred on March 24th, 1999 on the Italian side of the tunnel. A cross section of the tunnel is shown in Fig. 3. Details can be found in [2, 5].

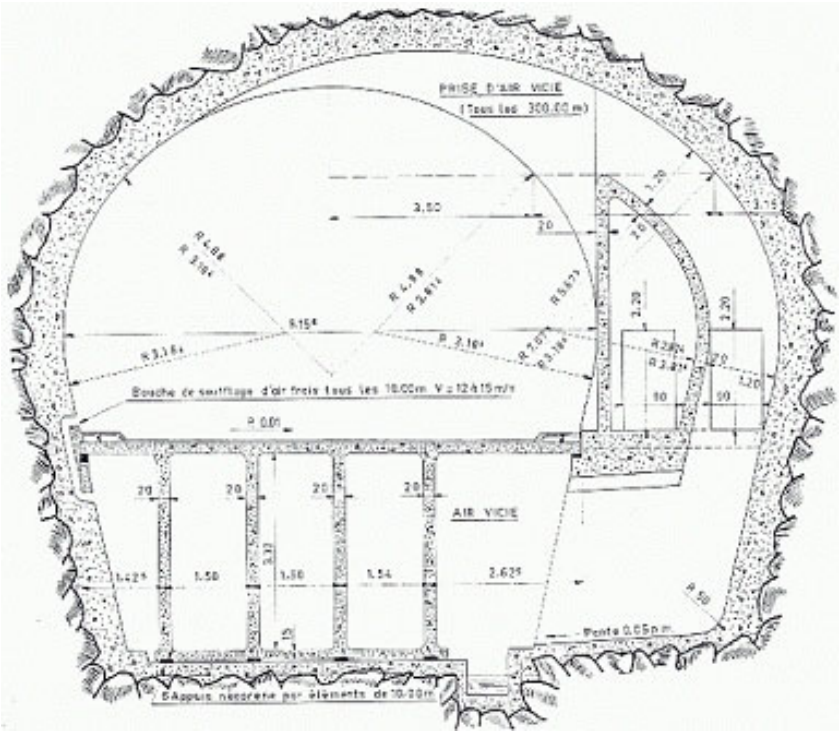

Figure 3: *Tunnel cross section*

5.2 Ventilation System

The ventilation system is of semi transverse type with ducts lying beneath the road surface. Four fresh air ducts start from each portal and each services a quarter of the tunnel half-length. A fifth duct was originally built for extraction, but can also be used for fresh air supply. After the fire in 1999 the size and locations of the exhaust air openings have been changed significantly. The control of the naturally induced longitudinal velocity is realised by means of jet fans .Details can be found in [5, 6, 7, 8].

Furthermore according to Brouses et al. [5] strong natural ventilation effects can occur due to a bariometric pressure difference on both sides of the tunnels. This pressure difference lies typically in the range of $\pm$ 300 [Pa] but can be up to $\pm$ 1000 [Pa]. As a consequence of this the longitudinal velocity can reach values of up to 15 [m/sec] at the tunnel portals. In emergency cases the velocity must be reduced to about 1.5 [m] as fast as possible to avoid destratification of the smoke.

Old Ventilation System (before 1999)

The ducts are capable of supplying 75 [m³/sec] of fresh air each. In extraction mode the fifth duct is capable of removing 150 [m³/sec] of exhaust air. Fresh air inlet openings of 0.32 [m] * 0.12 [m] size are located every 10 [m] at the lower part of the lateral wall in the Italy-French direction. An exhaust air extraction opening is located every 300 [m] at the upper part of the opposite side. The extraction openings are of 1.5 [m] * 1.0 [m] size. A representative tunnel section containing the old ventilation system can be seen in Fig. 4.

New Ventilation System

Again the fresh air inlet openings of 0.32 [m] * 0.12 [m] size are located every 10 [m] at the lower part of the sidewall. In contrast to the old system the exhaust air openings are now of 3.0 [m] * 3.0 [m] size and located every 100 [m] at the tunnel ceiling. This should result in a smoke extraction rate of 150 [m³/sec], which is well above the safety level suggested by Duffé et al [2]. Again a representative tunnel section is depicted in Fig. 5.

5.3 Scenarios Investigated for the Mont Blanc Tunnel

A summary of the parameters for the ventilation system is given in Table 2.

Scenario	**A1**	**A2**	**A3**	**A4**	**A5**
Fresh air volume flux [m³/sec] per inlet	0.58	0.58	0.58	0.58	0.58
Fresh air volume flux [m³/sec/km]	58	58	58	58	58
Extraction under pressure [Pa]	100	100	100	100	100
Bariometric pressure difference [Pa]	380	- 380	380	380	380
Heat source [MW]	5	5	5	30	100

Table 2: *Operating conditions for the Mont Blanc tunnel*

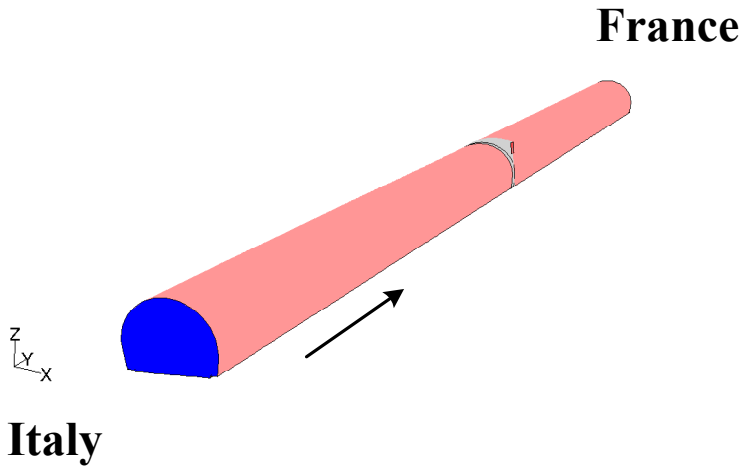

Figure 4: *Mont Blanc - old tunnel section*

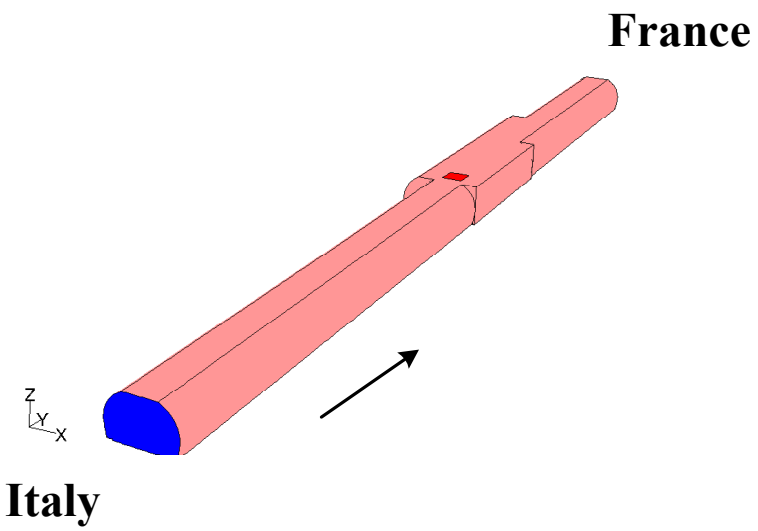

Figure 5: *Mont Blanc - new tunnel section*

Scenario A1: Old Ventilation System (Figs. A1.1 – A1.8)

The first scenario (A1) assumes a constant heat source of 5 [MW] and the bariometric pressure drop of 380 [Pa] is in line with the direction of the spiral flow induced by the ventilation system. This leads to a longitudinal ventilation of 2.5 [m/sec]. Fresh air at a constant rate of 5.8 [m³/sec] per 100 [m] tunnel length enters through the inlet openings. The under-pressure at the extraction openings is 100 [Pa].

As can be seen in Fig. A1.1 at the beginning of the fire the hot gases spread in both direction, but preferred into the direction of the spiralling natural convection flow. For the first 200 [sec] a strong stratification of the hot gases along the ceiling is observed. Subsequently the peak temperatures and the hot gases stratification are decreasing, but close to the fire origin temperatures are still well above 400 [K].

As can be seen in Fig. A1.7, the ventilation system is not able to remove all combustion gases, as they proceed further downstream into the tunnel. The gas velocities inside the tunnel are found to be below 5 [m/sec] and only close to the extraction system outlet values of approximately 20 [m/sec] are reached.

Scenario A2: Old Ventilation System with Reversed Pressure Difference (Figs. A2.1 – A2.8)

Most time of the year the natural convection and hence ventilation direction is from France towards Italy. About twenty times a year the opposite situation can occur, as it was the case for the catastrophic fire in 1999. For scenario A2 the bariometric situation therefore has been reversed and a pressure difference of 380 [Pa] was assumed to exist between the Italian and French side of the tunnel. The heat source was placed at a certain distance from the extraction opening on the “Italian side”. All other parameters are the same as applied in scenario A1.

As in the previous scenario A1 it can be observed in Fig. A2.1 that initially the hot gases tend to spread in both directions.

However, the back layering is now pronounced due to the reversed natural ventilation direction. Again stratification effects can be observed. Apparently the ventilation system is able to extract a certain amount of the hot gases against the main flow direction.

Due to the shorter distance between the heat source and the extraction opening compared to scenario A1, the zone where the temperature exceeds 400 [K] is much smaller in the early stage of the fire. AS can be seen in Fig. A2.7, after 300 [sec] the hot gases are flowing mainly towards the Italian side and the extraction opening next to the fire is able to remove only a very small amount of them. There is no pronounced stratification found anymore.

Scenario A3: New Ventilation System assuming a Passenger Car Fire (Figs. A3.1 – A3.8)

The first of the following three scenarios considers the new ventilation system of the Mont Blanc tunnel in operation since 2002. All ventilation system parameters are the same, but the fire load varies.

Scenario A3 assumes a fire load of about 5 [MW], which is the upper limit for a passenger car fire. It can be clearly see from Figs. A3.1 – A 3.8 that the new ventilation system of the Mont Blanc tunnel is able to control the spread of hot gases effectively in the case of a small fire. The combustion products are removed from the extraction system almost completely. No significant back layering effects can be observed. Except for the zone between the fire location and the extraction opening the tunnel is free of hot gases and the temperature rise is insignificant.

Scenario A4: New Ventilation System assuming a Heavy Goods Vehicle (HGV) Fire (Figs. A4.1 – A4.8)

Scenario A4 considers a fire involving a HGV carrying no goods or materials with low heat release. This type of HGV is represented by a heat load of 30 [MW], which is – as mentioned above – also the typical design fire for tunnel ventilation system layout. All other parameters are the same as in scenario A3.

As can be seen in Fig. A4.1, the fire starts to spread rapidly in both directions. Initially the extraction system is able to remove a fraction of the hot gases therefore the bottom of the tunnel on the downstream side of the extraction system remains at a low temperature level for some time. Nevertheless a layer of hot gases below the ceiling starts to develop. Due to natural ventilation the combustion products are pushed towards France and the ventilation system is not able to remove all the hot gases further on (Figs. A4.3 and A4.4). The strong stratification of hot gases starts to disappear and the tunnel temperature at the downstream side of the extraction opening rises substantially. Finally the upstream side of the HGV is free of combustion products, but at the downstream side the temperatures are still well above 400 [K].

Scenario A5: New Ventilation System assuming a Tanker Disaster (Figs. A5.1 – A5.8)

One further scenario was considered to investigate the effect of a fire involving a HGV carrying highly combustible materials.

Again the new ventilation system of the Mont Blanc tunnel was modelled. Except of the fire load all parameters were the same as in scenario A3 & A4.

The fire load was assumed to be in the order of 100 [MW], which is a realistic value for tanker carrying fuel. According to Duffé et al [2] heat loads of that order are not reached immediately after the on-set of the fire, but after approximately 10 [min]. Nevertheless in the simulation the fire load of 100 [MW] was applied right from the beginning.

Figs. A5.1 – A5.8 show clearly the disastrous effects of a tank trailer fire. The fire starts to spread immediately in both directions. After 50 [sec] almost the whole tunnel section is filled with gases much hotter than 400 [K]. The extraction system is able to delay the flame spread towards France, but has only little effect on the propagation of hot gases towards Italy. Later on on the French side the tunnel is gradually filled with hot gases. As depicted in Fig. A4.5, after 200 [sec] there is only a small zone existing at the bottom of the tunnel where the temperature does not exceed 400 [K].

Any natural ventilation effects are suppressed by the extension of hot gases induced by the fire. Although the extraction system is able to remove a portion of the hot gases, its efficiency is limited for fire disasters of this order.

6. Case B: Gleinalm Tunnel

6.1 Introduction

The Gleinalm Tunnel is located in Styria and is part of the Phyrn motorway connecting Graz with the upper part of Styria. The southern portal is located about 35 [km] in the north of Graz, the northern one in the vicinity of St. Michael in der Obersteiermark. The location is depicted in Fig. 6.

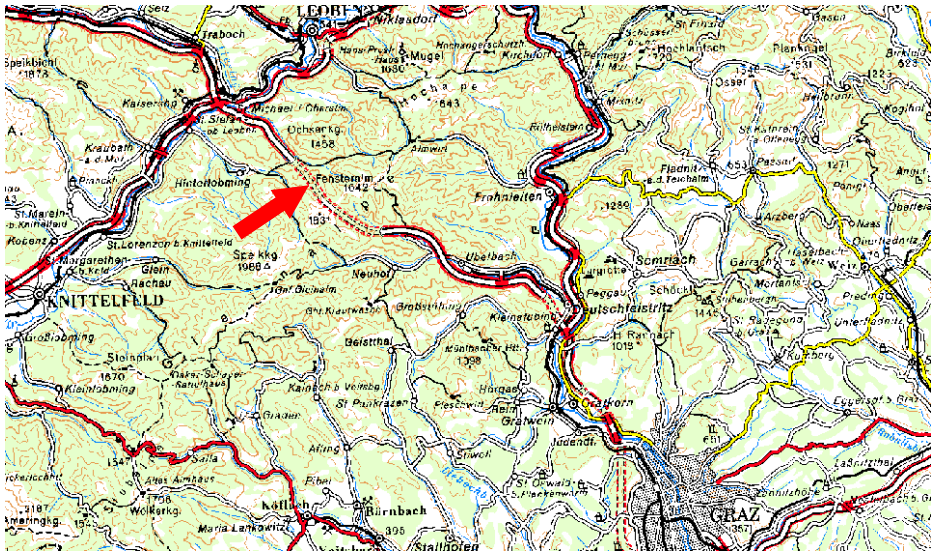

Figure 6: *Gleinalm region (© Österreichisches Bundesamt für Eich- und Vermessungswesen/Vienna, Austria)*

The Gleinalm Tunnel is one of the longest tunnels in Austria with a length of 8,320 [m]. The altitude of both tunnel portals is about 800 [m]. On the 6th of August 2001 a tunnel fire involving two passenger cars and about 10 persons occurred. The two vehicles caught fire and burned out completely. Five persons on board of a minivan burned to death in their car. After the catastrophic fires in the Mont Blanc and Tauern tunnel and the tunnel hazard in the Gleinalm itself the ventilation system has been redesigned in 2002 [9]. The regular cross section of the Gleinalm tunnel can be seen in Fig. 7.

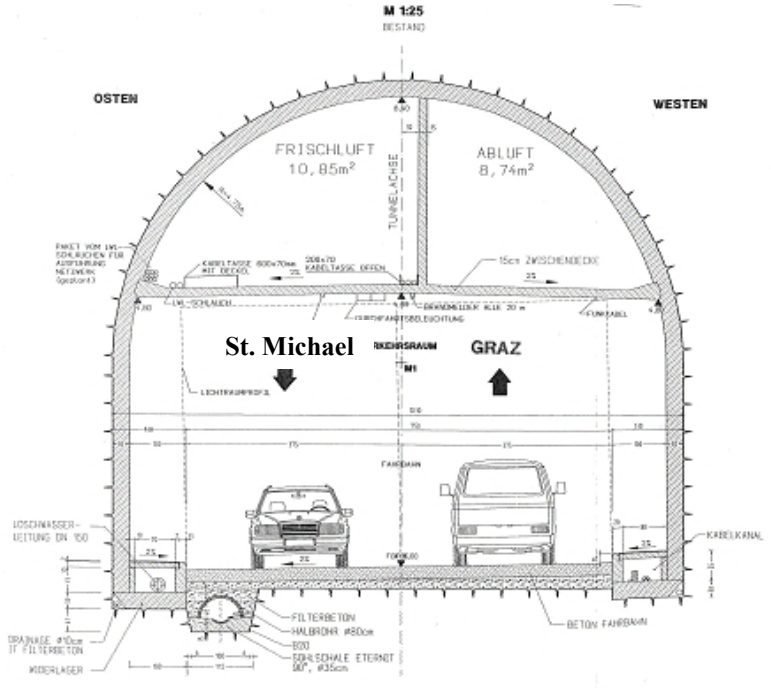

Figure 7: *Regular cross-section of Gleinalm Tunnel (© ÖSAG)*

6.2 Ventilation System

As in most Austrian single lane tunnels a full cross ventilation system is in operation. The ducts are located above the tunnel ceiling. The most significant difference between old and new ventilation system can be found in the design of the exhaust air openings [10].

Although both tunnel portals are located at an altitude of about 800 [m] there can be a substantial bariometric pressure difference. The Gleinalm massif is a strong weather divide between the southern and northern part of Styria. Long time experience indicates that the typical weather situation is high bariometric pressure at the southern portal and low bariometric pressure in the north. It has to be noted that the weather conditions can change very rapidly even in the course of the day.

Old Ventilation System (before 2002)

The fresh air openings of 0.605 [m] * 0.25 [m] size are located every 6 [m] above the lane directed to St. Michael (north) of the tunnel ceiling. The maximum fresh air rate is about 135 [m³/sec/km]. The exhaust air openings of the same size are located at the opposite side of the ceiling every 6 [m], i.e. above the road track directed to Graz (south).

New Ventilation System

The fresh air openings correspond to the ones of the old system. However, instead of the small exhaust openings now a very large opening with a size of 3.0 [m] * 3.0 [m] is located every 100 [m] at the tunnel ceiling.

6.3 Scenarios Investigated for the Gleinalm Tunnel

The parameters of the ventilation system are given in Table 3. The computational domains including the old and the new ventilation system are depicted in Figs. 8 and 9. The arrow indicates the direction of the natural ventilation flow induced by the bariometric pressure difference.

Scenario	**B1**	**B2**	**B3**
Fresh air volume flux per opening [m³/sec]	0.75	0.75	0
Fresh air volume flux [m³/sec/km]	120	120	0
Extraction under pressure [Pa]	150	150	150
Bariometric pressure difference [Pa]	800	800	800
Heat source [MW]	30	30	30

Table 3: *Operating conditions for the Gleinalm tunnel*

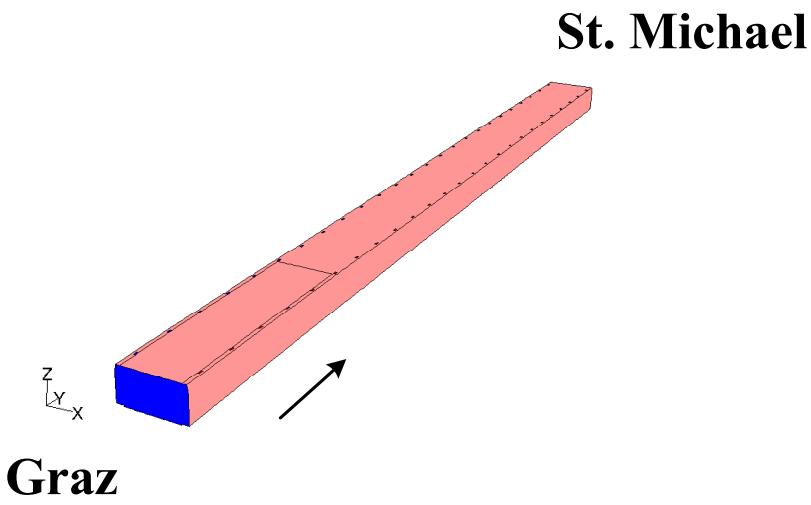

Figure 8: *Gleinalm tunnel - old tunnel section*

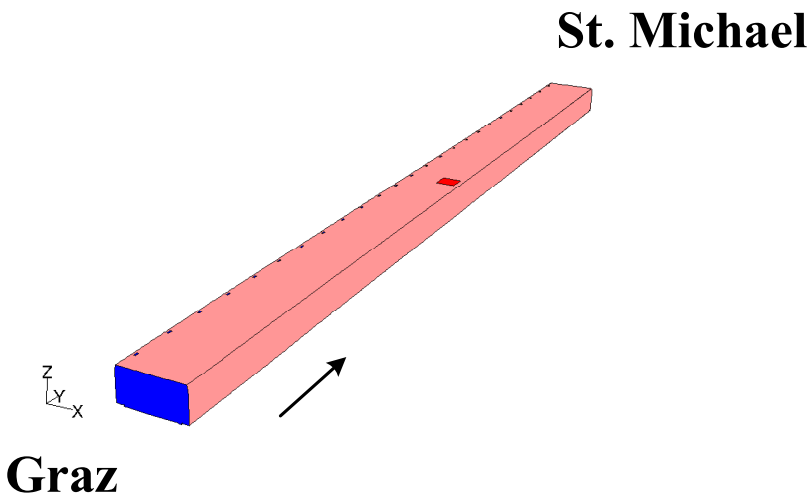

Figure 9: *Gleinalm tunnel - new tunnel section*

Scenario B1: Old Ventilation System (Figs. B1.1 – B1.8)

Scenario B1 takes into account the old ventilation system of the Gleinalm tunnel as it was before 2002. The ventilation system is in full operation i.e. the fresh air is supplied through the fresh air inlets and hot gases are removed through the extraction system. A very large, but not unusual bariometric pressure difference of 800 [Pa] is assumed inducing a natural ventilation flow directed to St. Michael in the north.

As it can be seen from B1.1 and B1.2, the hot gases start to spread in both directions, but are pushed strongly into the flow direction induced by the ventilation system. After a very short time the downstream side of the tunnel is completely filled with hot gases and the temperature exceeds 400 [K] in almost the whole area.

It can be concluded that in this case the ventilation system as it was used before 2002 appears to be insufficient for this situation.

Scenario B2: New Ventilation System with Working Fresh Air Supply
(Figs. B2.1 – B2.8)

The second scenario covers the recently installed ventilation system where it is assumed, that only one large extraction opening close to the fire source is in full operation for removal of hot combustion gases. All other exhaust openings in such a case are closed by the tunnel operator to prevent spread of toxic gases down to the floor level far away from the fire. This situation will occur after the hot combustion gases, which initially would flow along the ceiling, are cooling down. Through the inlets fresh air is supplied at a very high rate.

As depicted in Figs. B2.1 – B2.4, only for a short time after the initiation of the fire the hot gases spread in both directions along the ceiling but to a smaller extent than in the case of the old ventilation system. It can be clearly seen that the extraction system is capable to remove a large amount of hot gases. The temperatures downstream of the extraction opening are considerably lower than those using the old system. The high temperature area is concentrated between the HGV and the extraction opening.

Nevertheless, through the strong mixing process induced by the fresh air supply the exhaust gases cannot be removed completely and start spreading downstream.

Scenario B3: New Ventilation System without Fresh Air Supply
(Figs. B3.1 – B3.8)

Contrary to scenario B2 it is assumed that no fresh air enters the tunnel through the inlet openings.

Now a much stronger stratification of hot gases can be observed. A relatively large area between the HGV and the extraction opening exists were the temperature does not exceed 400 [K] at the bottom of the tunnel for a long time.

Although the extraction system is again not able to remove the whole amount of hot gases a relatively cool area remains at the bottom of the tunnel. As such ventilation scenario B3 is preferable against B2.

7. Summary and Conclusion

Two different tunnels with different fire hazard scenarios have been investigated in the present study.

The first case was the Mont Blanc tunnel. The old ventilation system as it was before the fire disaster in 1999 was considered as well as the new ventilation system now in operation since the tunnel has been reopened. The effect of different hazard scenarios and hence heat loads on the efficiency of the extraction system configurations has been computed.

It was found that both, the old and the new ventilation system, work well for passenger car fires. The new system is also able to keep the tunnel partly free of smoke for a HGV hazard. Nevertheless computations of a fuel tanker disaster showed, that the ventilation system still has little impact on the propagation of combustion gases and smoke in this case .

Considering the Gleinalm tunnel as a second case, in total three different scenarios have been investigated. All scenarios assumed a HGV burning inside a tunnel section.

In the first scenario the ventilation system as it was before 2002 and its effect on smoke propagation was considered. The second scenario comprised of the new ventilation system with working fresh air supply, whereas in the third case the fresh air supply was turned off. From this it can be concluded, that the new ventilation system is superior to the old one with respect to hot exhaust gas removal. Furthermore it was shown that deactivation of the fresh air supply during a hazard pronounces stratification of hot gases to exist for a longer time. A region of favourable low temperatures can be observed in this case close to the hazard origin.

As such the project phase concerned with the a-priori computations of tunnel fire hazards and the generation of CFD data (Workpackage 5.1) using the commercial flow solver FLUENT is now finished. The next project phase, which for the first time also will involve real time CFD simulations of tunnel fire hazards (WP 5.2) will rely on the ICE flow and combustion solver, where the development work on software version 1.0 at the Christian-Doppler-Laboratory for Applied Computational Thermofluiddynamics currently is in its final stages. The release of this version according to the workplan is due by project month 14.

8. Literature

[1] Fluent Inc.
"User's Guide for Fluent 6"
Lebanon, USA, 2001

[2] Duffé et al.
Report of the "Task Force for technical investigation of the 24th March 1999 fire in the Mont Blanc vehicular tunnel"
Ministry of Equipment, Transportation and Housing, France, 1999

[3] Mann M. and Segalla C.
"CFD Simulation of Smoke Propagation and Ventilation Efficiency of Tunnel Fire Incidents"
Proceedings of the International Conference on Tunnel Safety and Ventilation, Graz/Austria
April 8th – 10th 2002, p. 167 – 174

[4] Zumsteg F. and Steinemann U.
"Ventilation of Road Tunnels – The new Swiss Directive"
Proceedings of the International Conference on Tunnel Safety and Ventilation/Graz, Austria
April 8th – 10th 2002, p. 239 - 246

[5] Brouses B., Voeltzel A., Le Botlan Y. and Ruffin E.
"Ventilation and Fire Tests in the Mont-Blanc Tunnel to Better understanding the Catastrophic Fire of March 1999"
INERIS, France, 2000

[6] Bettelini M., Brandt R. and Riess I.
"Progress in Tunnel Ventilation - The Mont-Blanc Tunnel"
AITES-ITA 2001 World Tunnel Congress, Milano, Italy/June 10th – 13th, 2001

[7] Bettelini M.
"Le nouveau tunnel du Mont Blanc – Ventilation et Sécurité"
Chantiers 2002(2), p. 10 – 14

[8] Guigas X., Weatherill A. and Trottet Y.
"The new Ventilation Systems of the Mont-Blanc Tunnel"
http://www.atmb.net, Switzerland, 2002

[9] Hörhan R.
"Tunnel Accidents and their Impact on Relevant Guidelines in Austria"
Proceedings of the International Conference on Tunnel Safety and Ventilation/Graz, Austria
April 8th – 10th 2002, p. 1 – 8

[10] Österreichische Autobahnen- und Schnellstraßen AG
"Gleinalmtunnel Weströhre"
Construction drawings, 2001, unpublished

9. Appendix

MONT BLANC TUNNEL FIRE SIMULATIONS

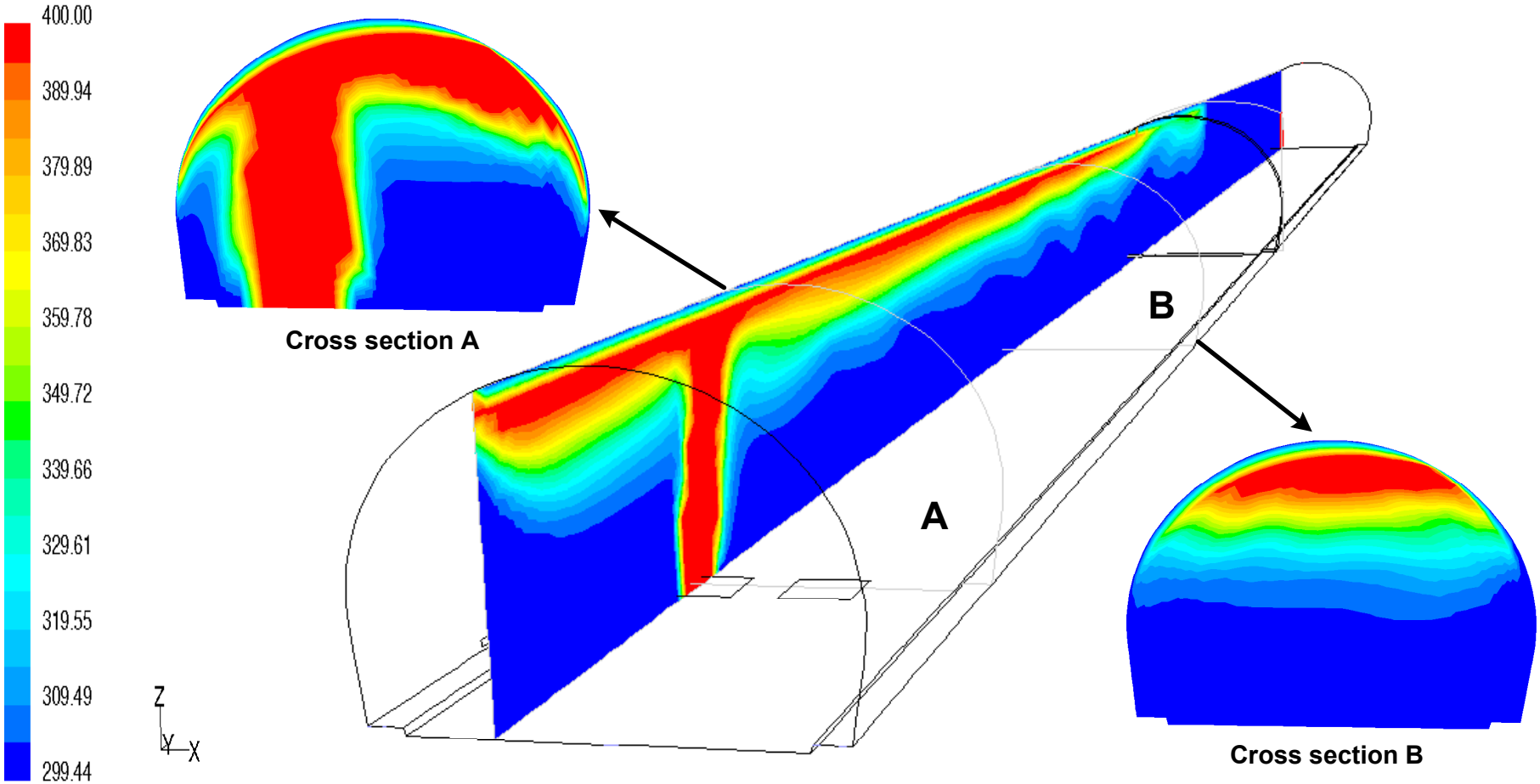

Figure A1.1: *Temperature distribution in different cut planes for scenario A1 (time=50s)*

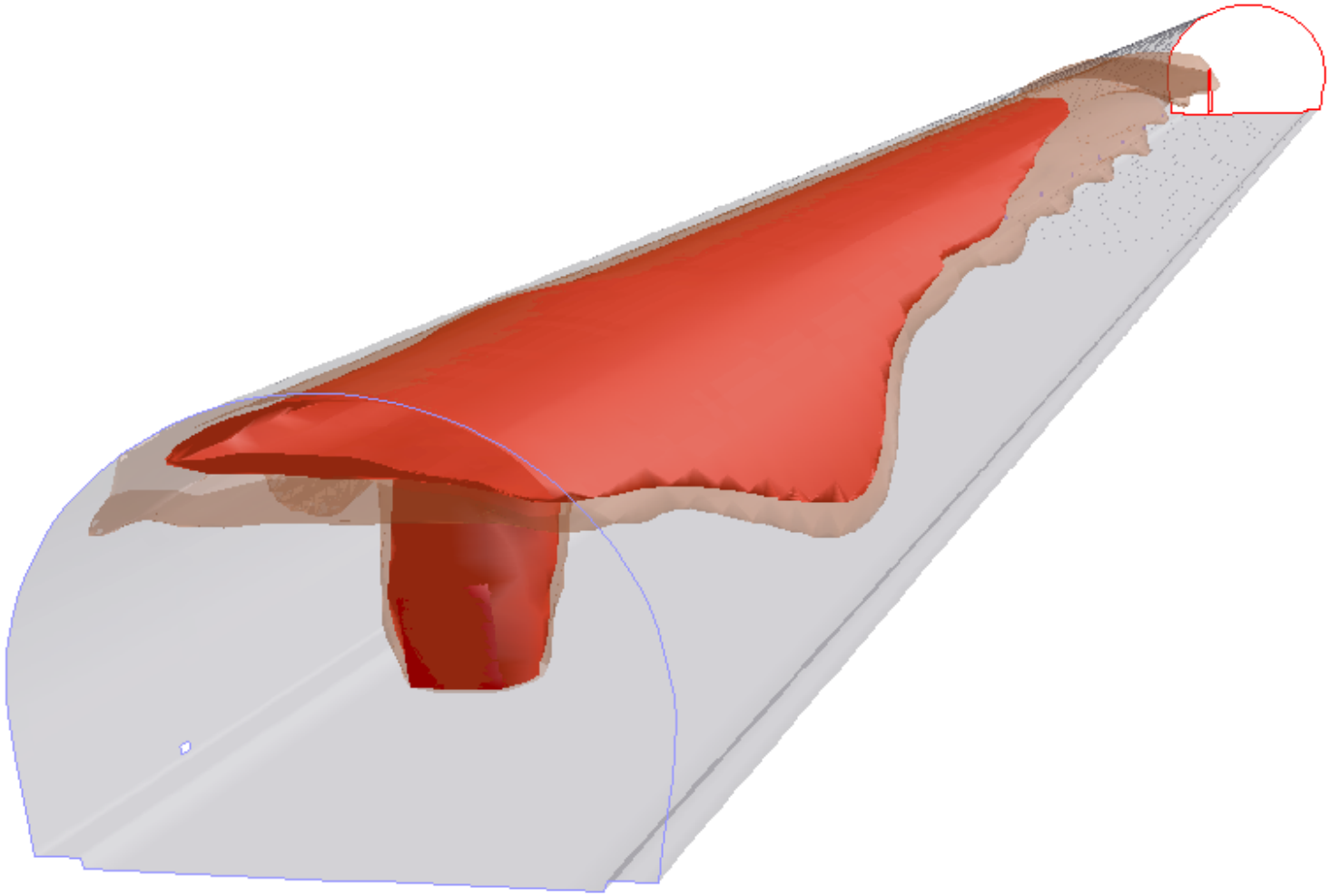

Figure A1.2: *Temperature isosurfaces for 350 [K] and 400 [K] (time=50s)*

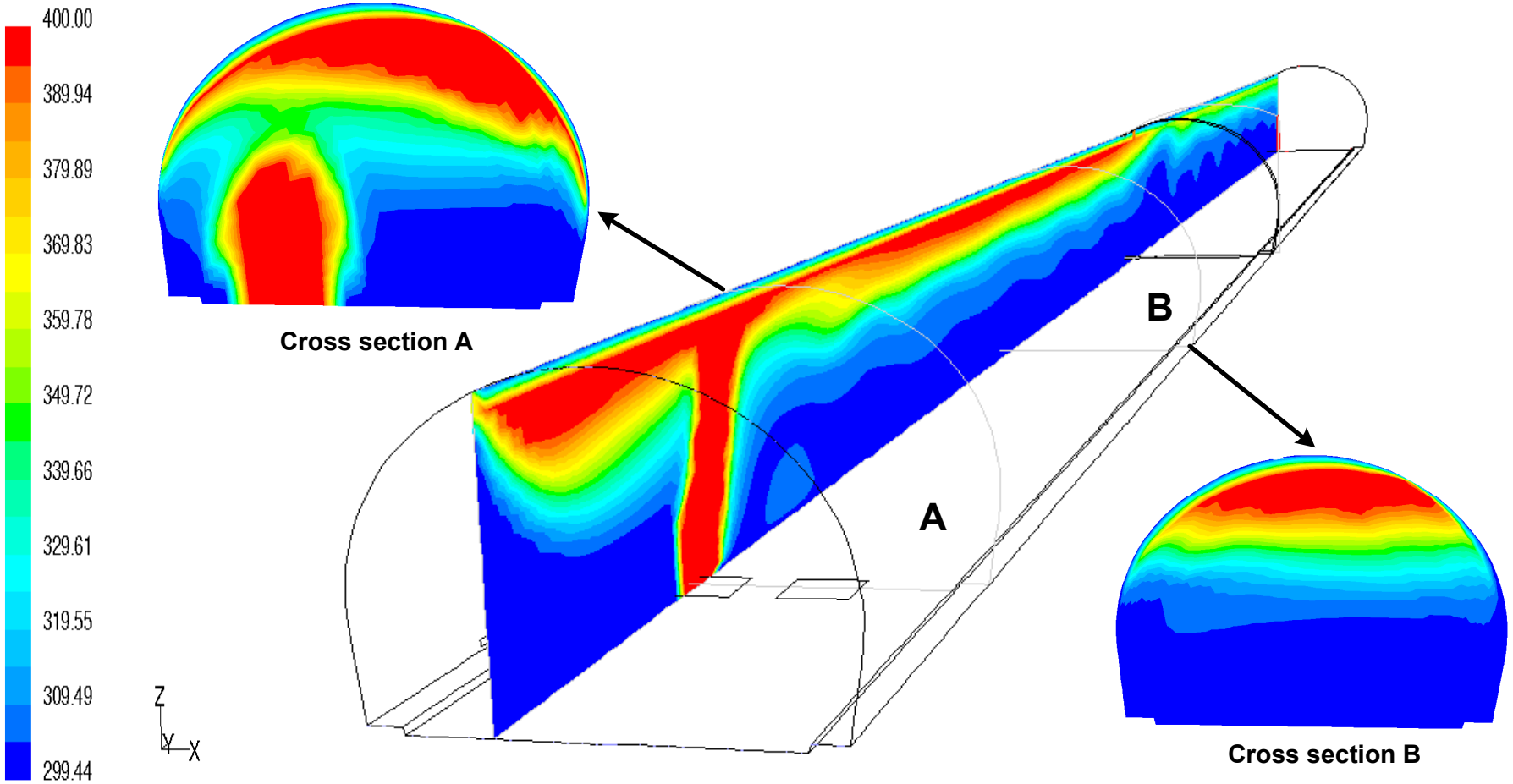

Figure A1.3: *Temperature distribution in different cut planes for scenario A1 (time=100s)*

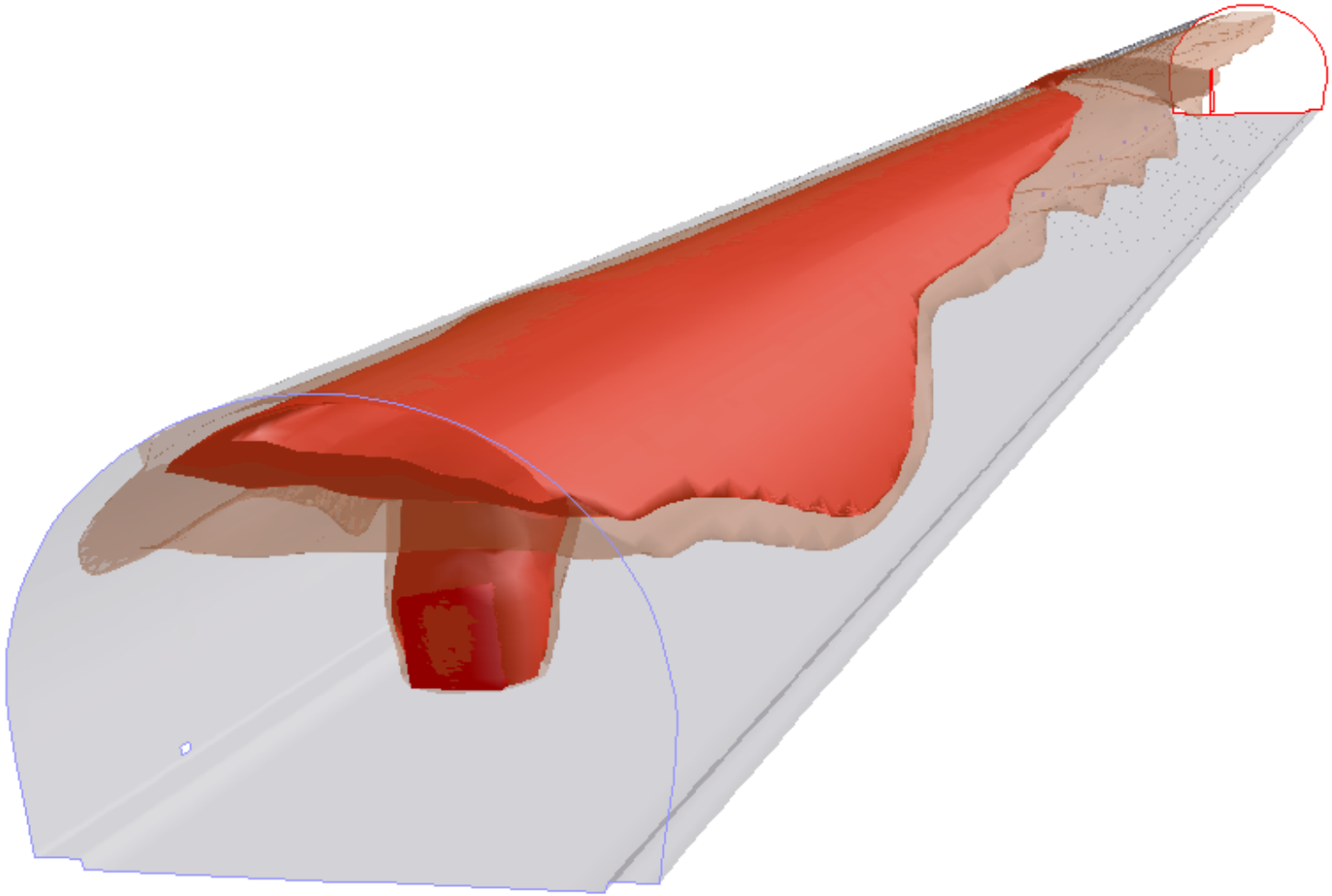

Figure A1.4: *Temperature isosurfaces for 350 [K] and 400 [K] (time=100s)*

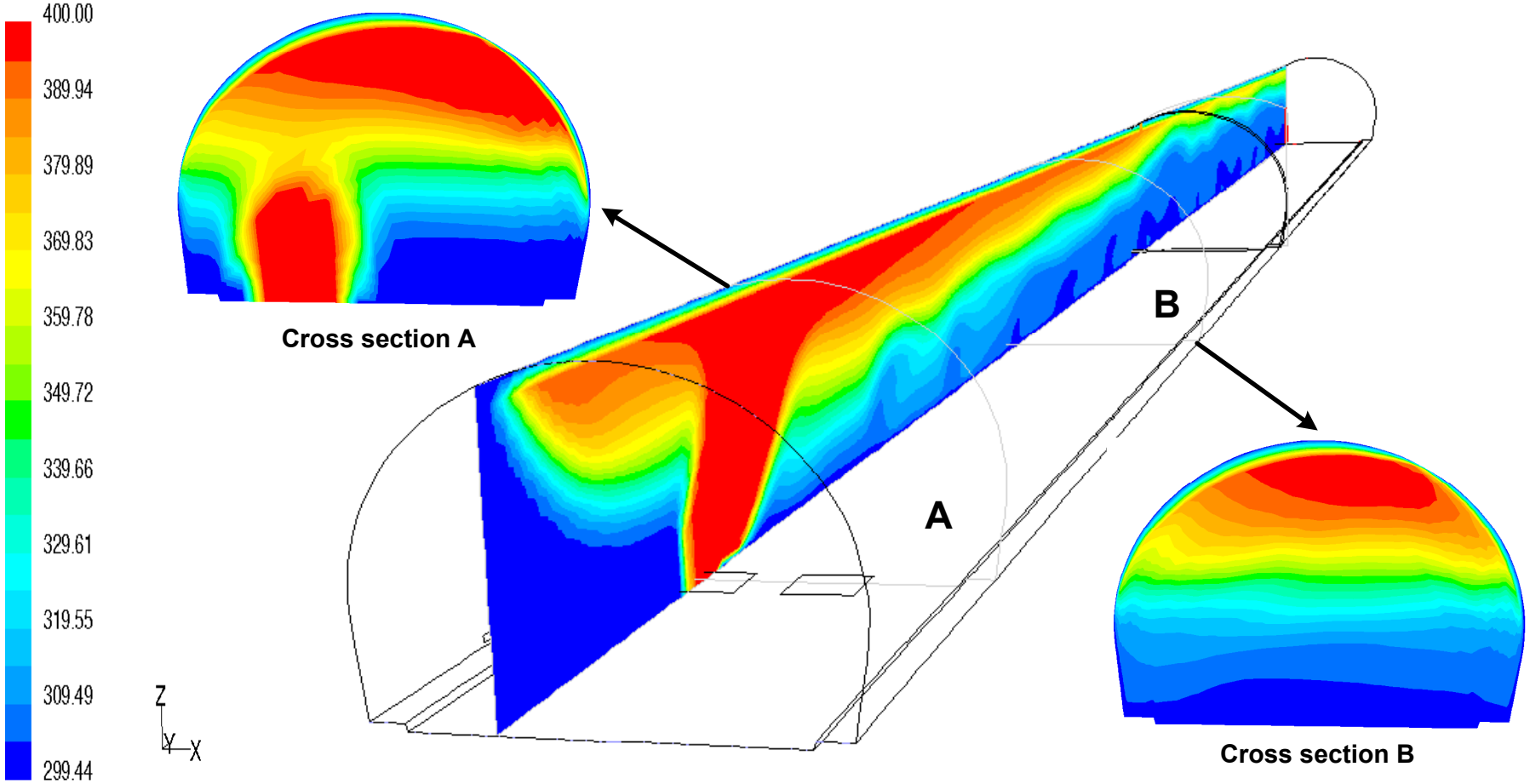

Figure A1.5: *Temperature distribution in different cut planes for scenario A1 (time=200s)*

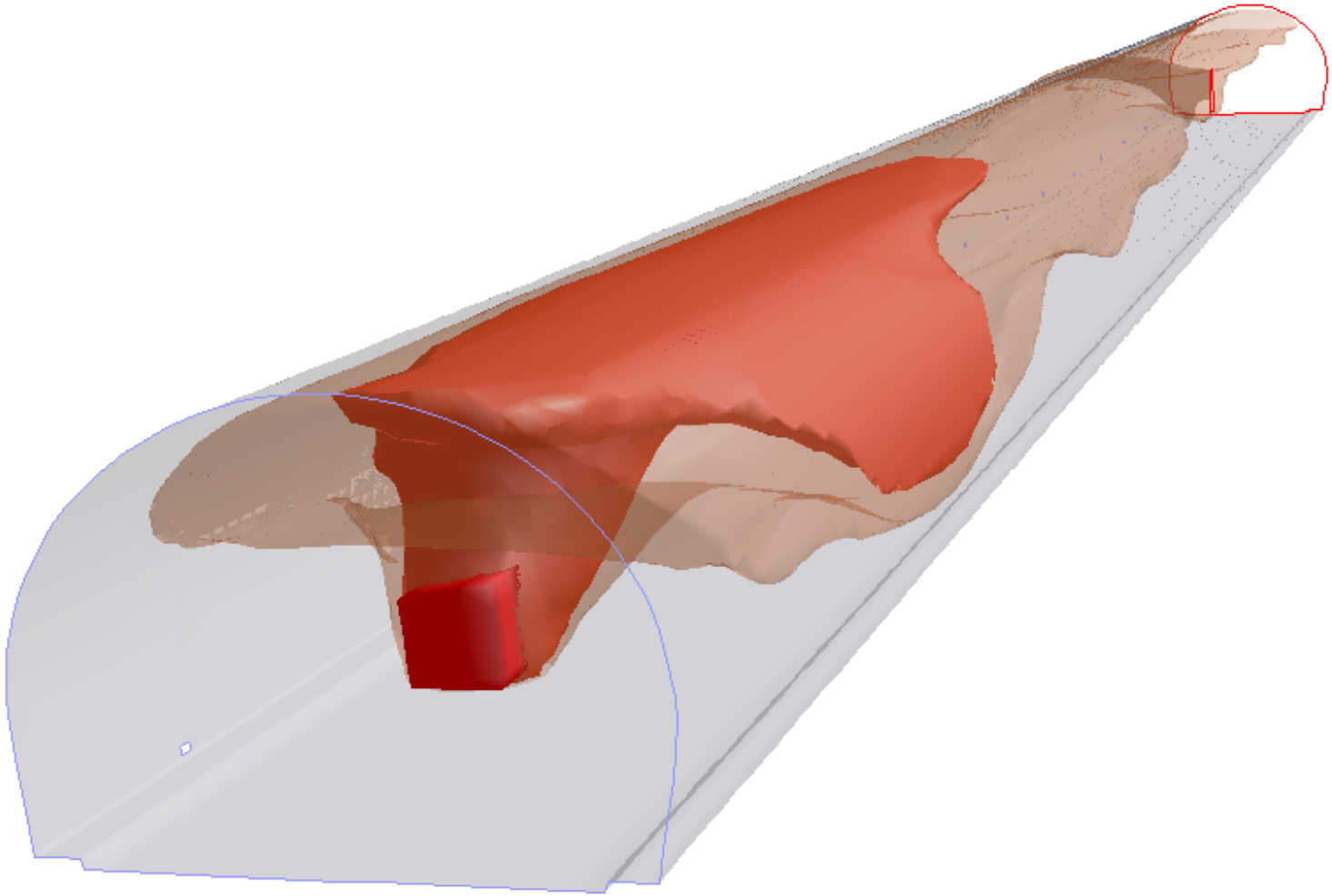

Figure A1.6: *Temperature isosurfaces for 350 [K] and 400 [K] (time=200s)*

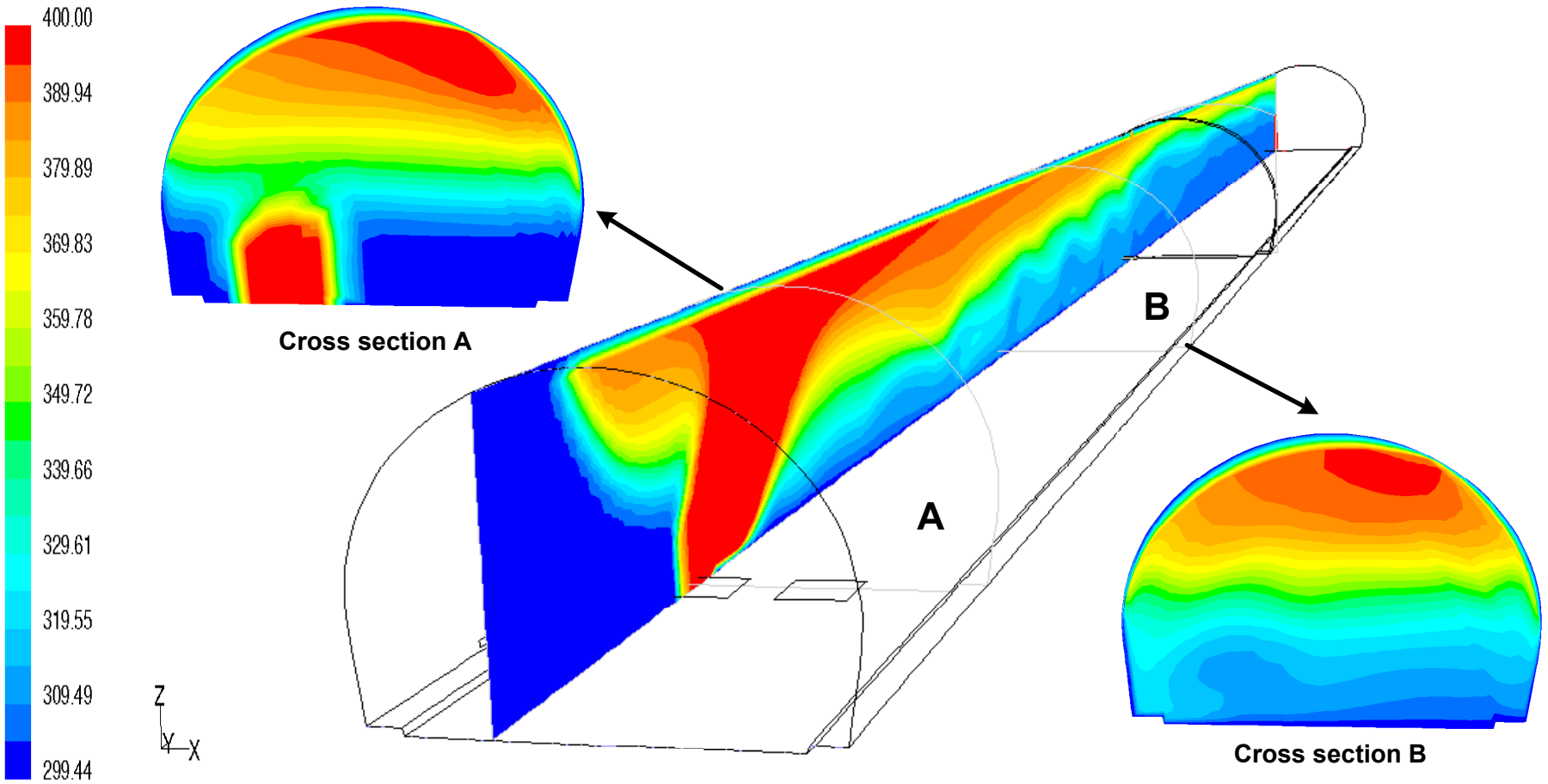

Figure A1.7: *Temperature distribution in different cut planes for scenario A1 (time=300s)*

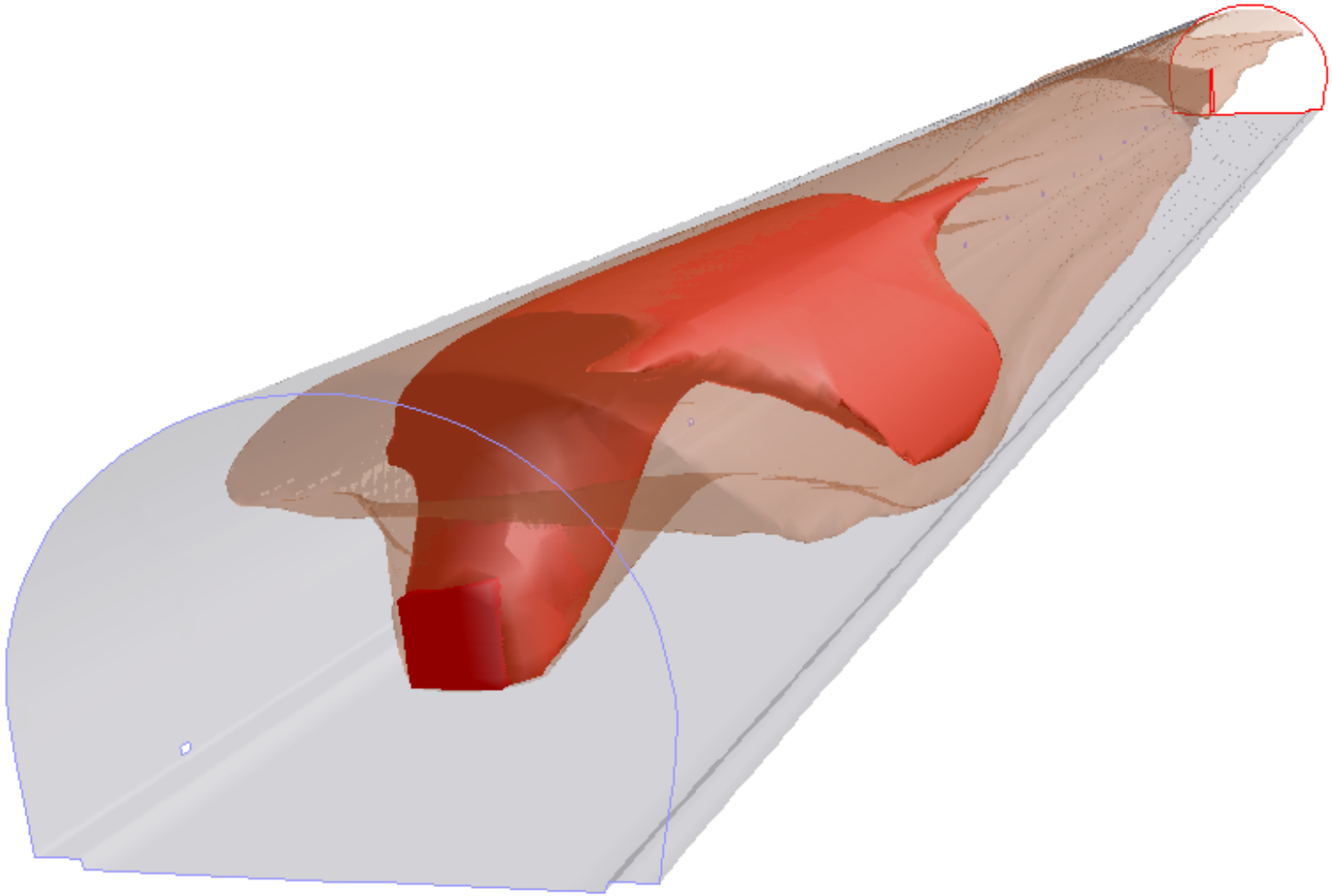

Figure A1.8: *Temperature isosurfaces for 350 [K] and 400 [K] (time=300s)*

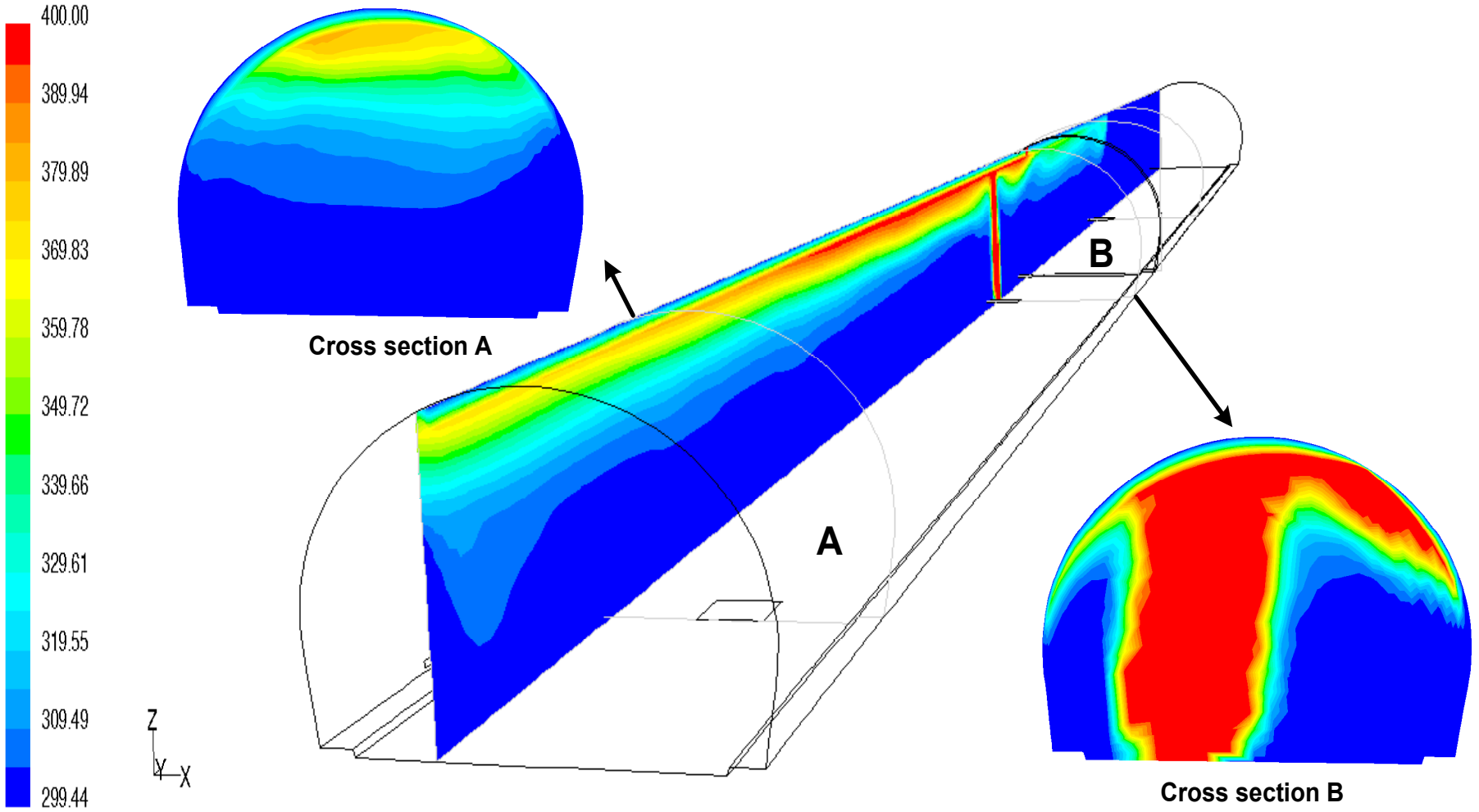

Figure A2.1: *Temperature distribution in different cut planes for scenario A2 (time=50s)*

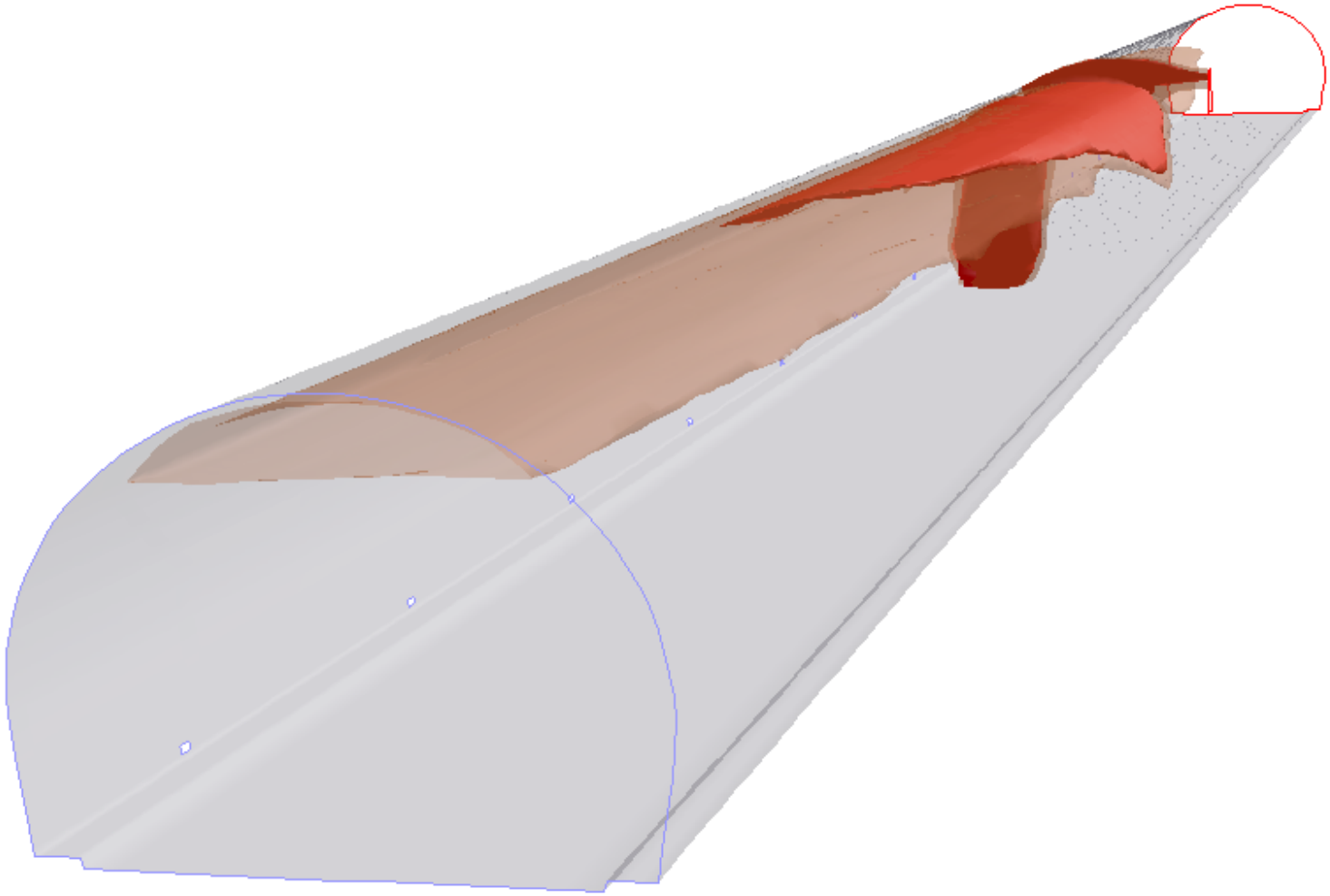

Figure A2.2: *Temperature isosurfaces for 350 [K] and 400 [K] (time=50s)*

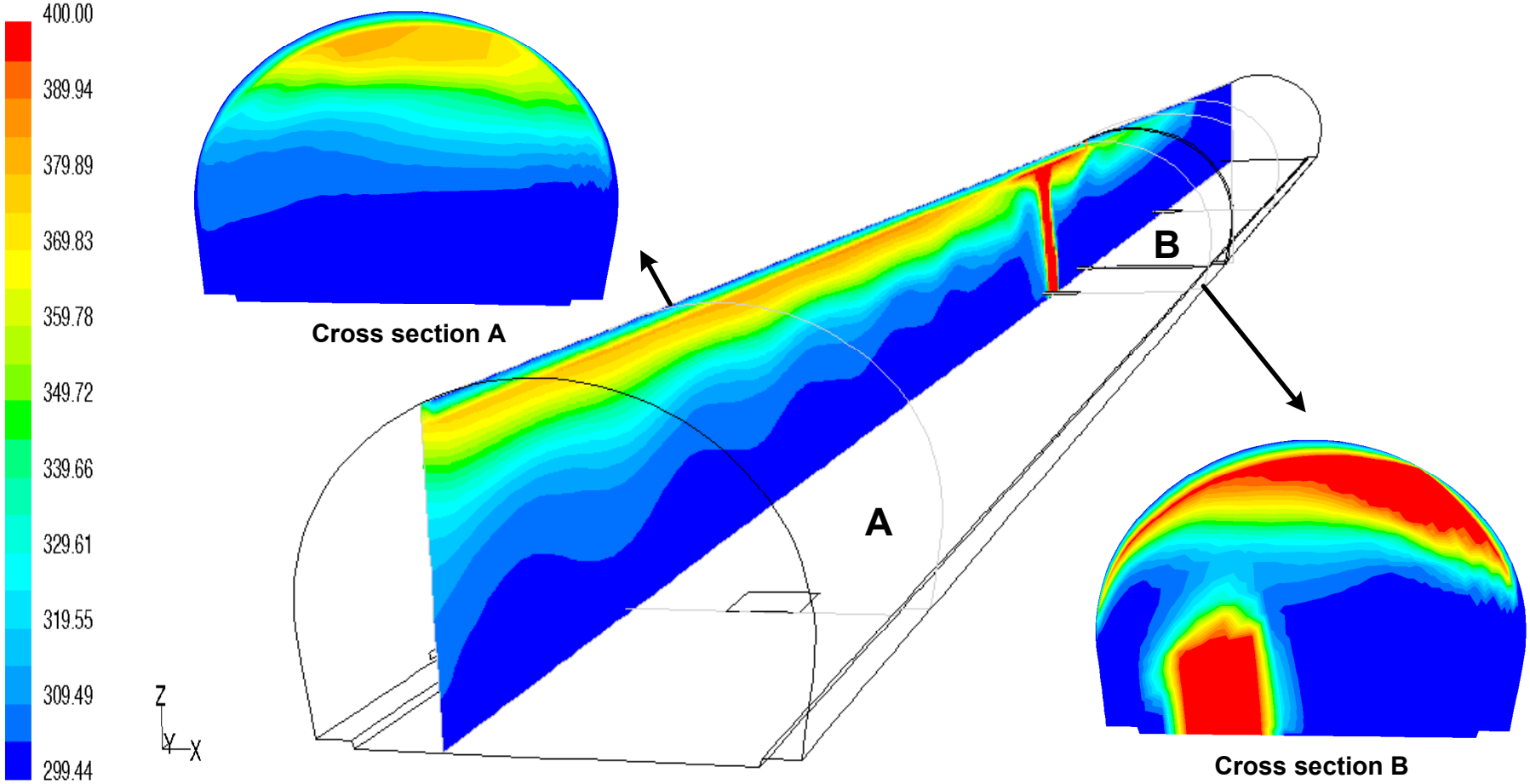

Figure A2.3: *Temperature distribution in different cut planes for scenario A2 (time=100s)*

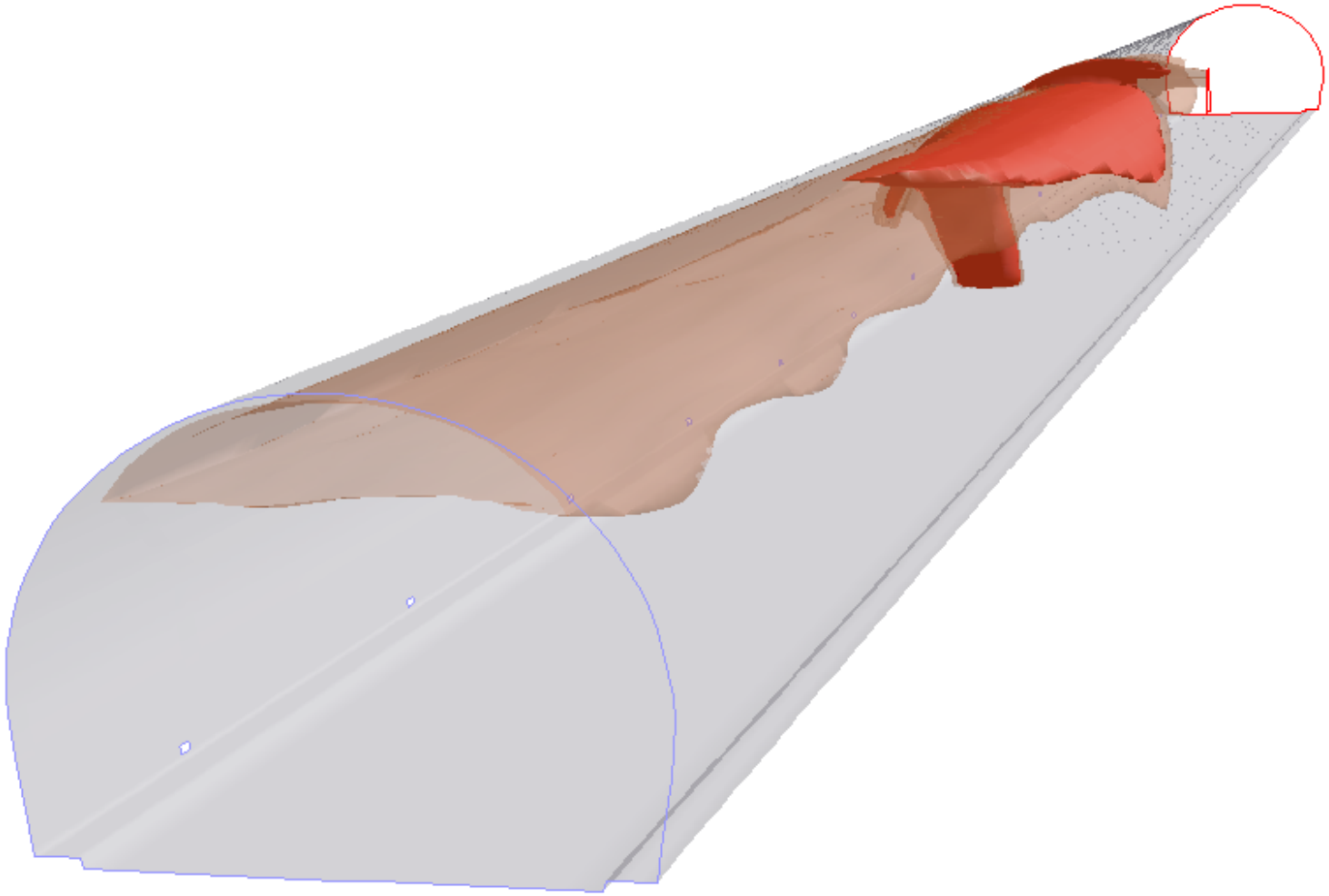

Figure A2.4: *Temperature isosurfaces for 350 [K] and 400 [K] (time=100s)*

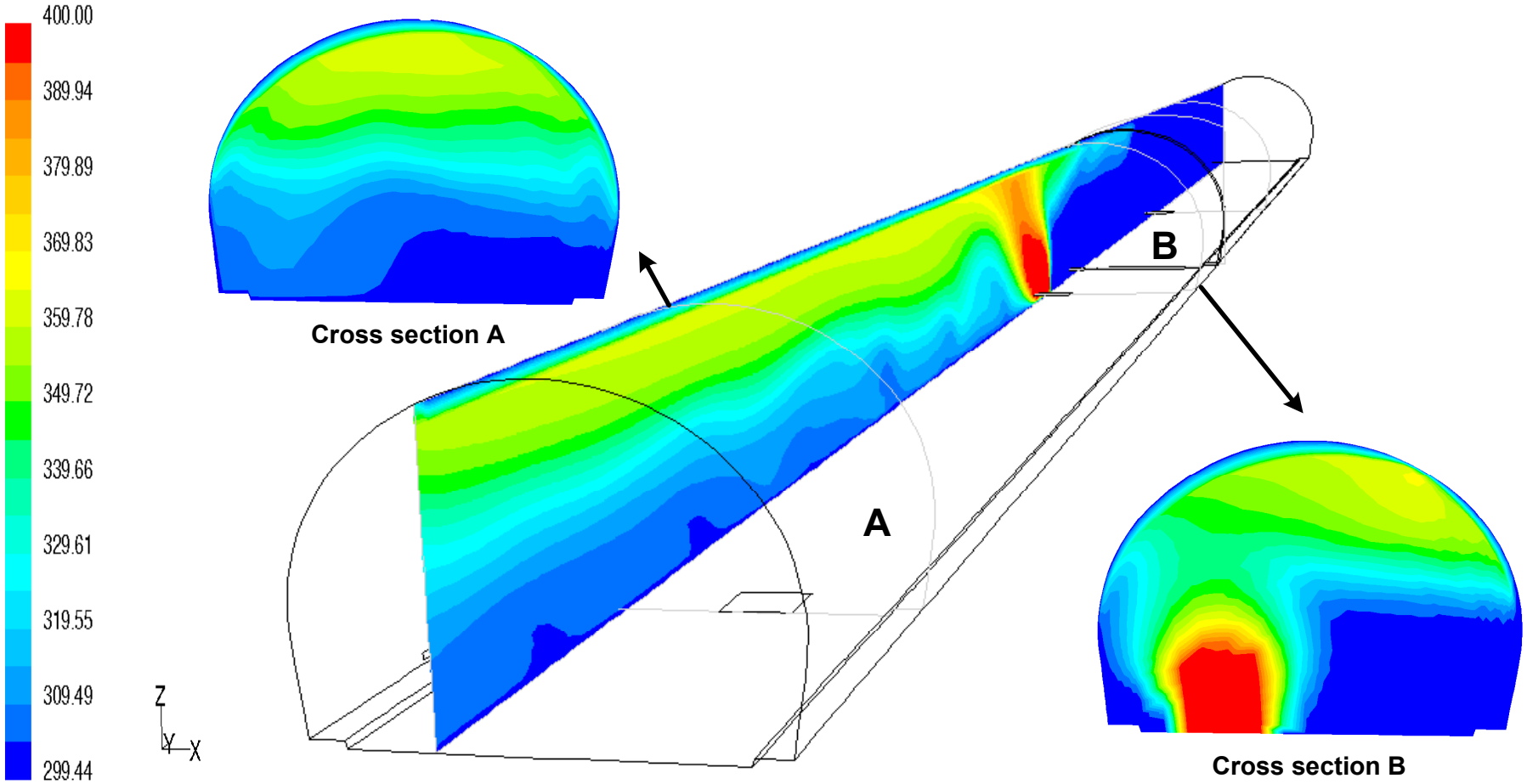

Figure A2.5: *Temperature distribution in different cut planes for scenario A2 (time=200s)*

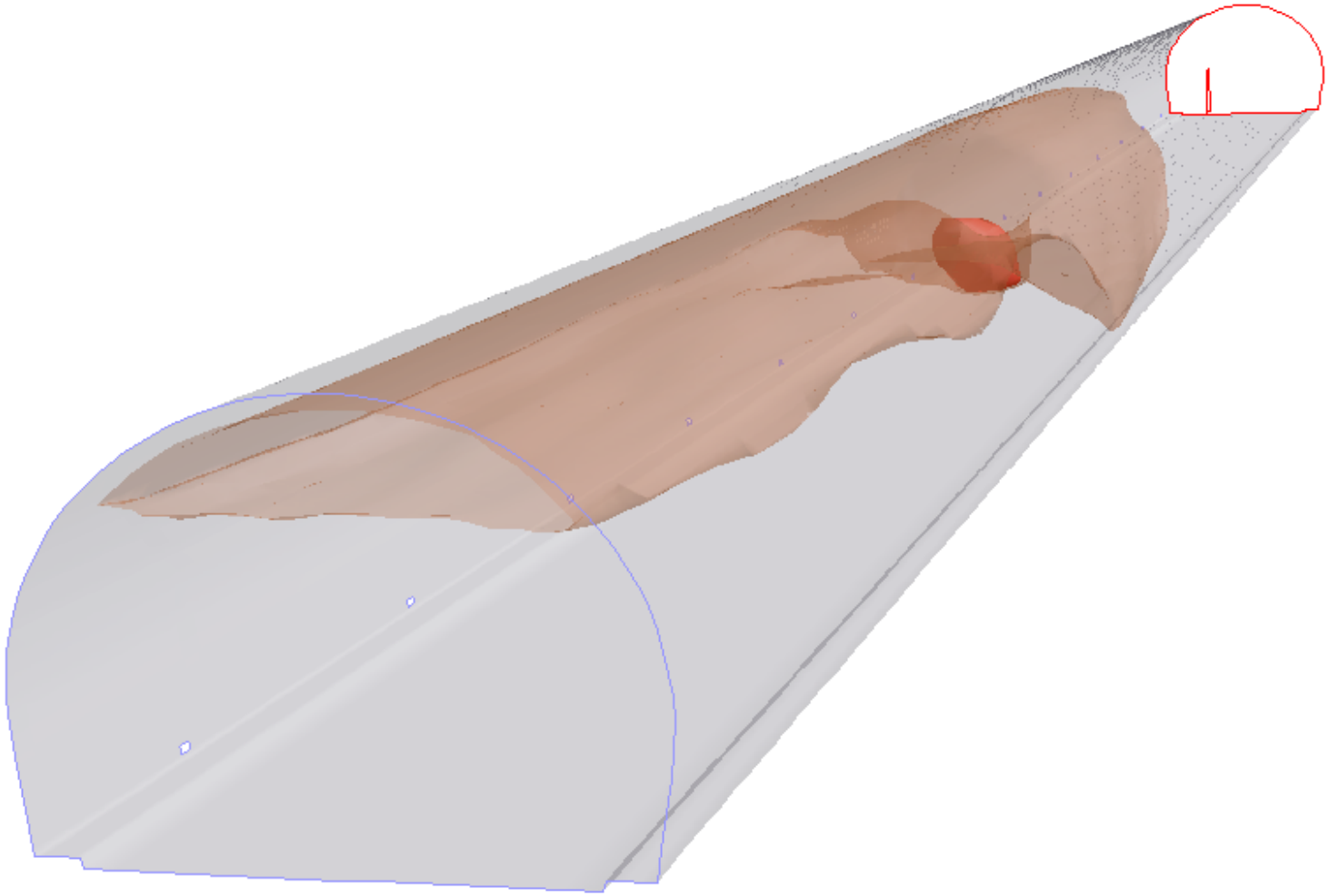

Figure A2.6: *Temperature isosurfaces for 350 [K] and 400 [K] (time=200s)*

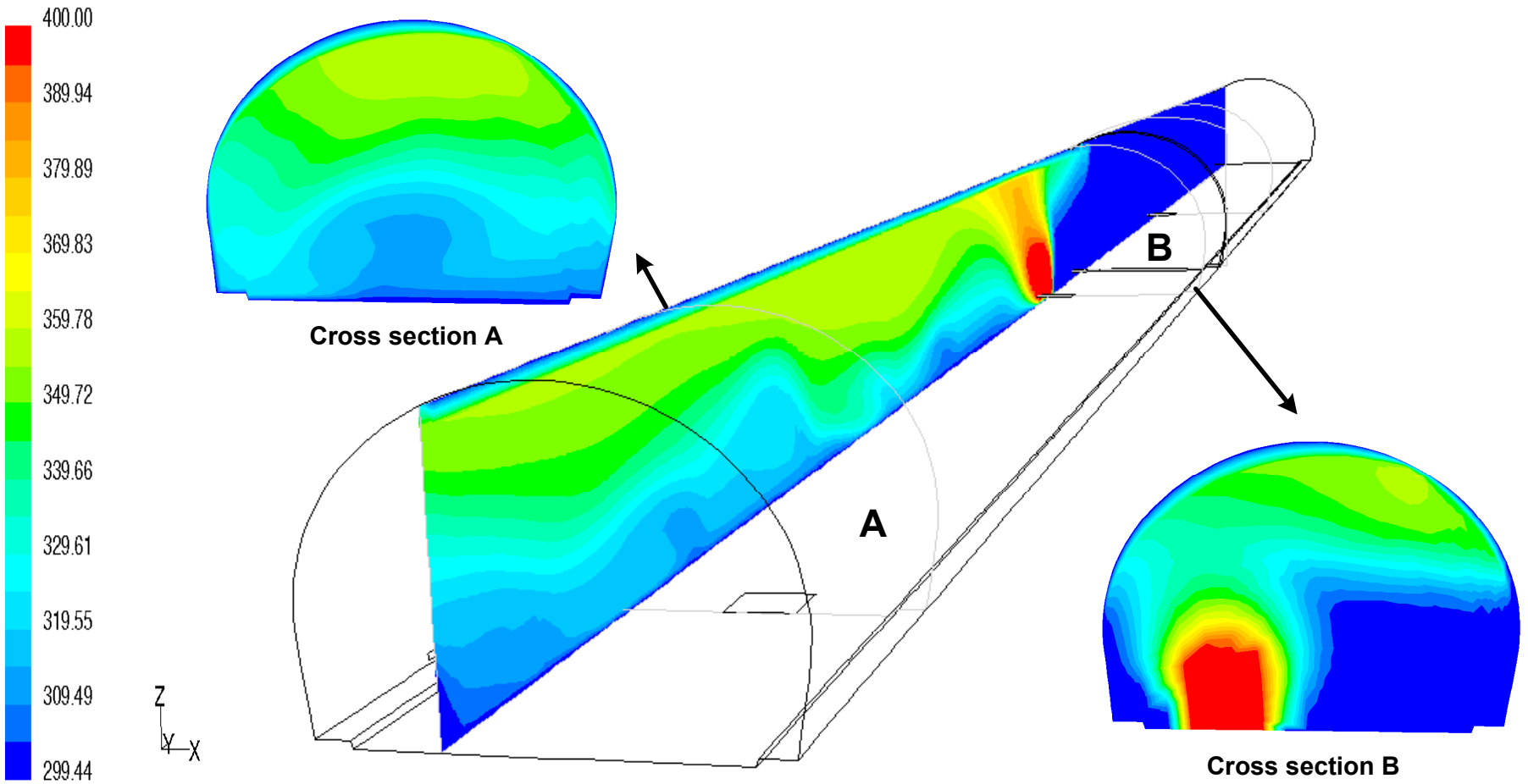

Figure A2.7: *Temperature distribution in different cut planes for scenario A2 (time=300s)*

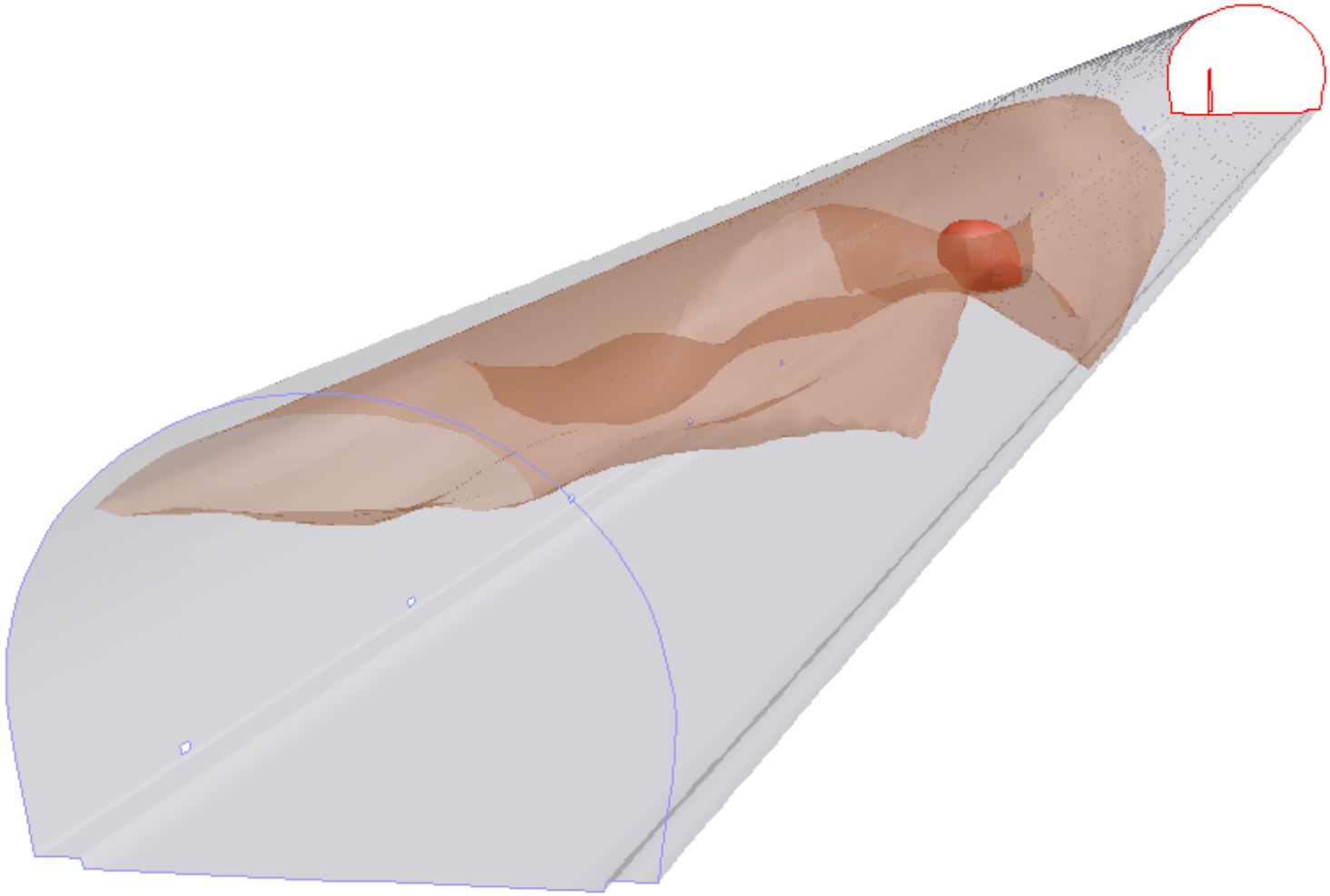

Figure A2.8: *Temperature isosurfaces for 350 [K] and 400 [K] (time=300s)*

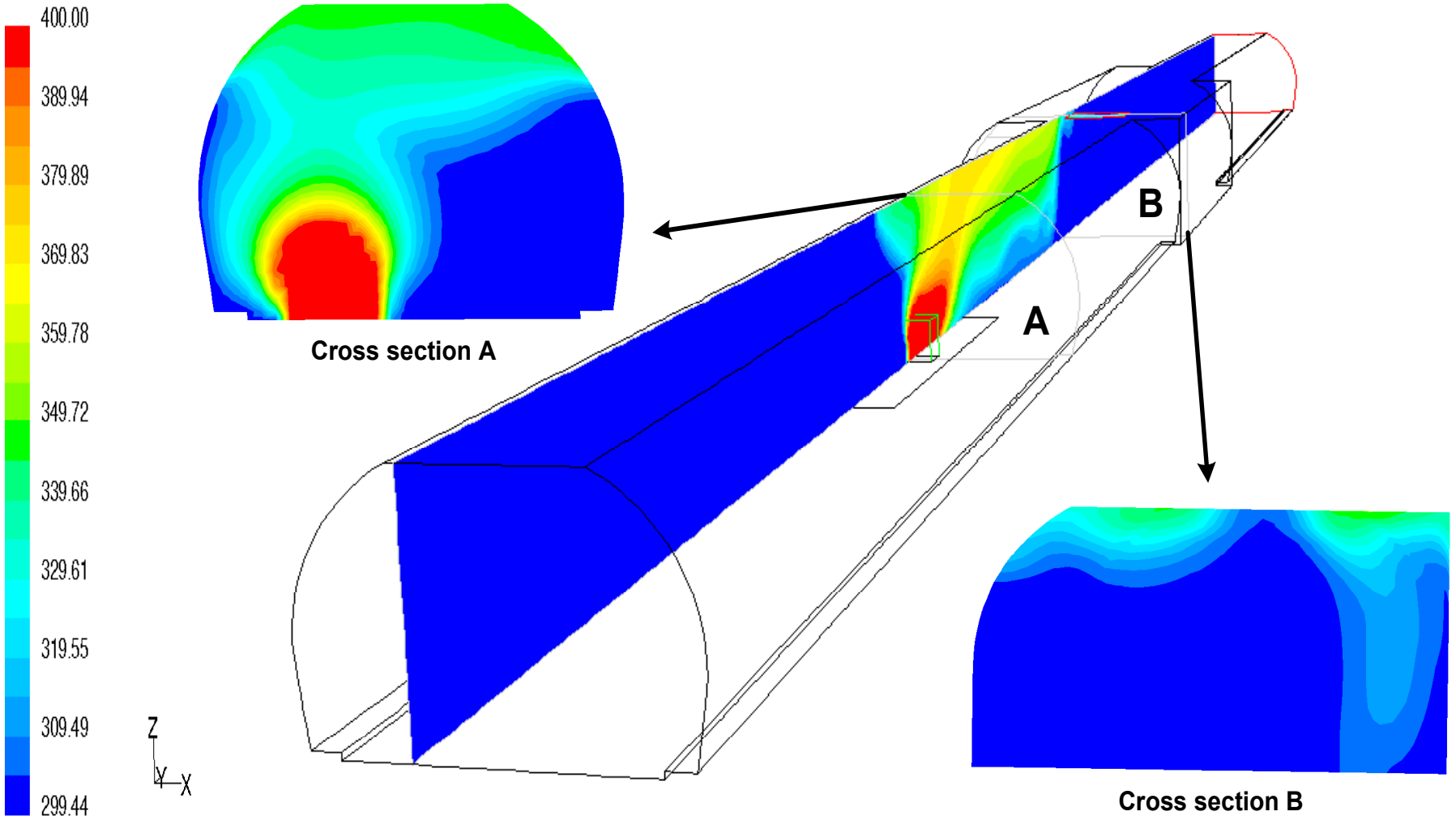

Figure A3.1: *Temperature distribution in different cut planes for scenario A3 (time=50s)*

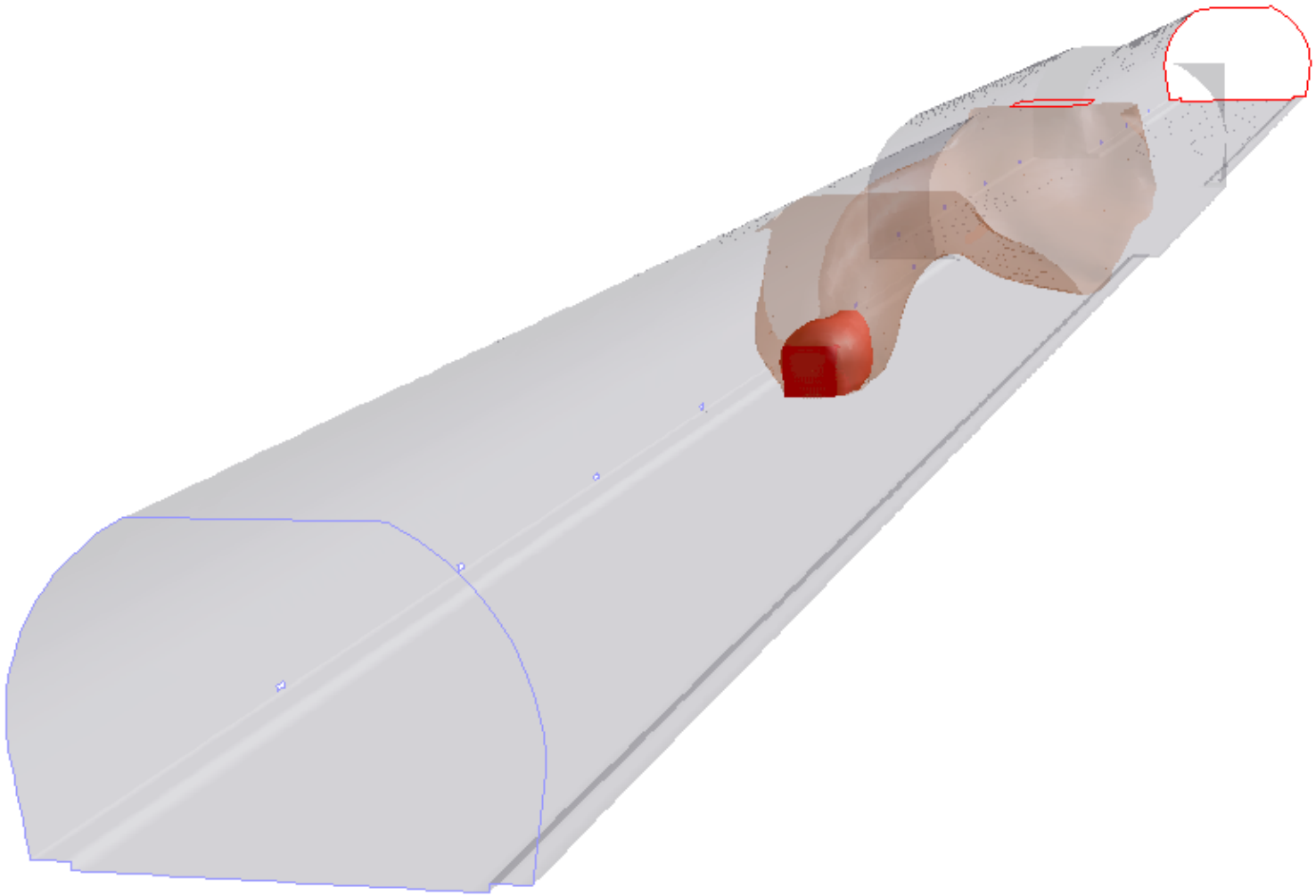

Figure A3.2: *Temperature isosurfaces for 350 [K] and 400 [K] (time=50s)*

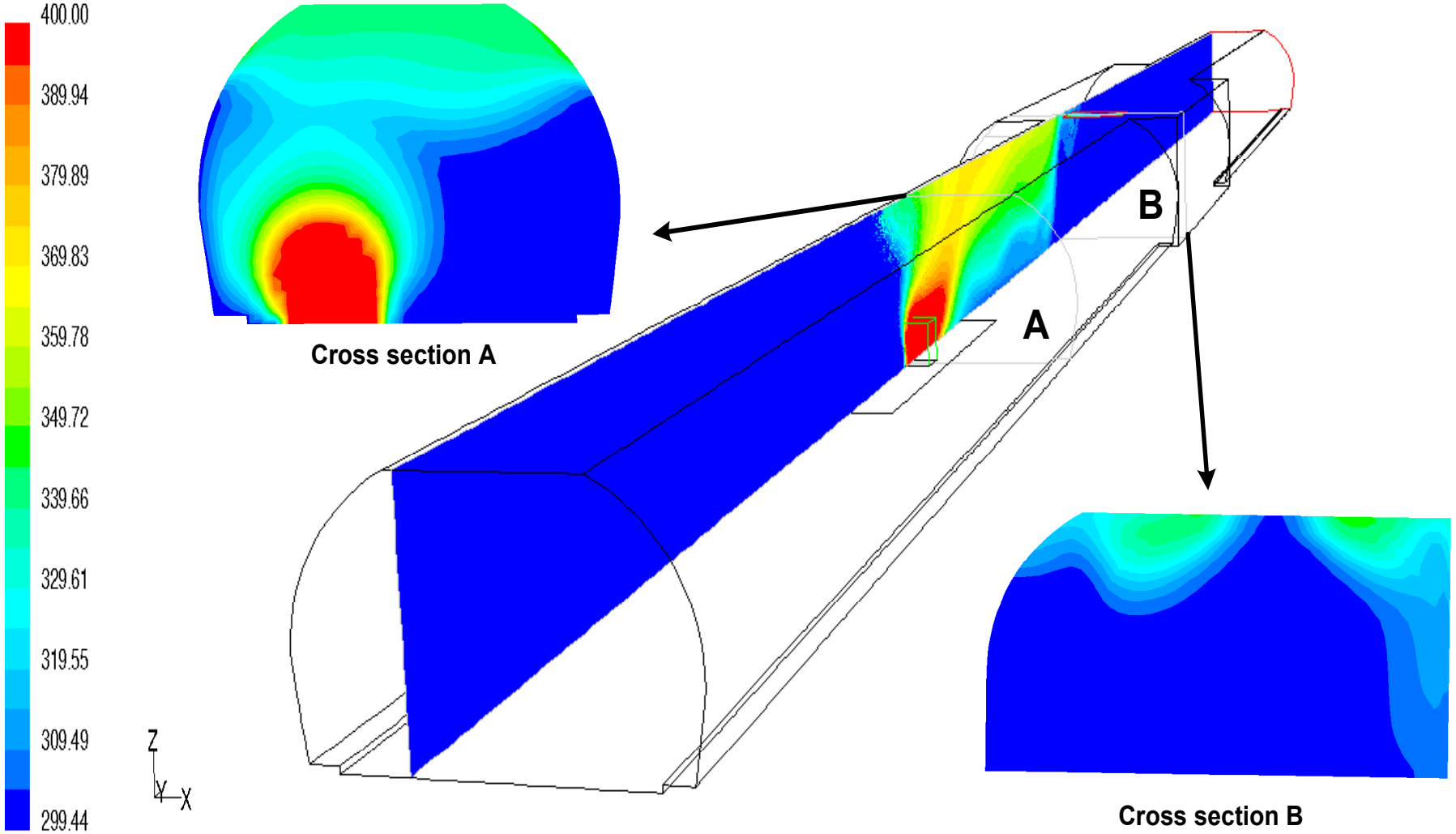

Figure A3.3: *Temperature distribution in different cut planes for scenario A3 (time=100s)*

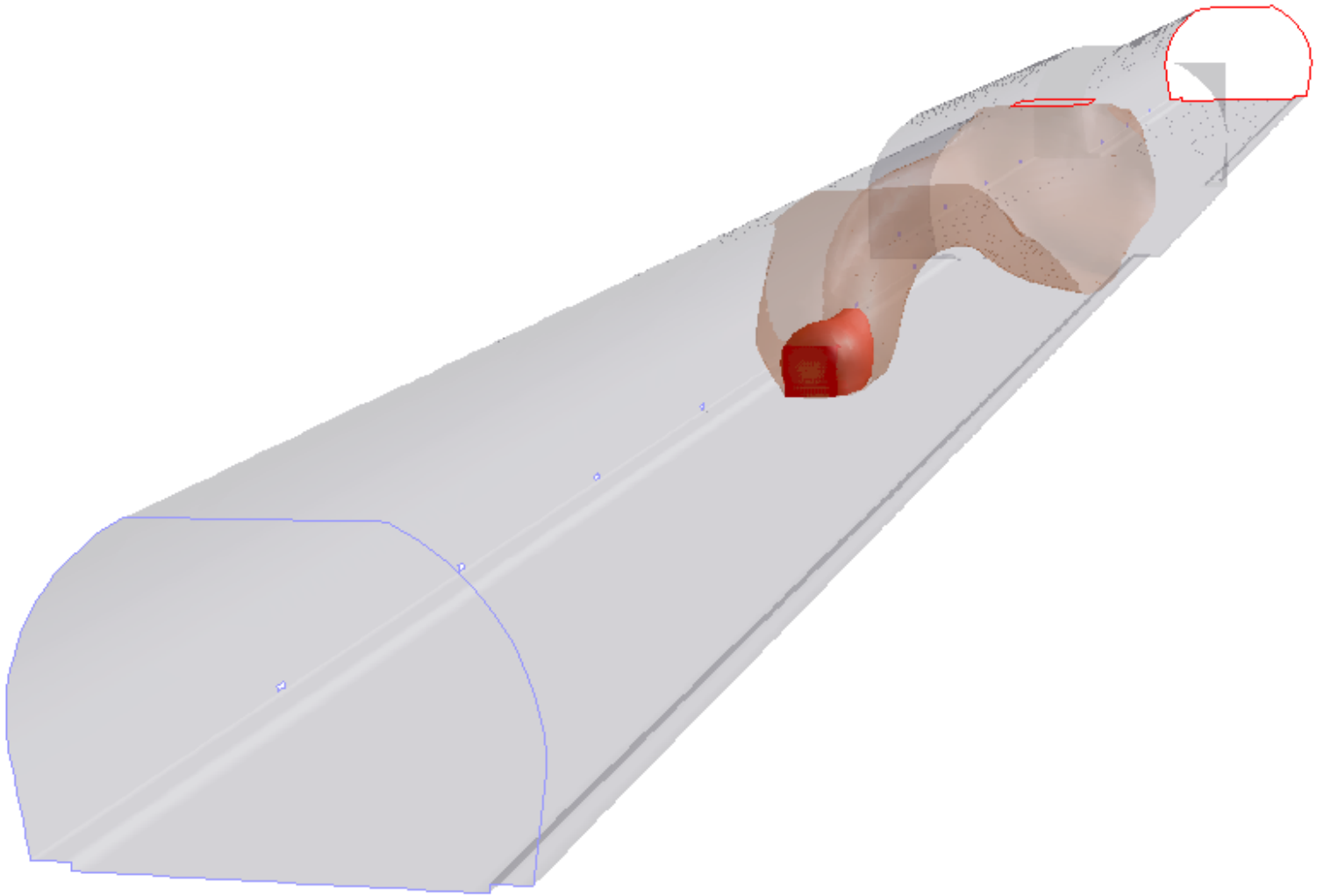

Figure A3.4: *Temperature isosurfaces for 350 [K] and 400 [K] (time=100s)*

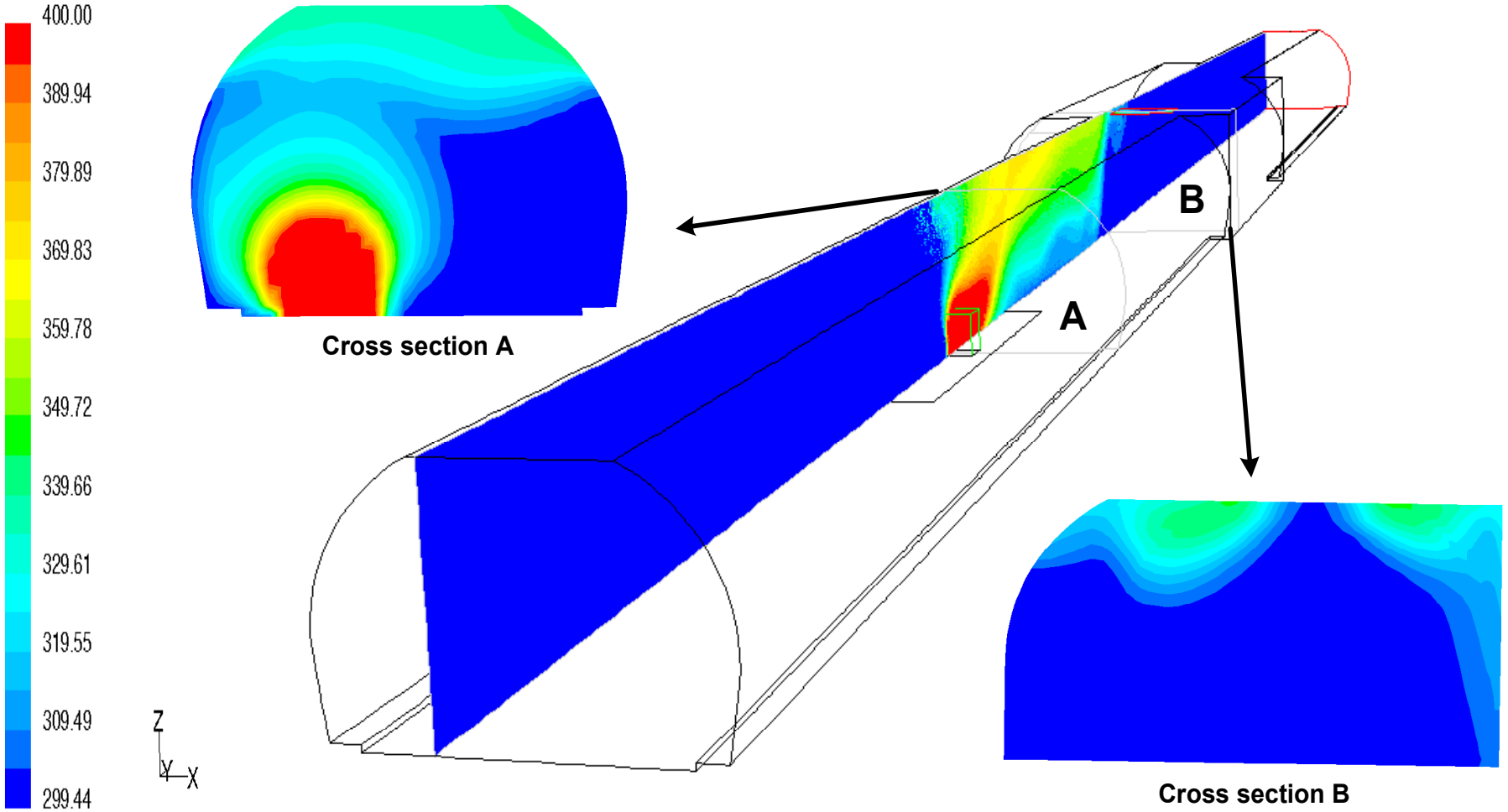

Figure A3.5: *Temperature distribution in different cut planes for scenario A3 (time=200s)*

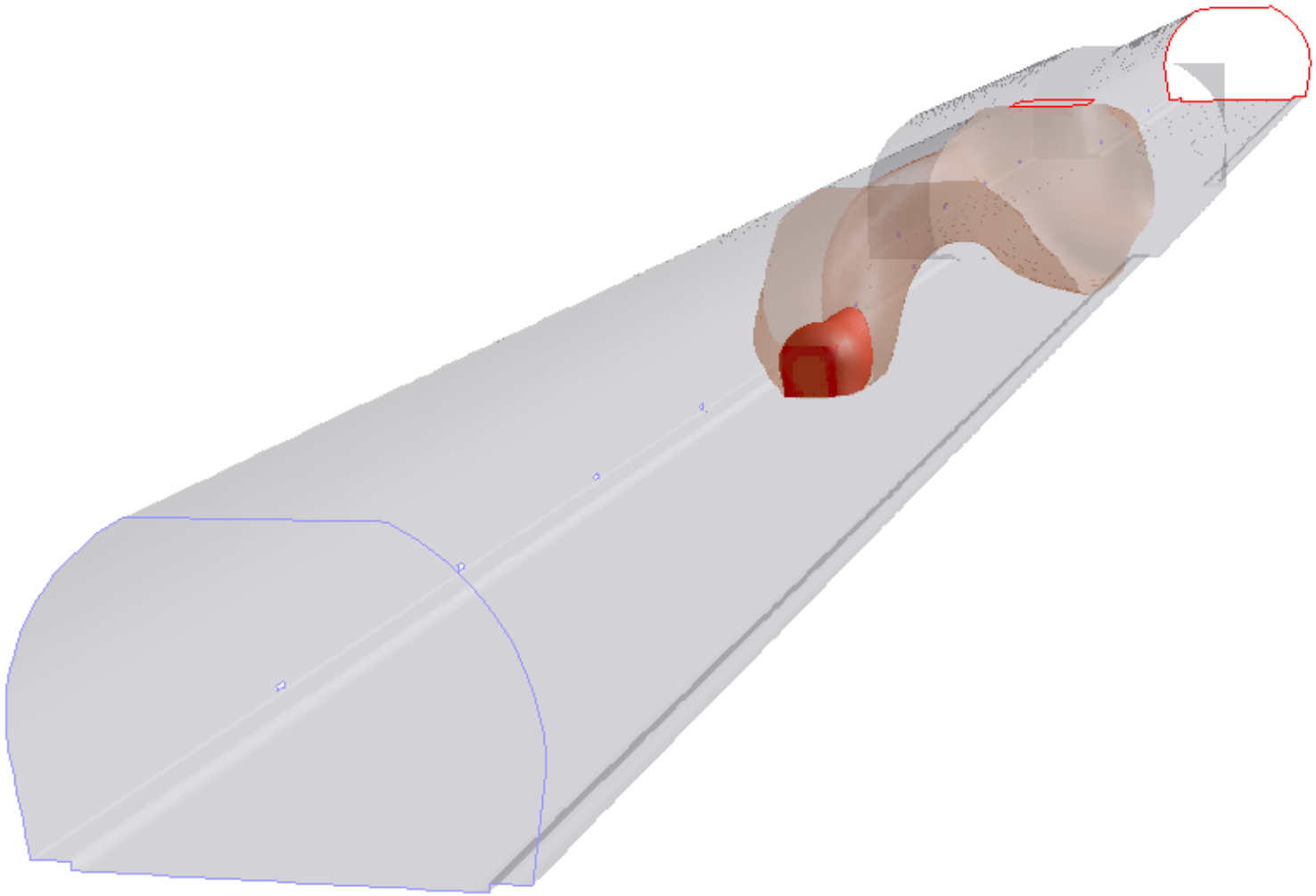

Figure A3.6: *Temperature isosurfaces for 350 [K] and 400 [K] (time=200s)*

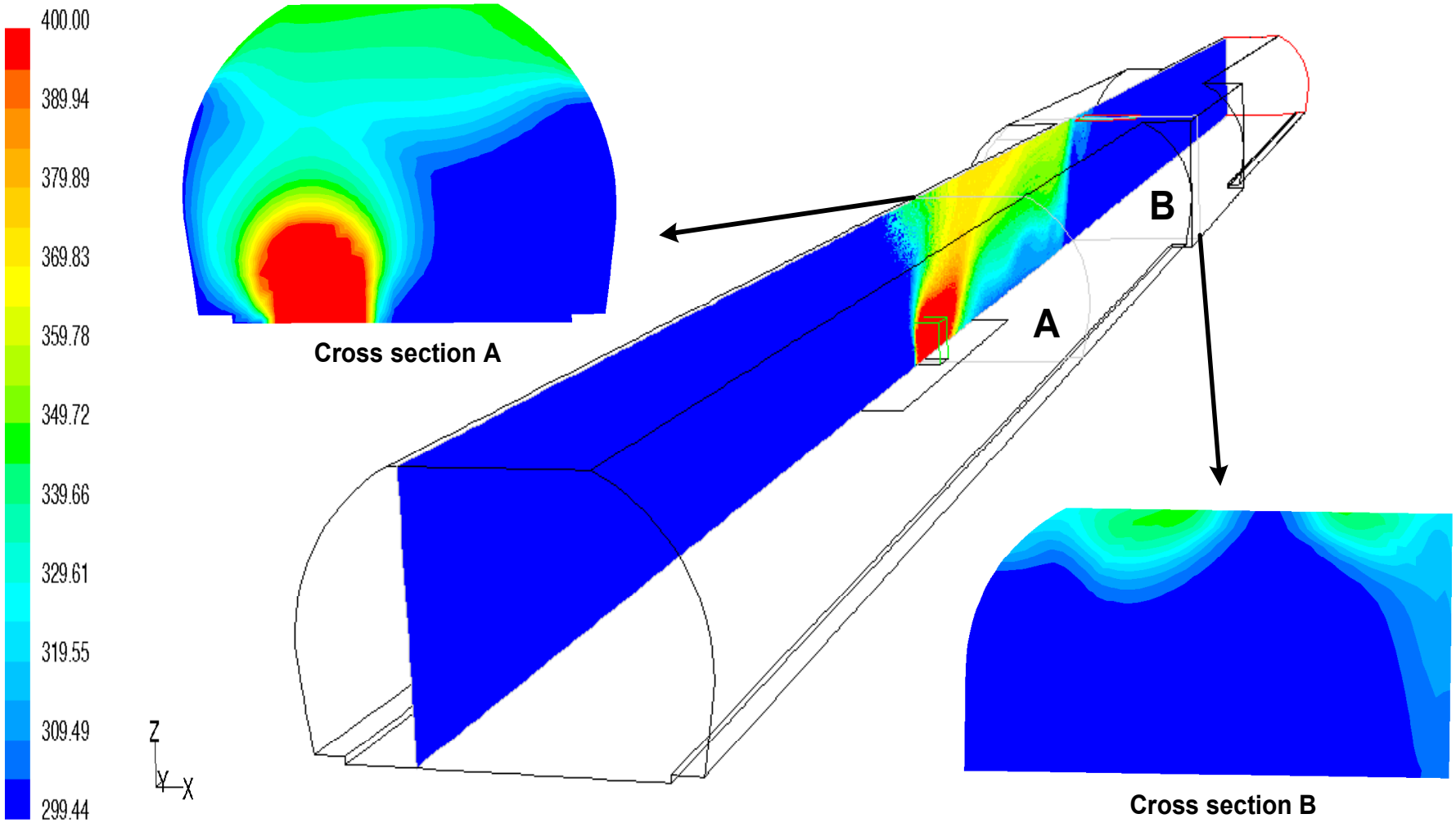

Figure A3.7: *Temperature distribution in different cut planes for scenario A3 (time=300s)*

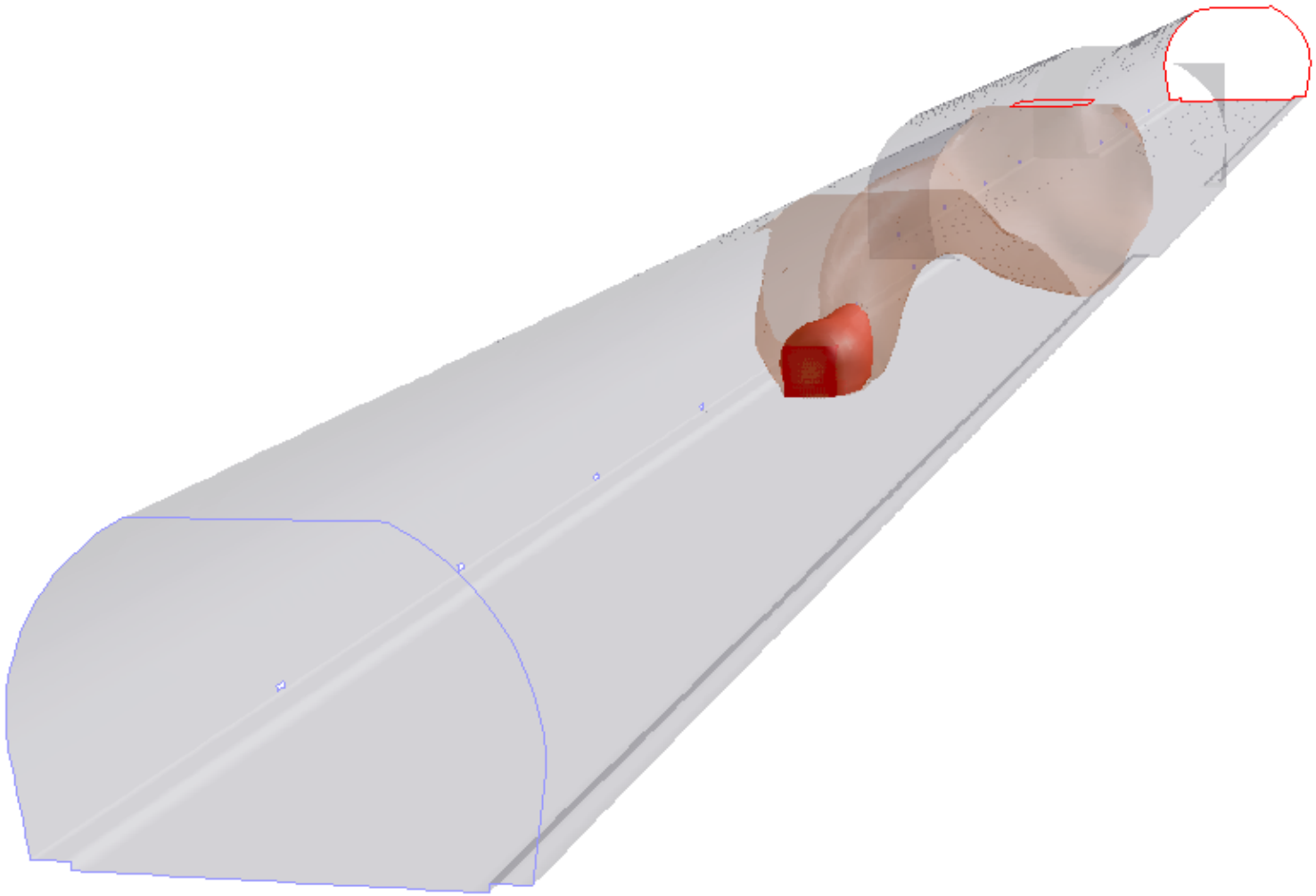

Figure A3.8: *Temperature isosurfaces for 350 [K] and 400 [K] (time=300s)*

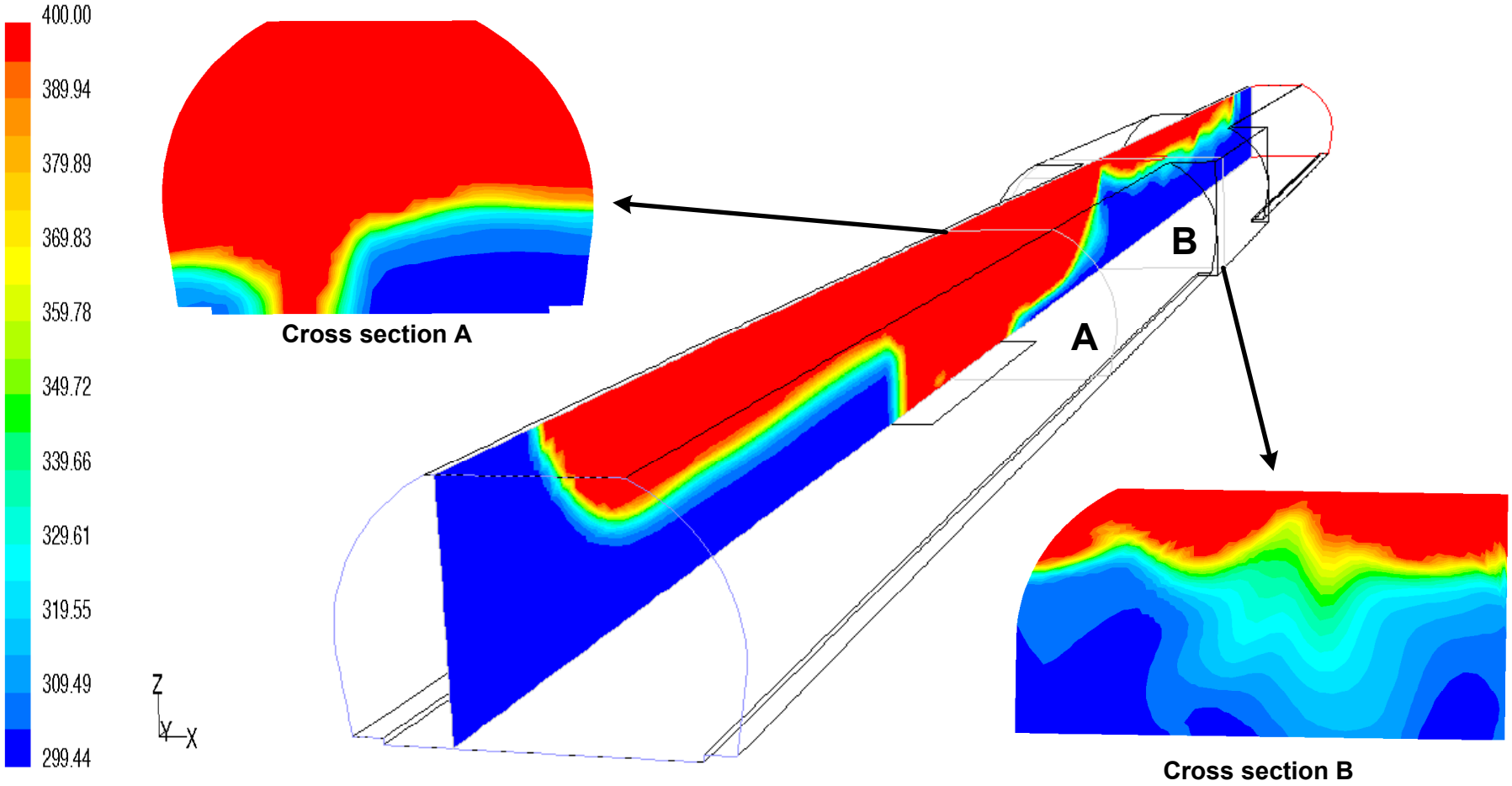

Figure A4.1: *Temperature distribution in different cut planes for scenario A4 (time=50s)*

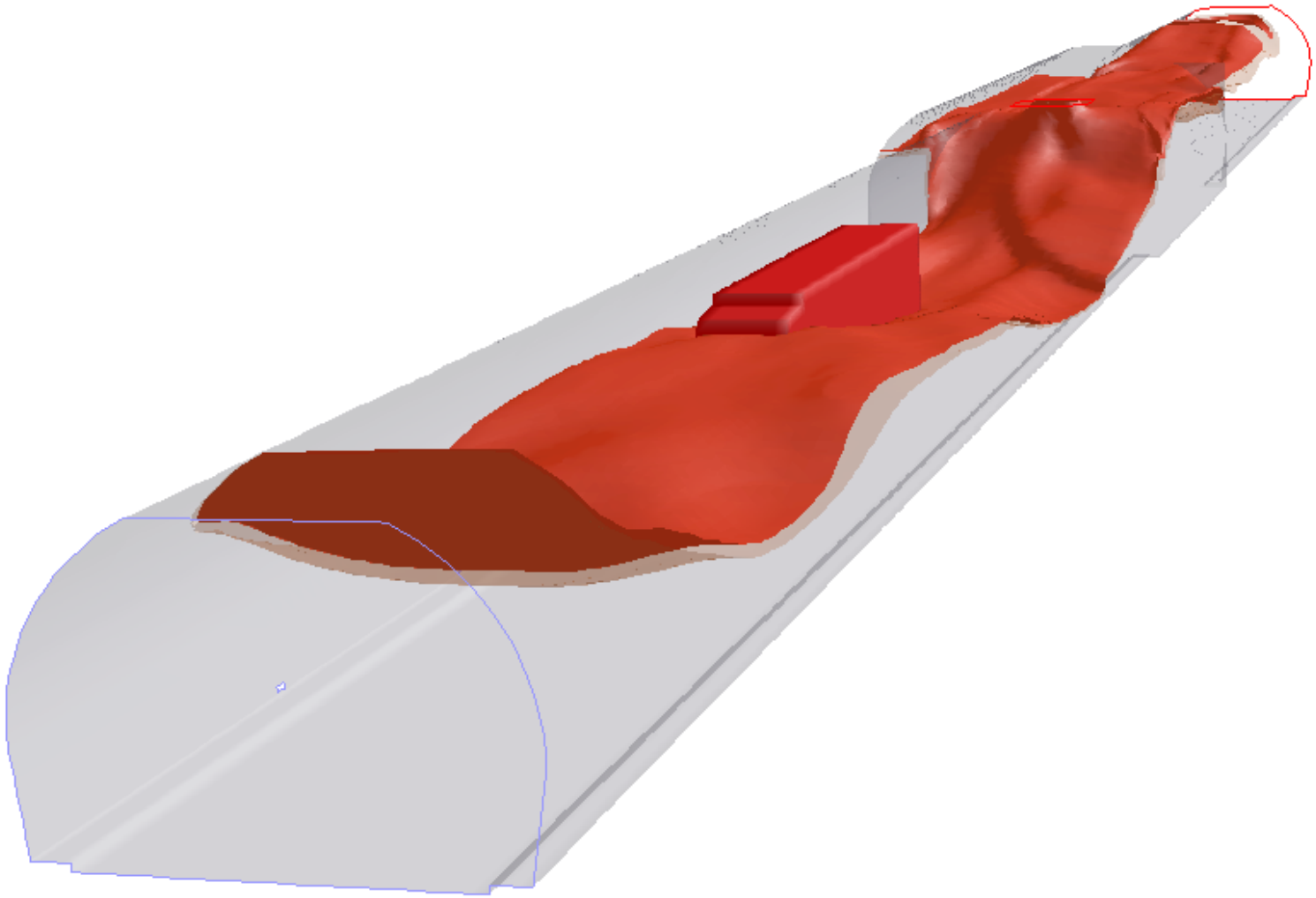

Figure A4.2: *Temperature isosurfaces for 350 [K] and 400 [K] (time=50s)*

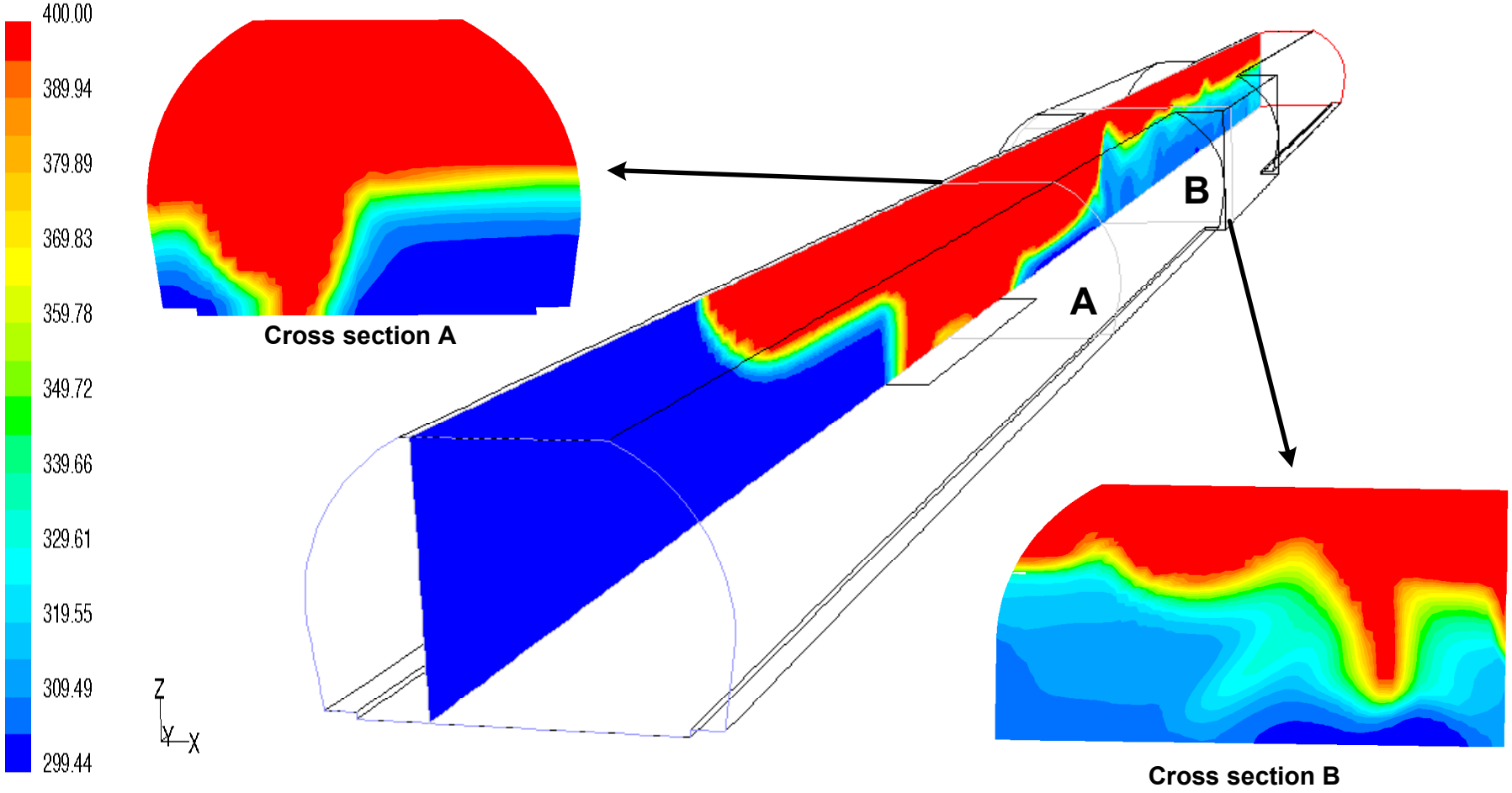

Figure A4.3: *Temperature distribution in different cut planes for scenario A4 (time=100s)*

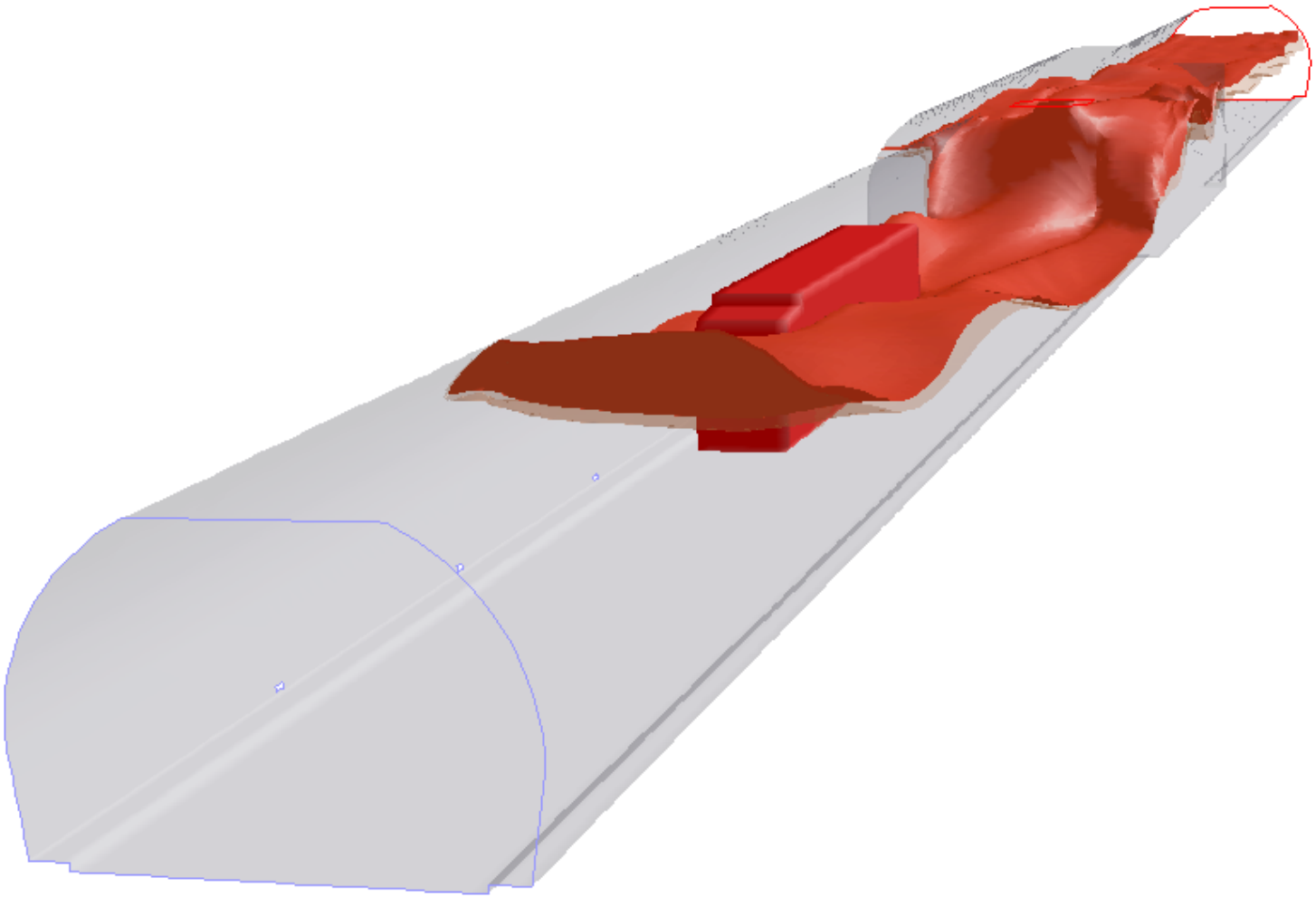

Figure A4.4: *Temperature isosurfaces for 350 [K] and 400 [K] (time=100s)*

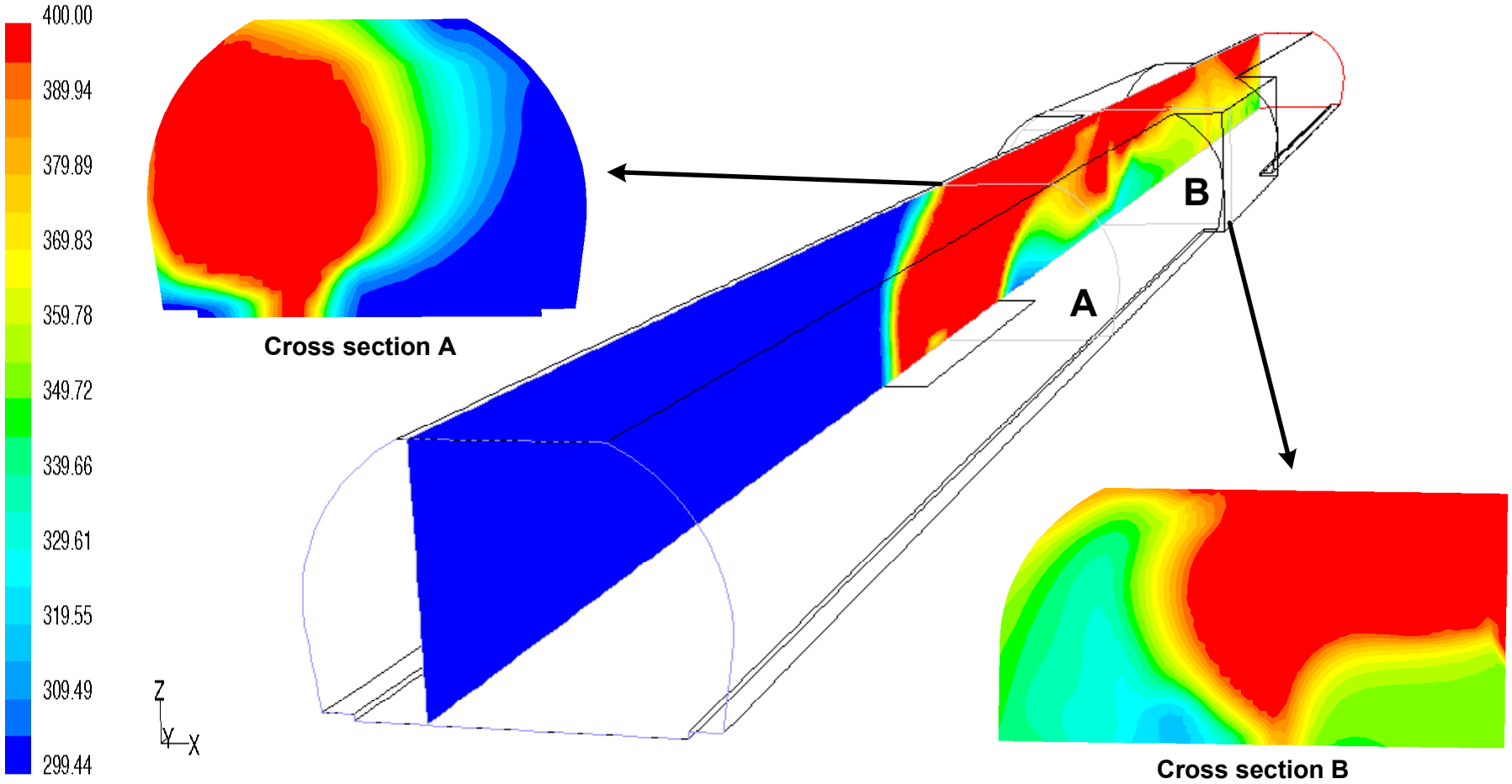

Figure A4.5: *Temperature distribution in different cut planes for scenario A4 (time=200s)*

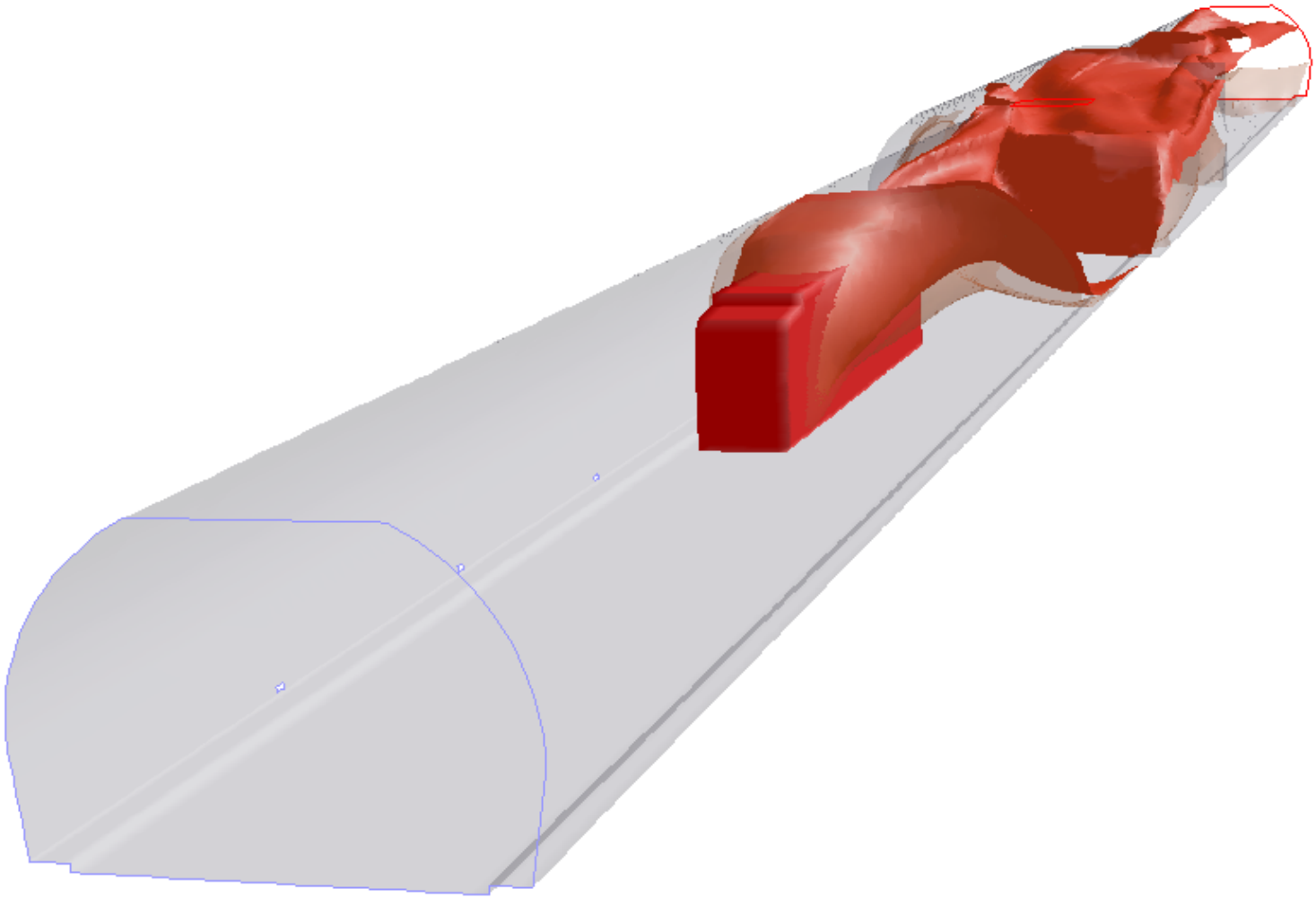

Figure A4.6: *Temperature isosurfaces for 350 [K] and 400 [K] (time=200s)*

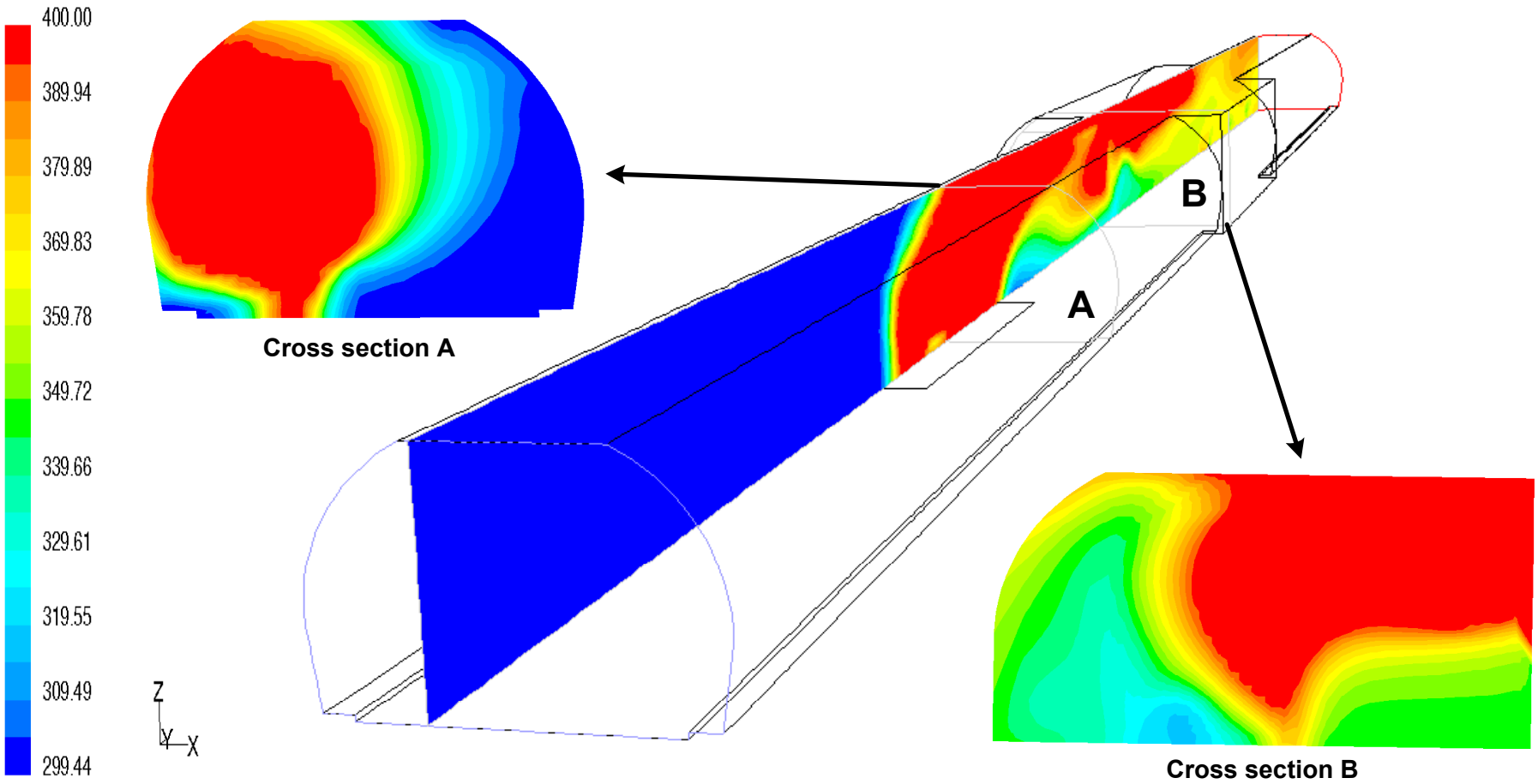

Figure A4.7: *Temperature distribution in different cut planes for scenario A4 (time=300s)*

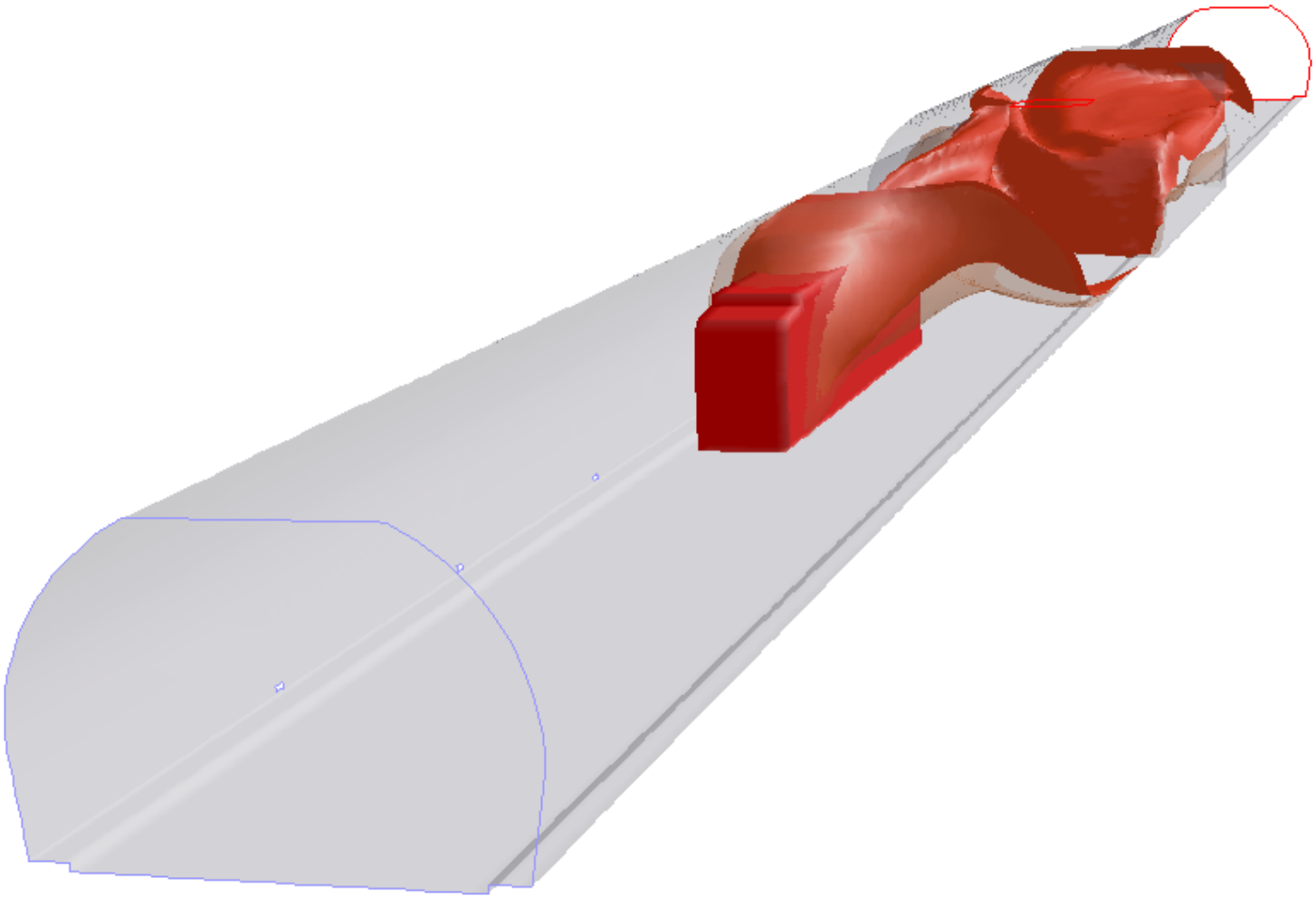

Figure A4.8: *Temperature isosurfaces for 350 [K] and 400 [K] (time=300s)*

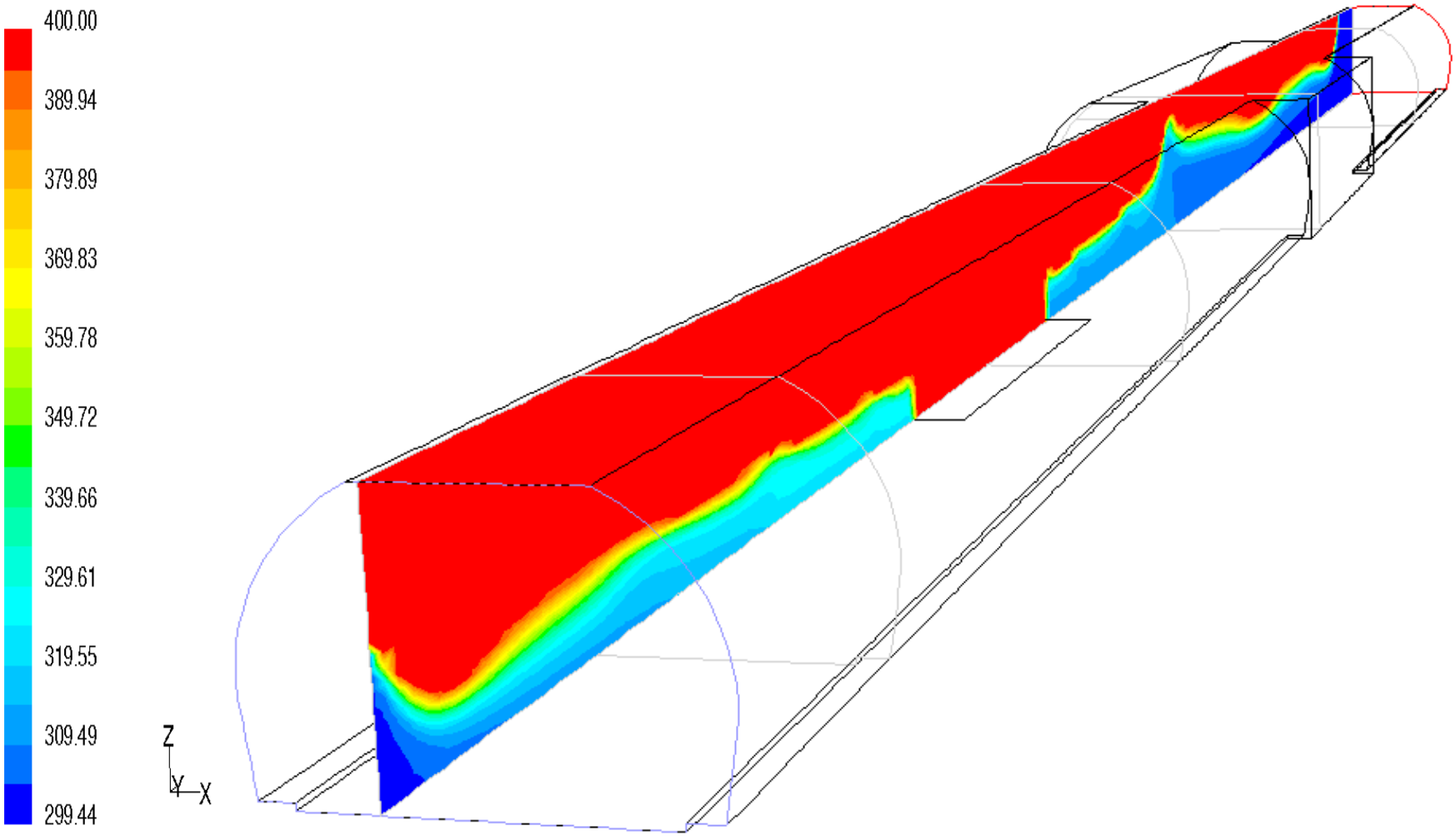

Figure A5.1: *Temperature distribution in different cut planes for scenario A5 (time=50s)*

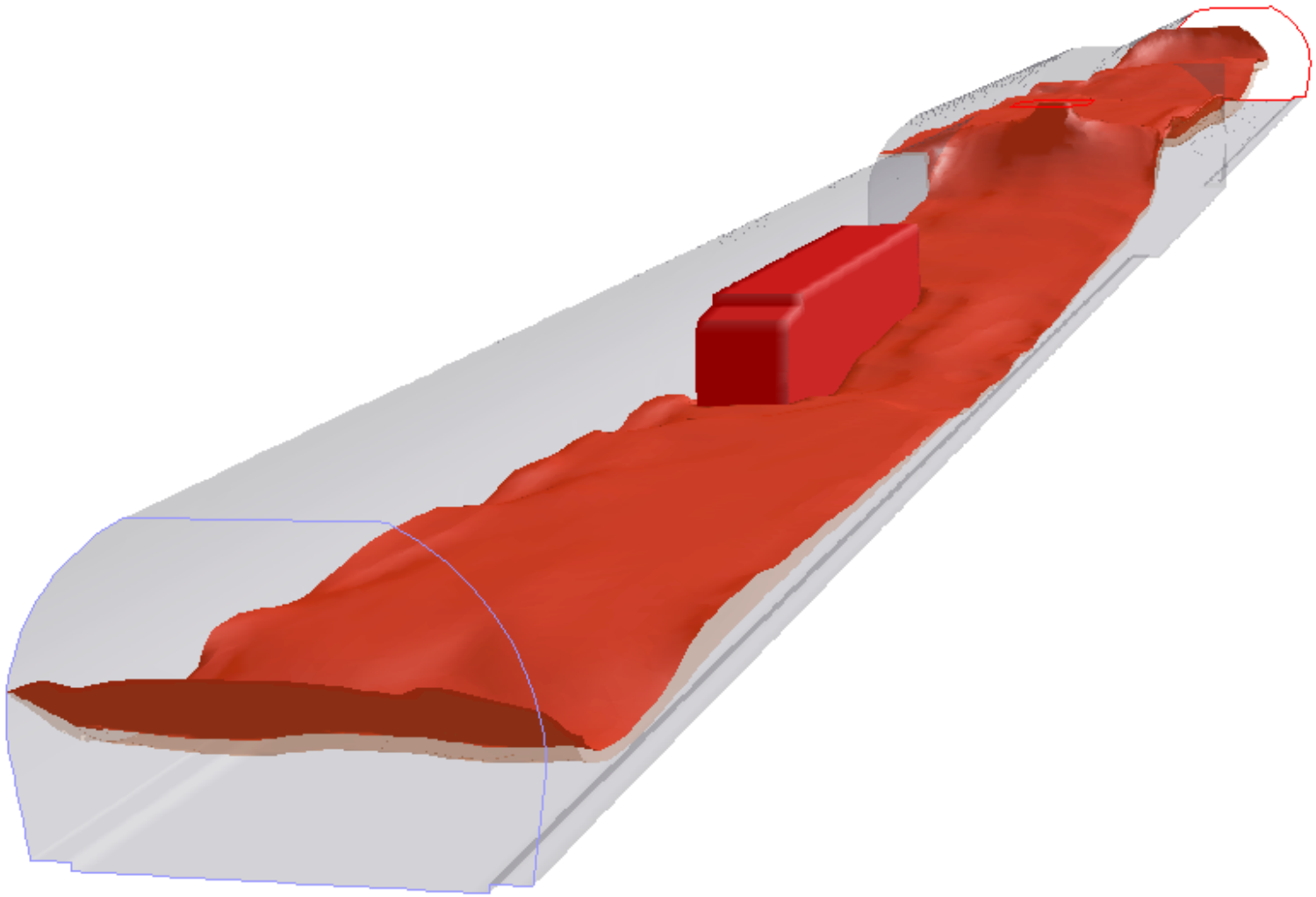

Figure A5.2: *Temperature isosurfaces for 350 [K] and 400 [K] (time=50s)*

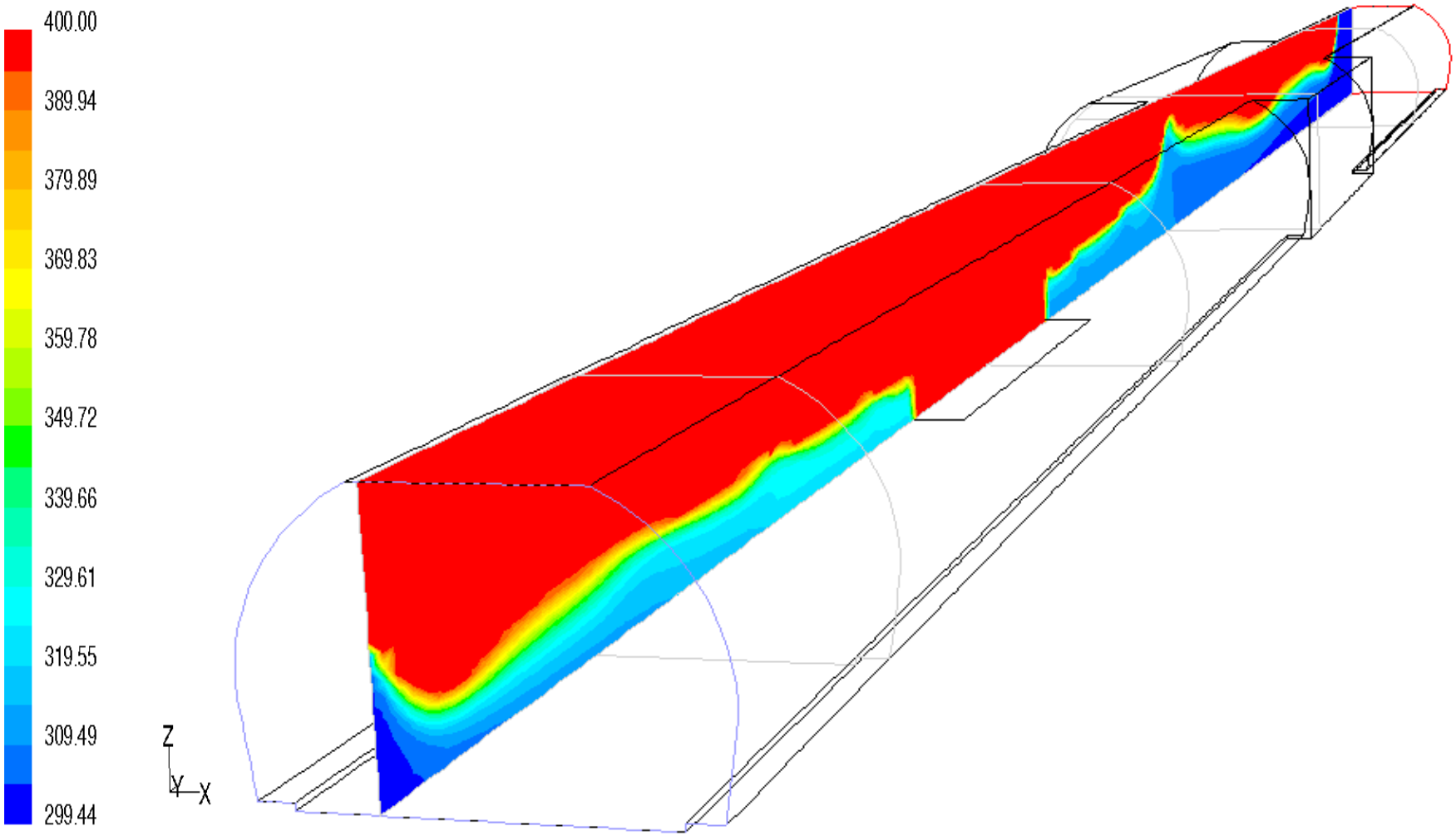

Figure A5.3: *Temperature distribution in different cut planes for scenario A5 (time=100s)*

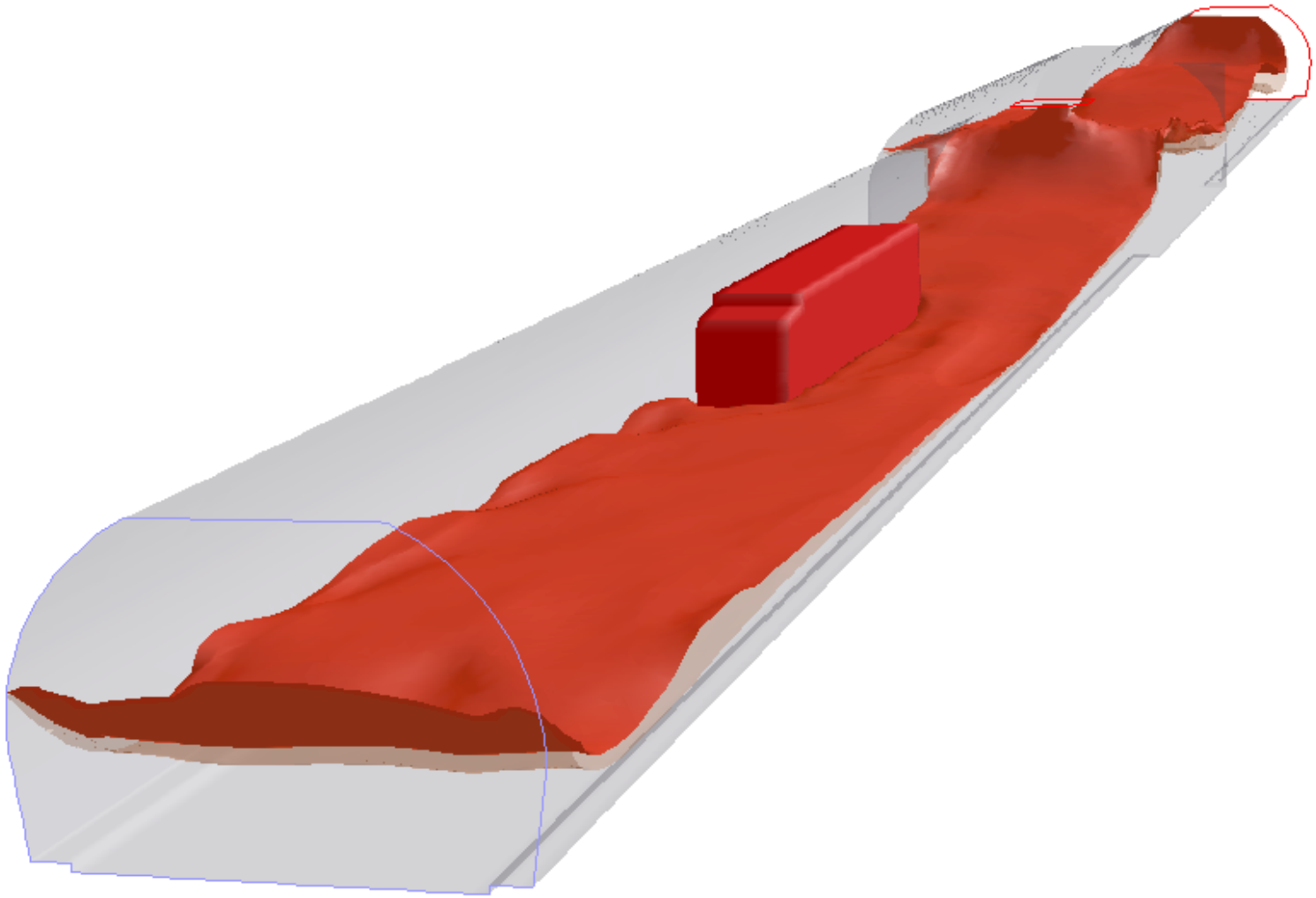

Figure A5.4: *Temperature isosurfaces for 350 [K] and 400 [K] (time=100s)*

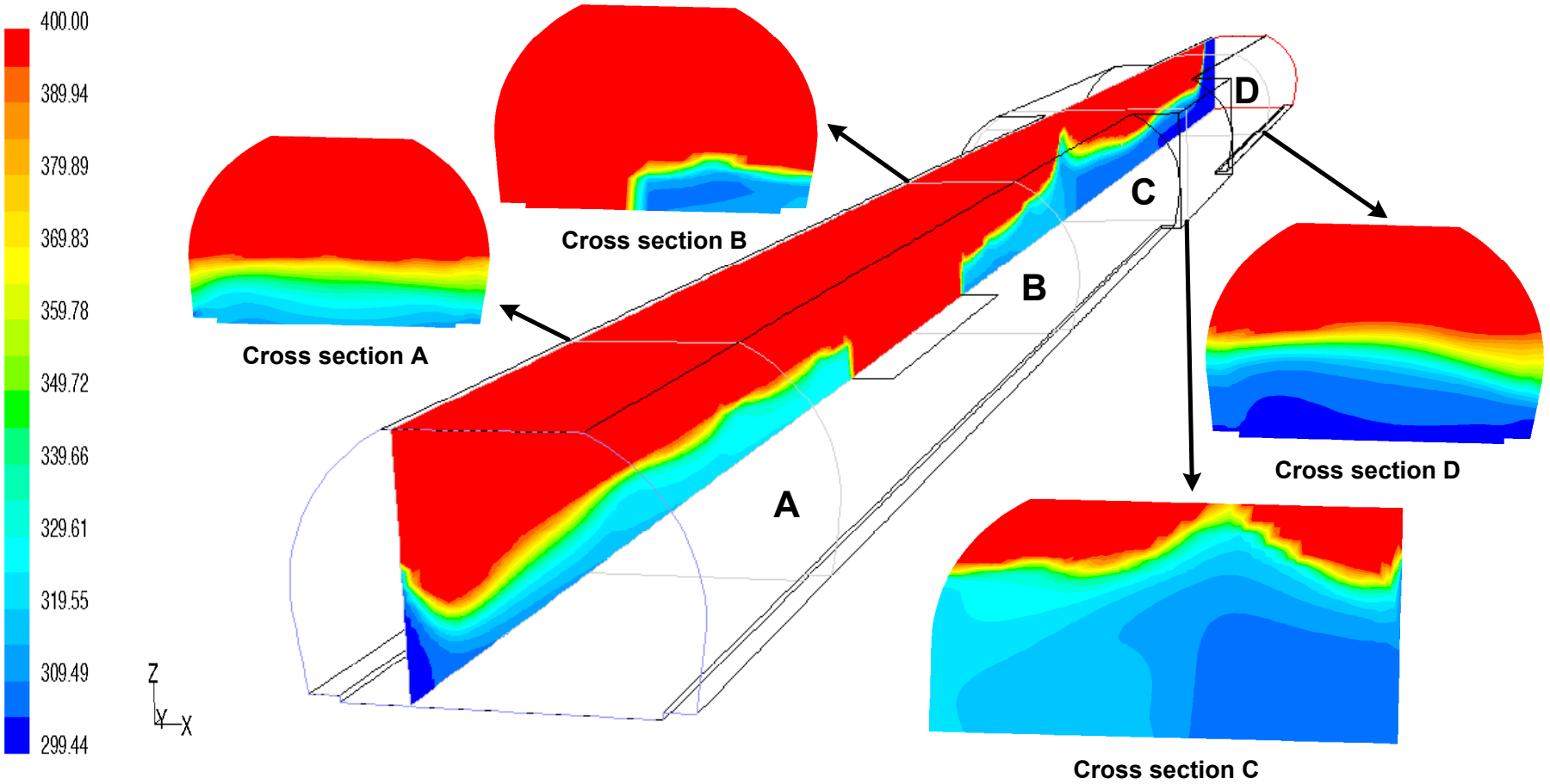

Figure A5.5: *Temperature distribution in different cut planes for scenario A5 (time=200s)*

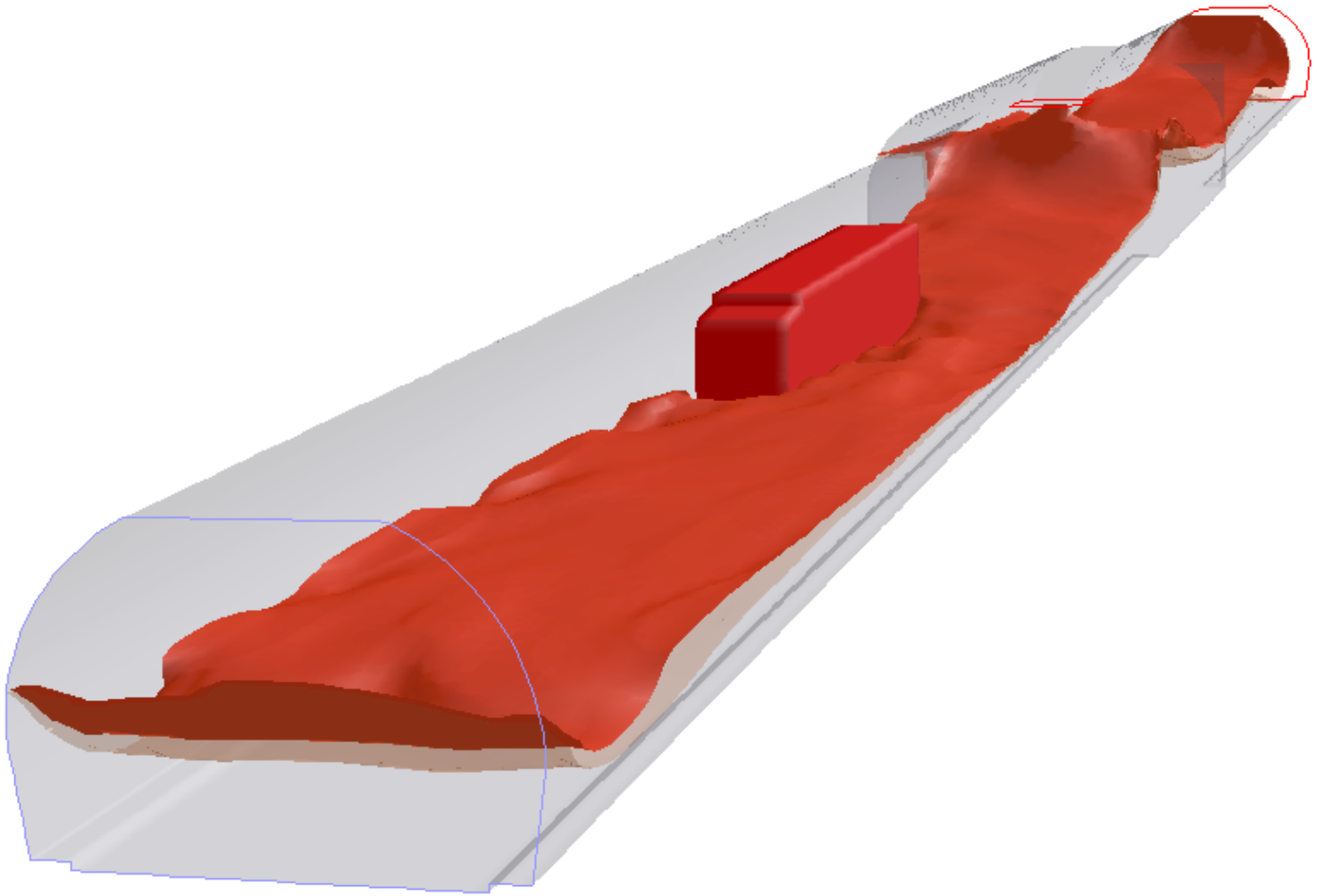

Figure A5.6: *Temperature isosurfaces for 350 [K] and 400 [K] (time=200s)*

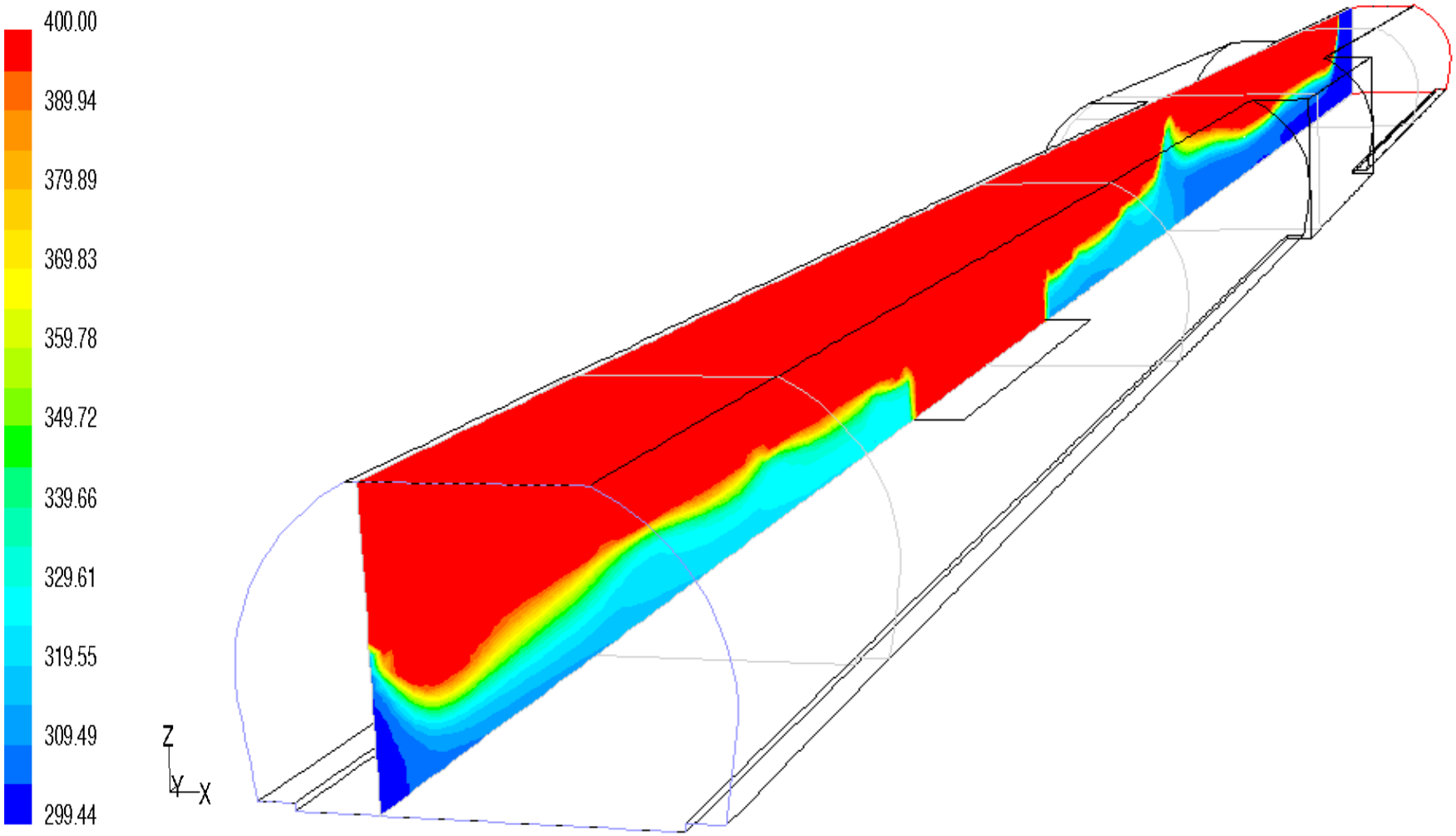

Figure A5.7: *Temperature distribution in different cut planes for scenario A5 (time=300s)*

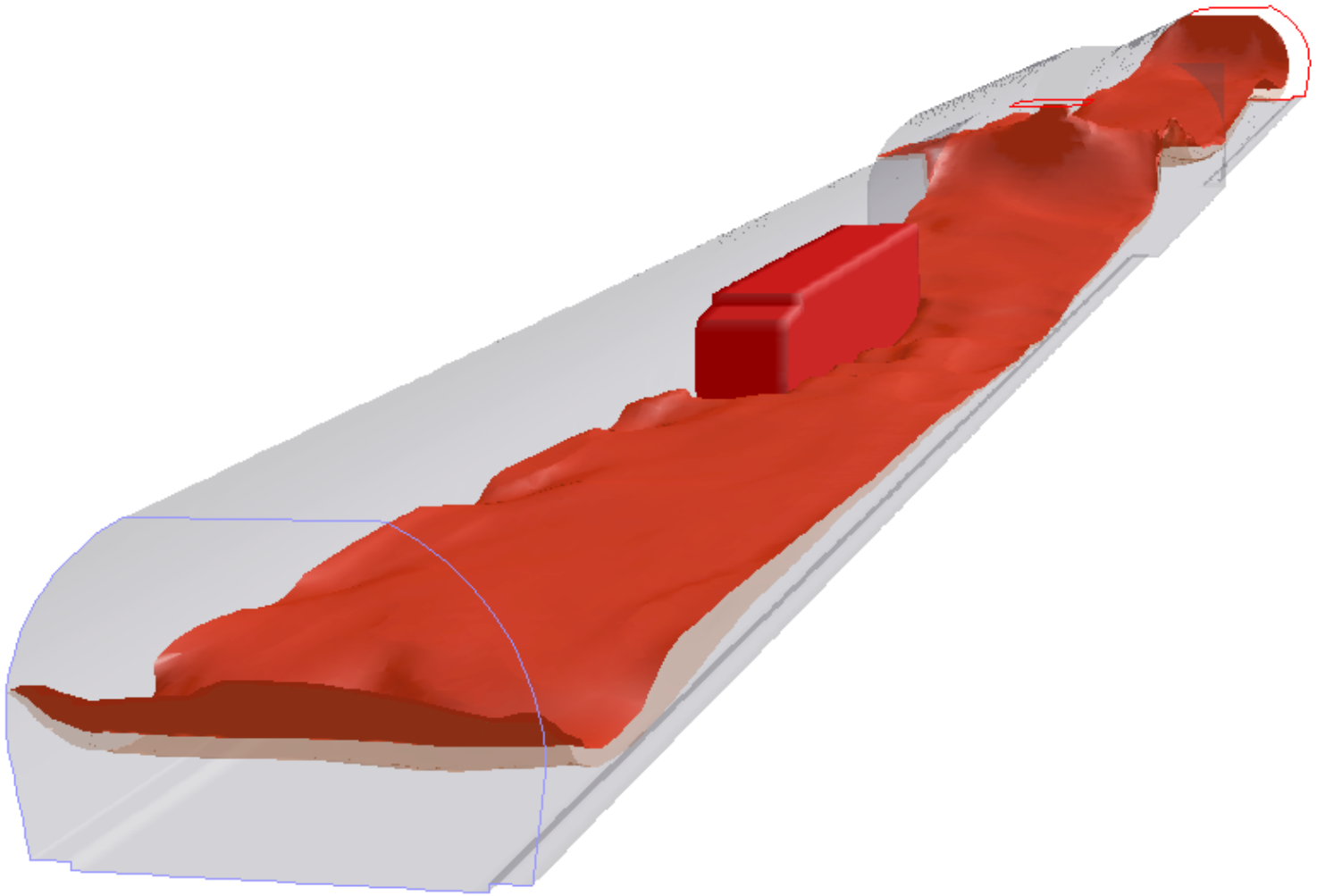

Figure A5.8: *Temperature isosurfaces for 350 [K] and 400 [K] (time=300s)*

GLEINALM TUNNEL FIRE SIMULATIONS

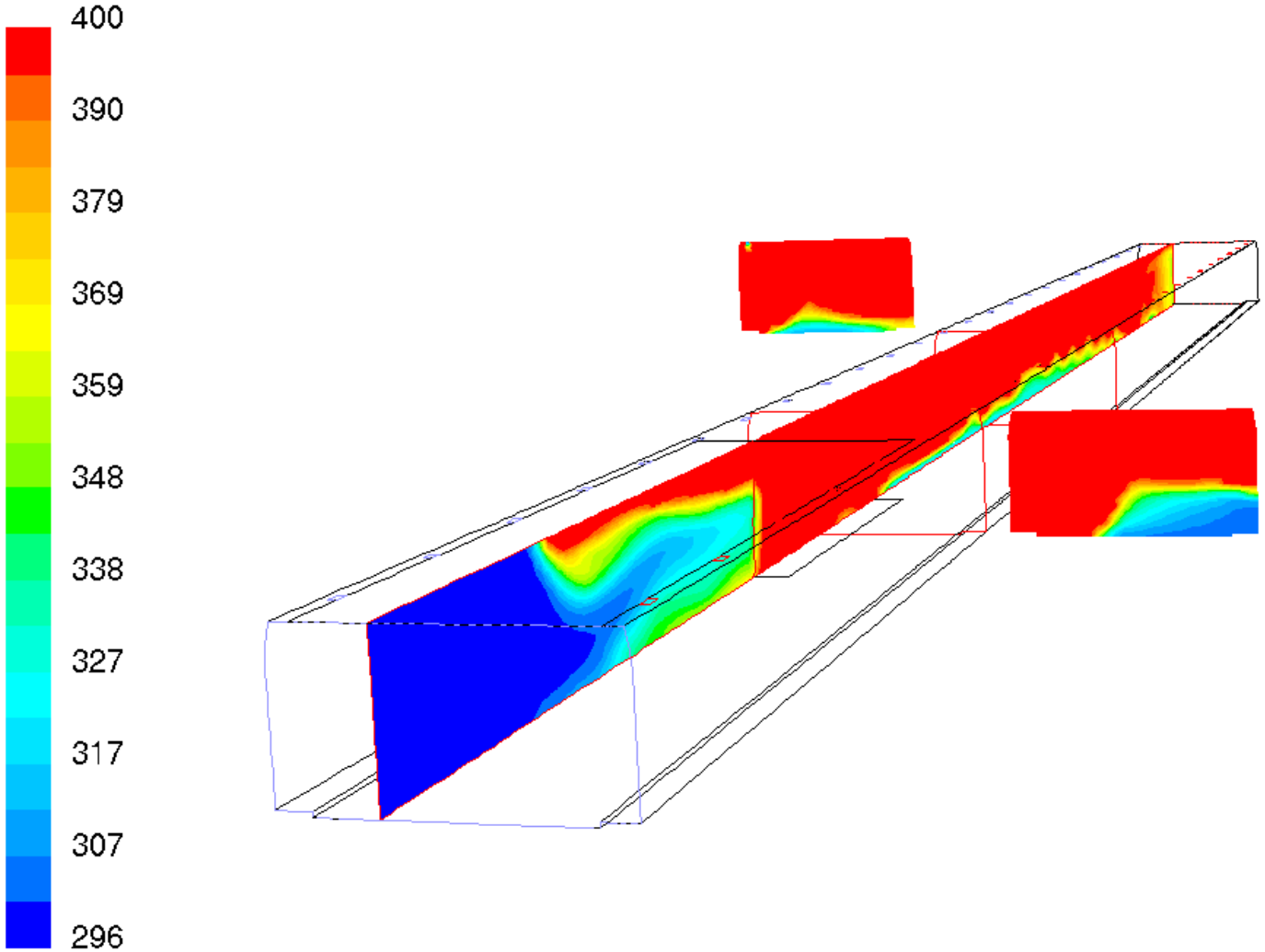

Figure B1.1: *Temperature distribution in different cut planes for scenario B1 (time=50s)*

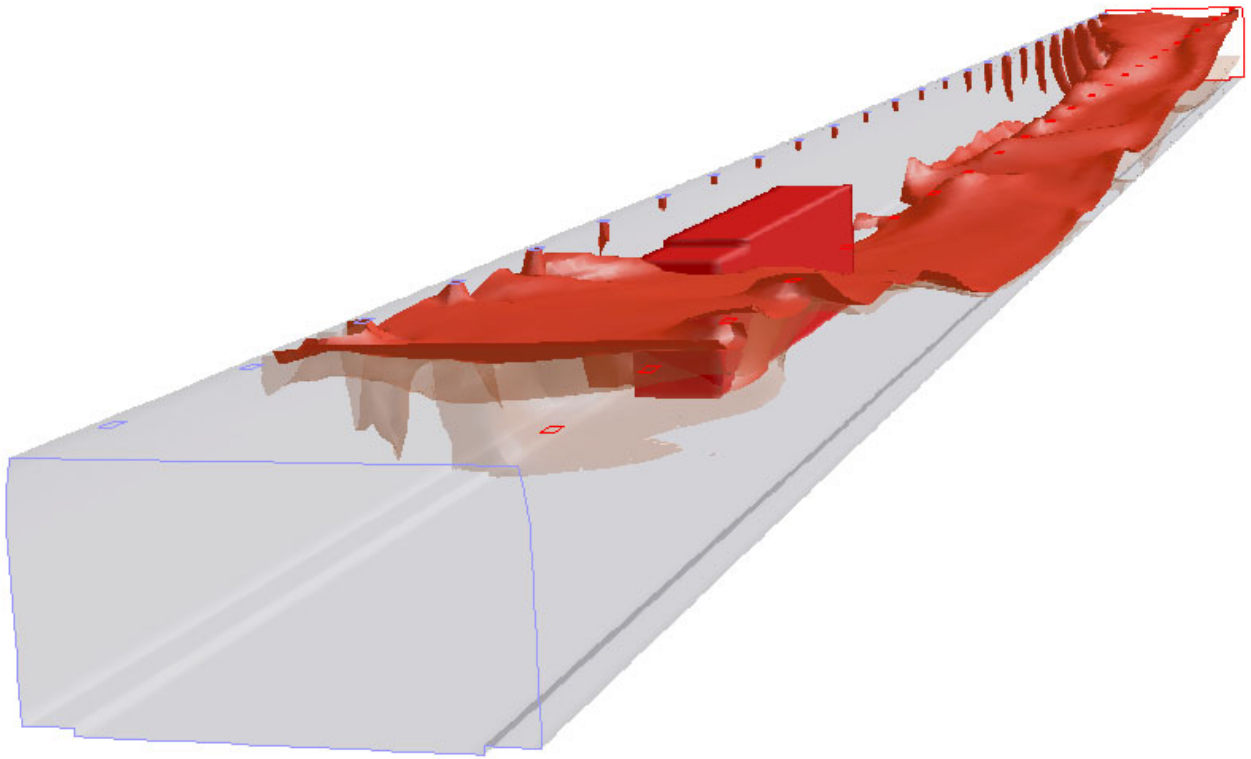

Figure B1.2: *Temperature isosurfaces for 350 [K] and 400 [K] (time=50s)*

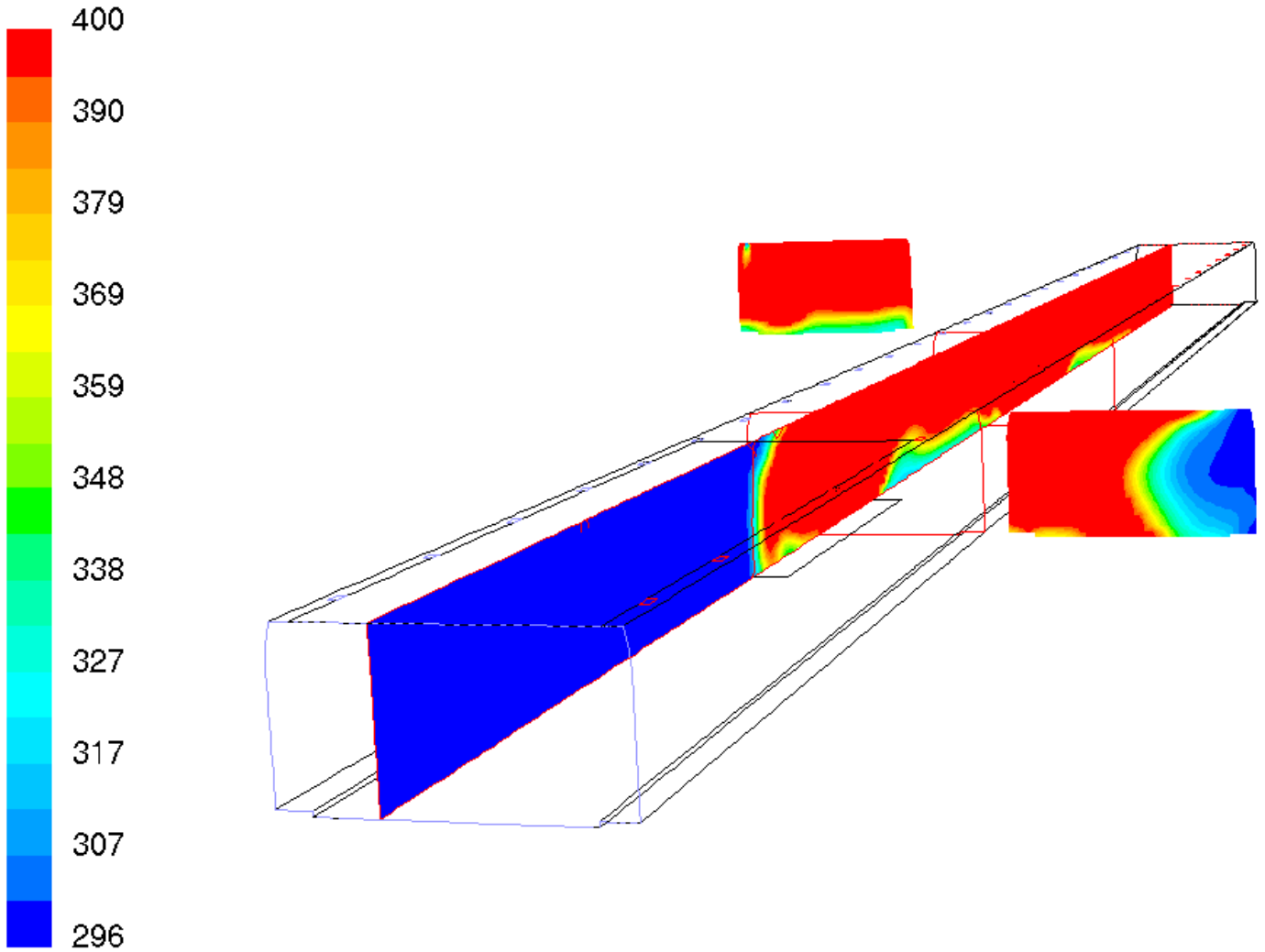

Figure B1.3: *Temperature distribution in different cut planes for scenario B1 (time=100s)*

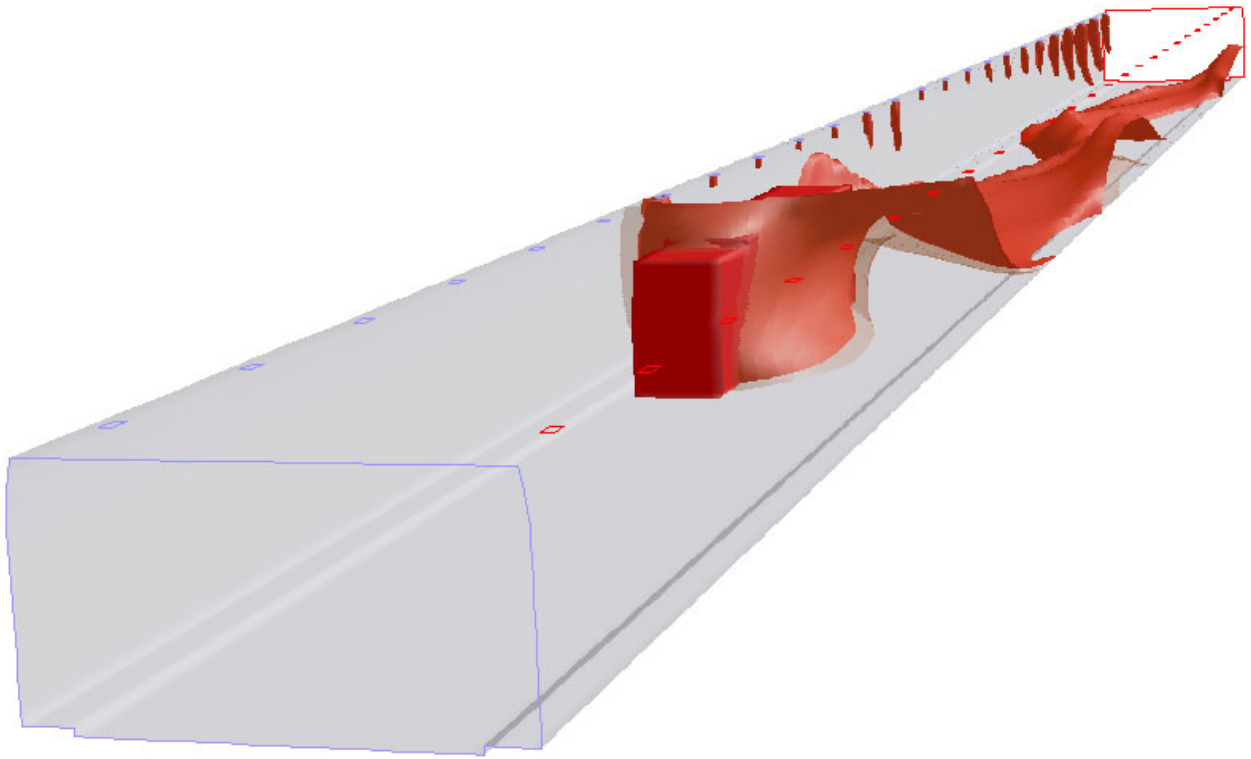

Figure B1.4: *Temperature isosurfaces for 350 [K] and 400 [K] (time=100s)*

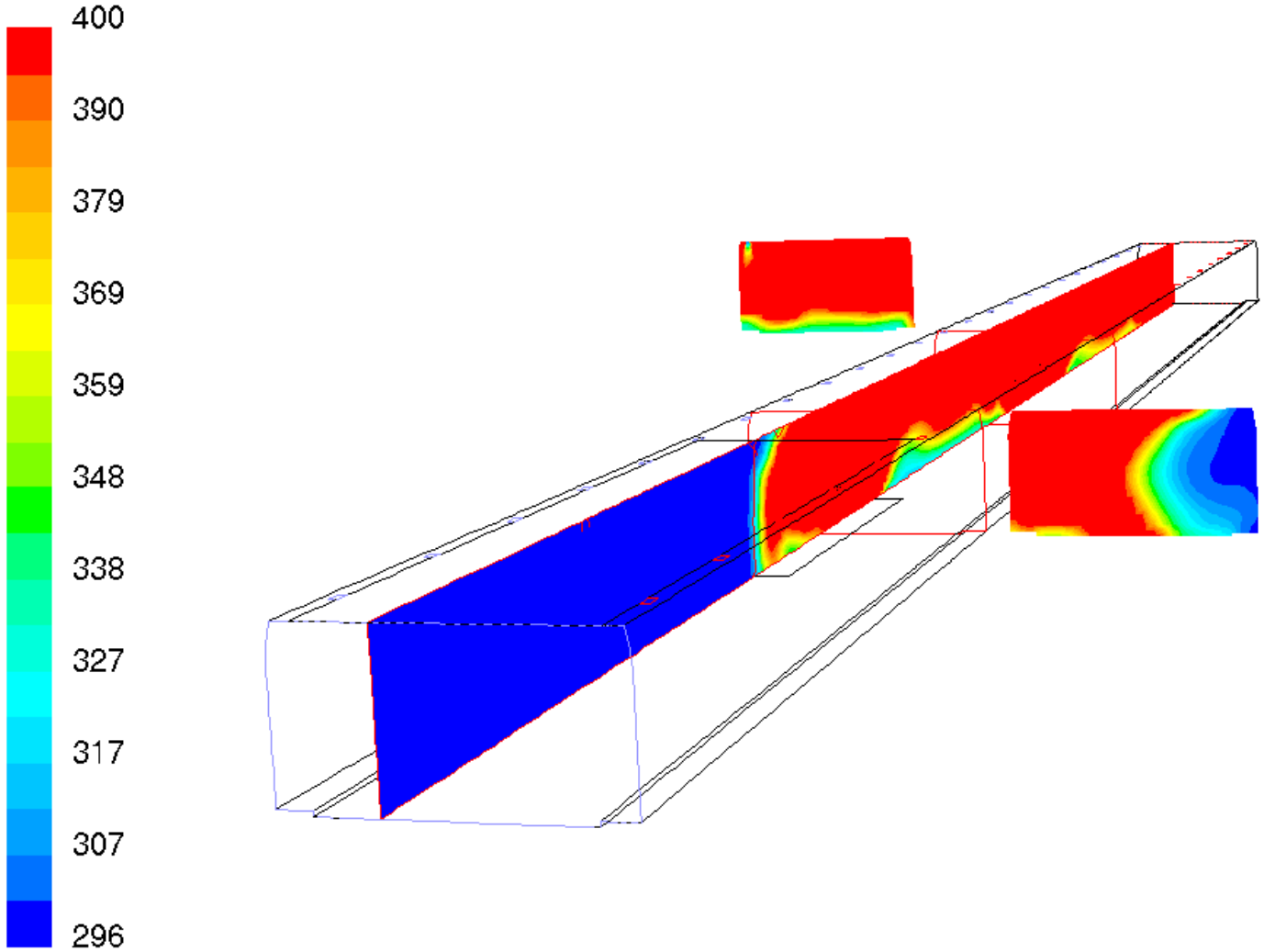

Figure B1.5: *Temperature distribution in different cut planes for scenario B1 (time=200s)*

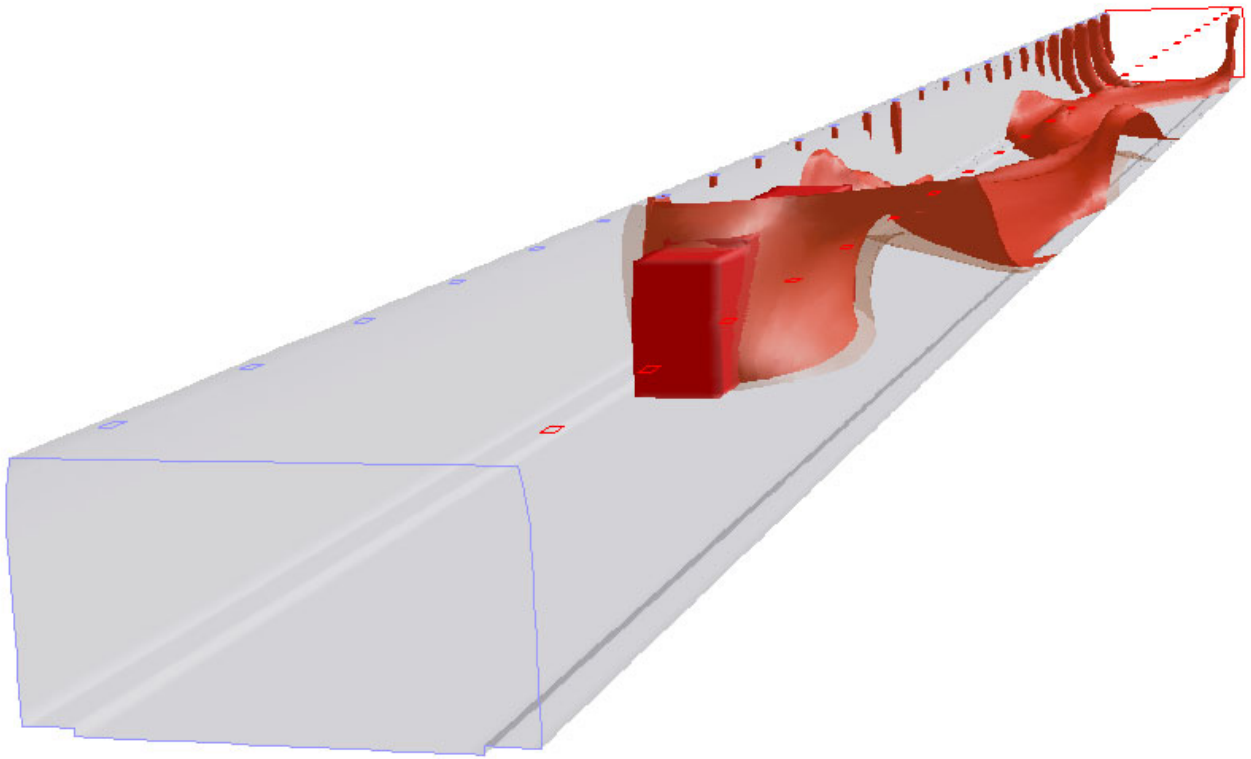

Figure B1.6: *Temperature isosurfaces for 350 [K] and 400 [K] (time=200s)*

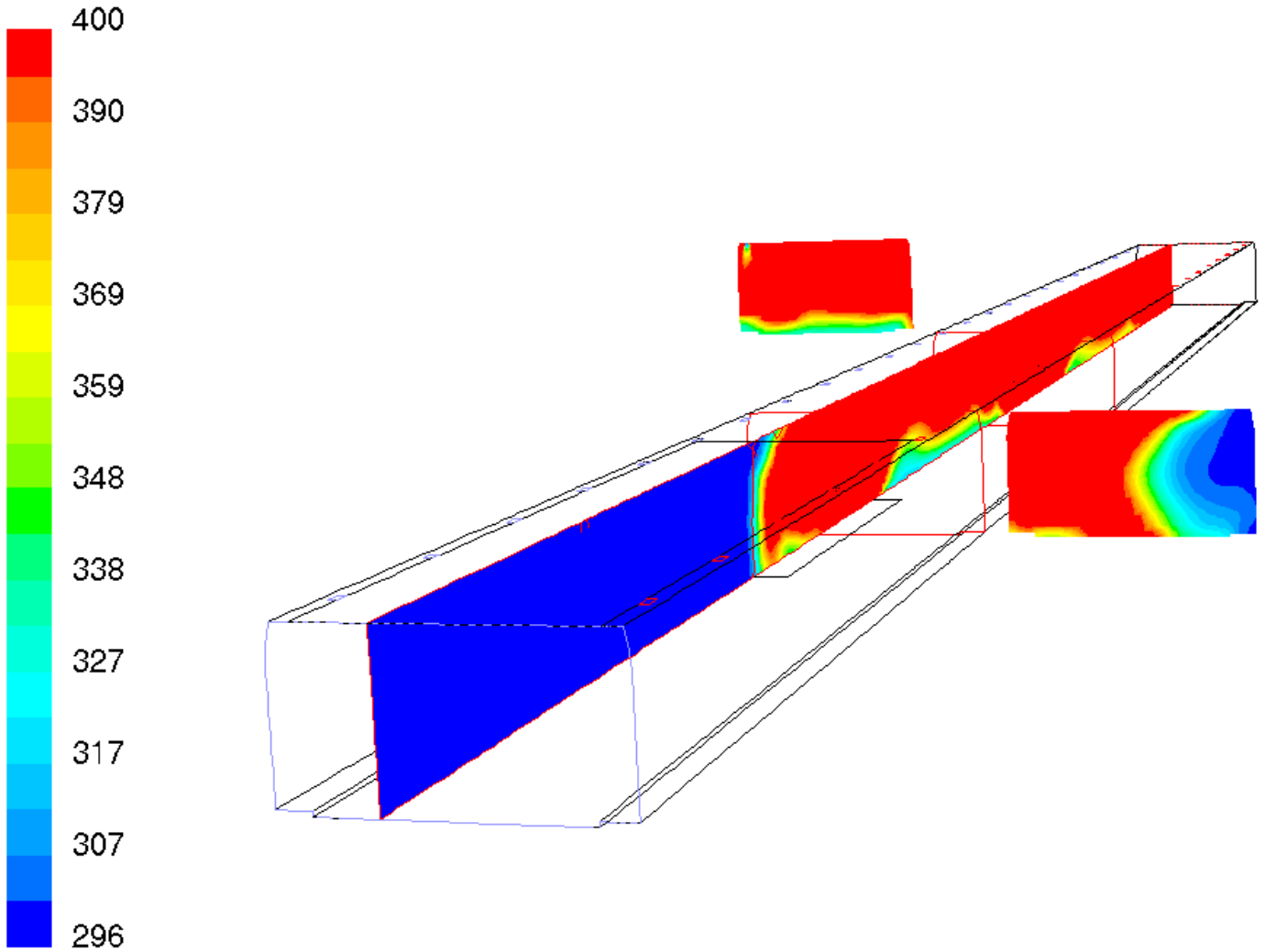

Figure B1.7: *Temperature distribution in different cut planes for scenario B1 (time=300s)*

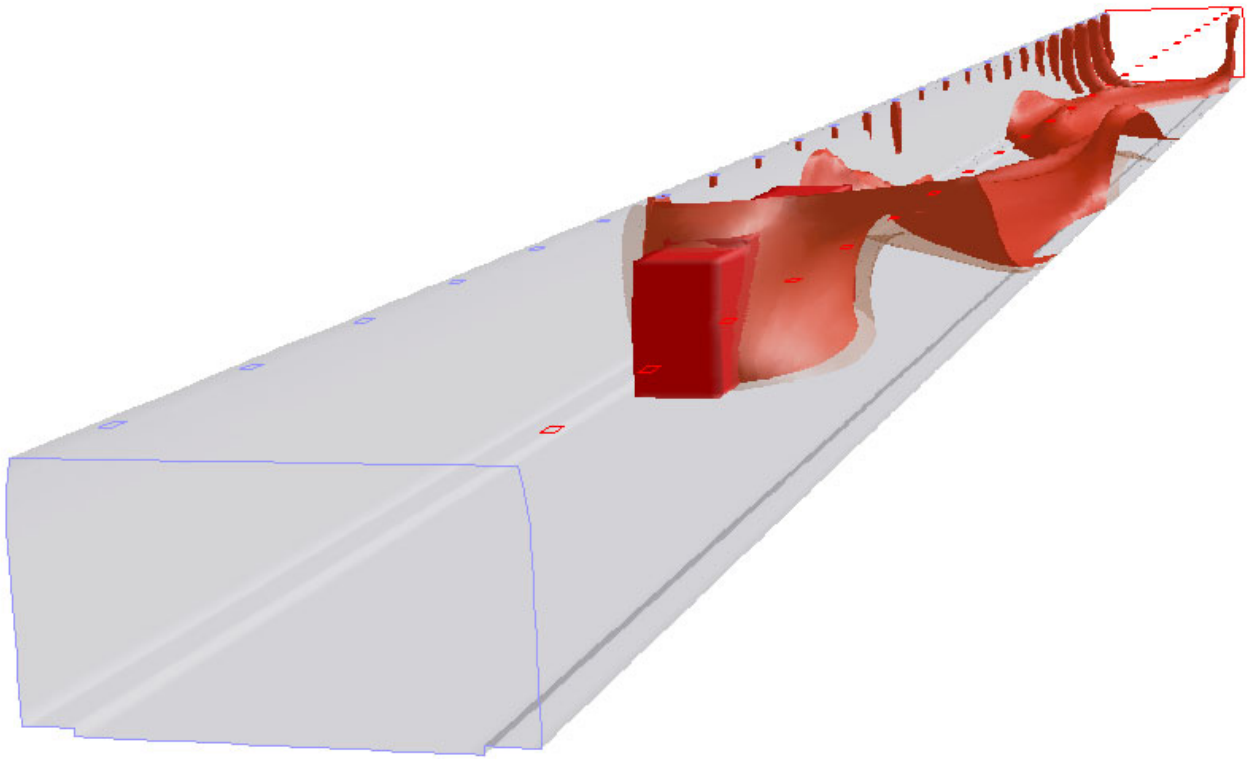

Figure B1.8: *Temperature isosurfaces for 350 [K] and 400 [K] (time=300s)*

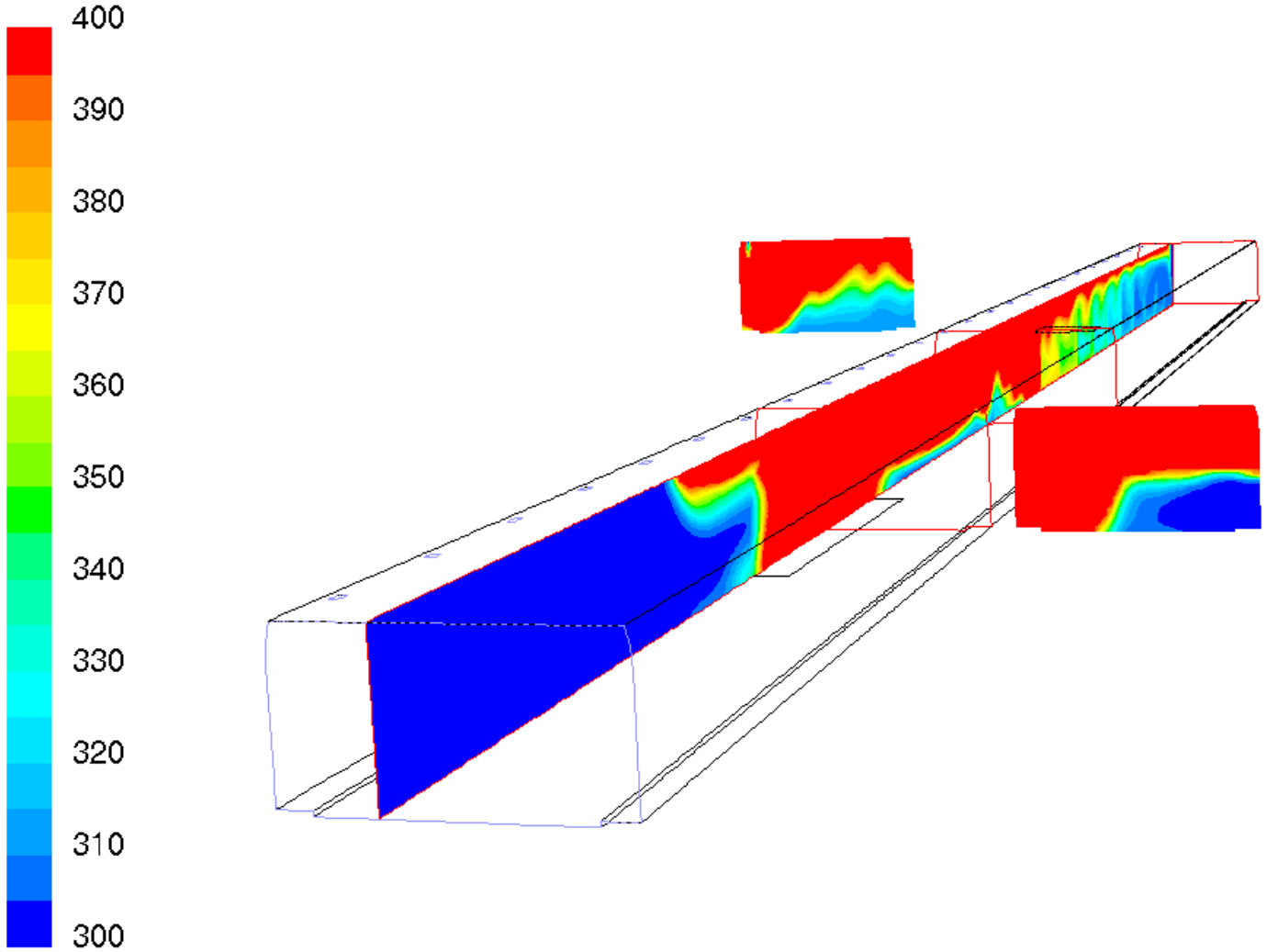

Figure B2.1: *Temperature distribution in different cut planes for scenario B2 (time=50s)*

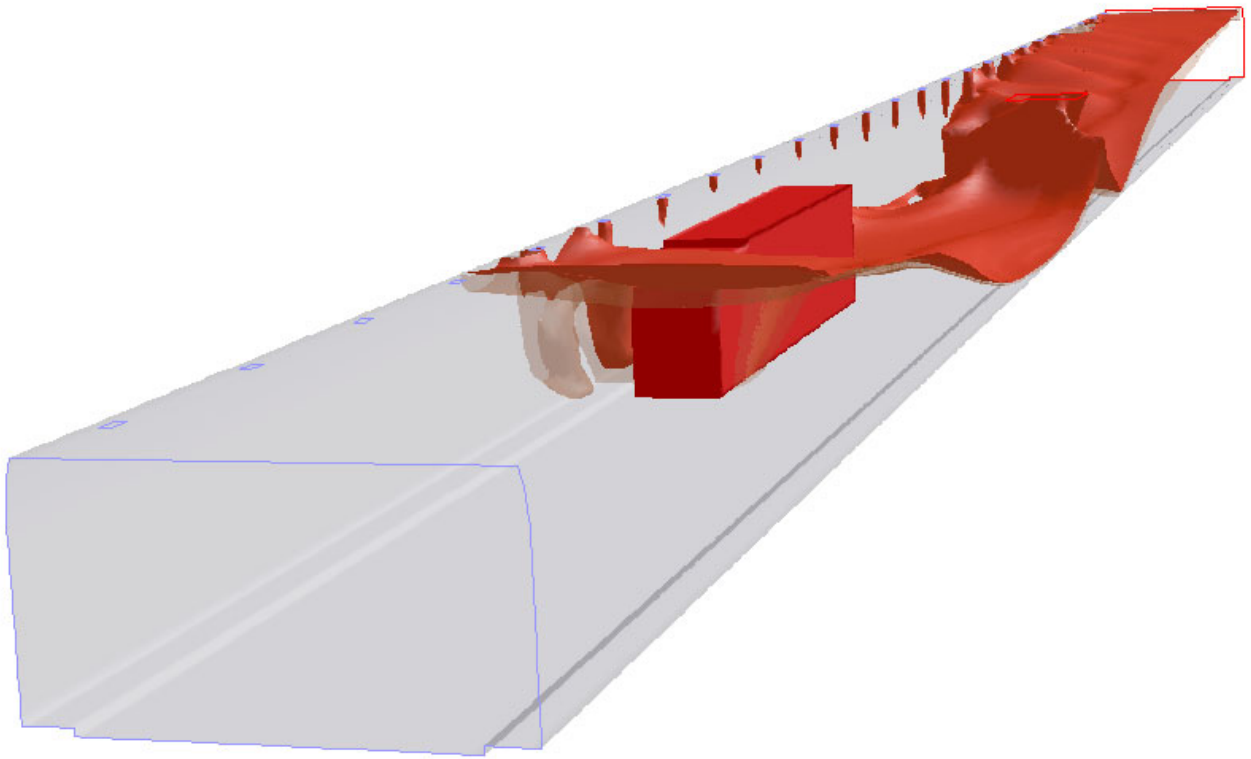

Figure B2.2: *Temperature isosurfaces for 350 [K] and 400 [K] (time=50s)*

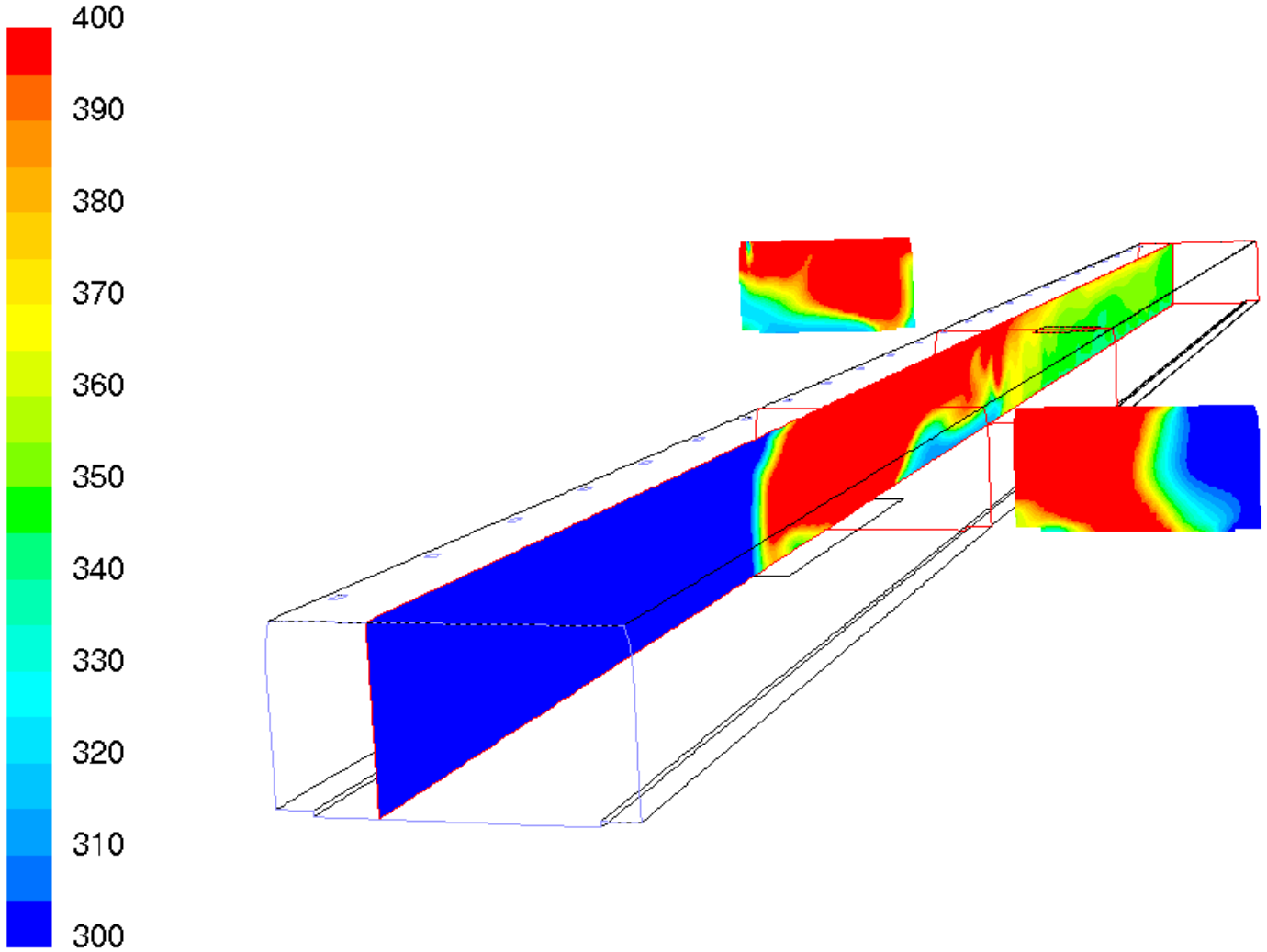

Figure B2.3: *Temperature distribution in different cut planes for scenario B2 (time=100s)*

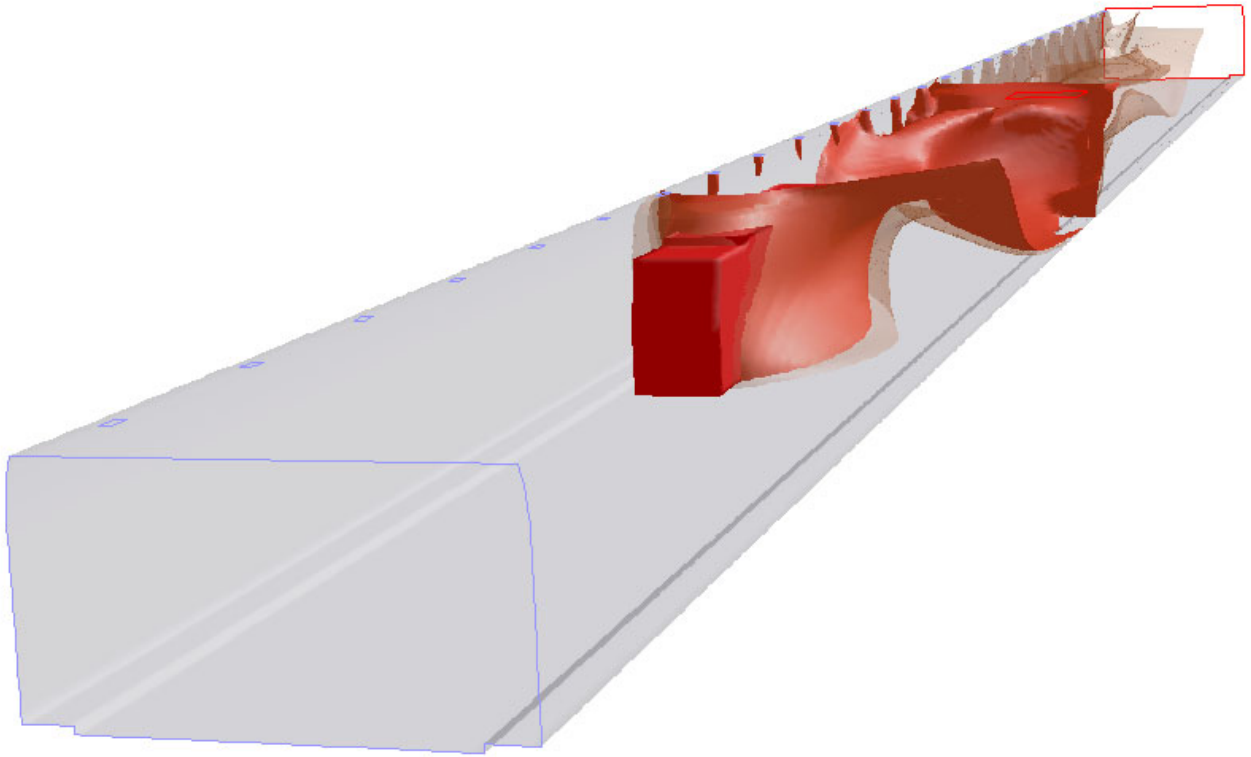

Figure B2.4: *Temperature isosurfaces for 350 [K] and 400 [K] (time=100s)*

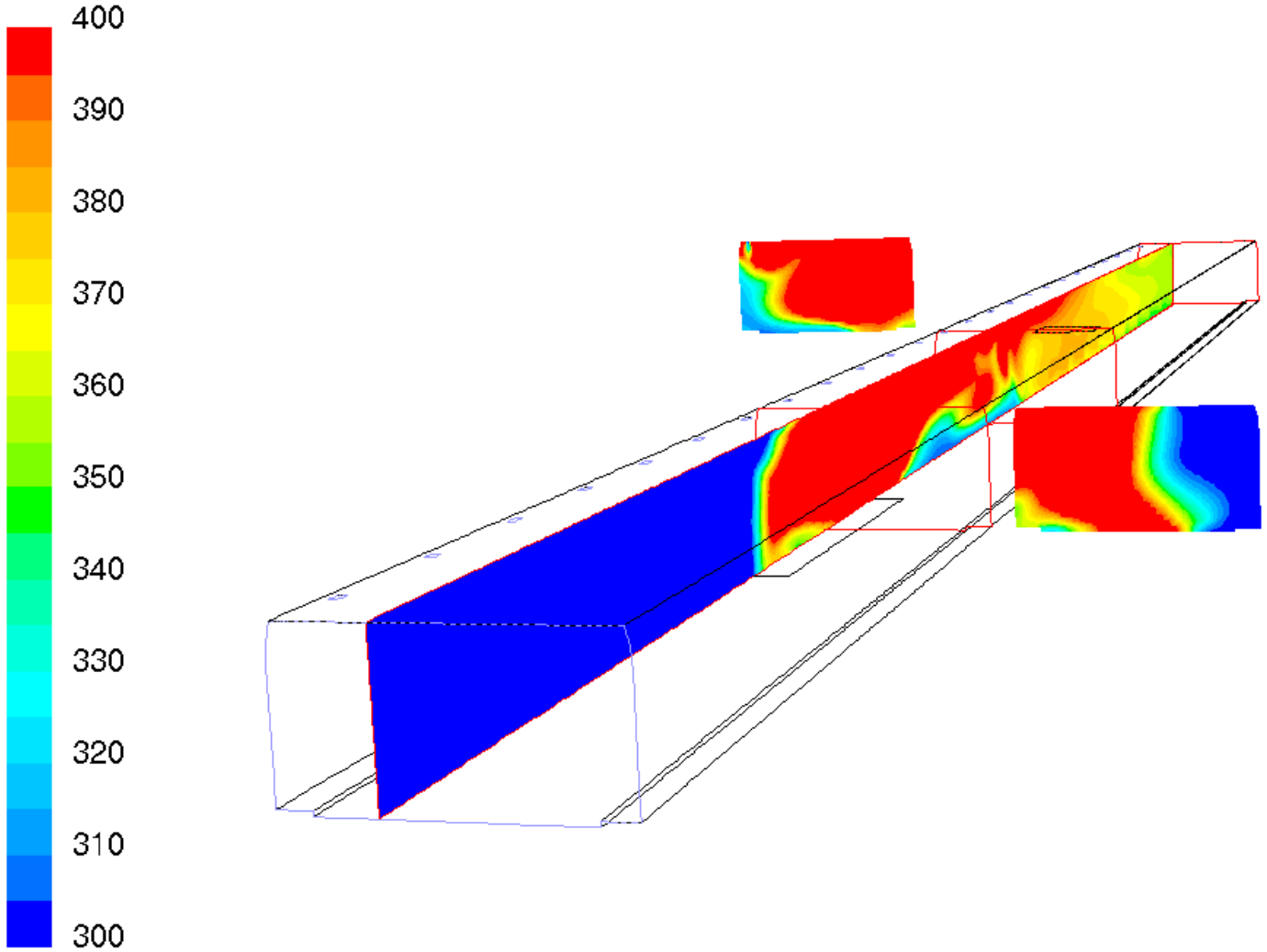

Figure B2.5: *Temperature distribution in different cut planes for scenario B2 (time=200s)*

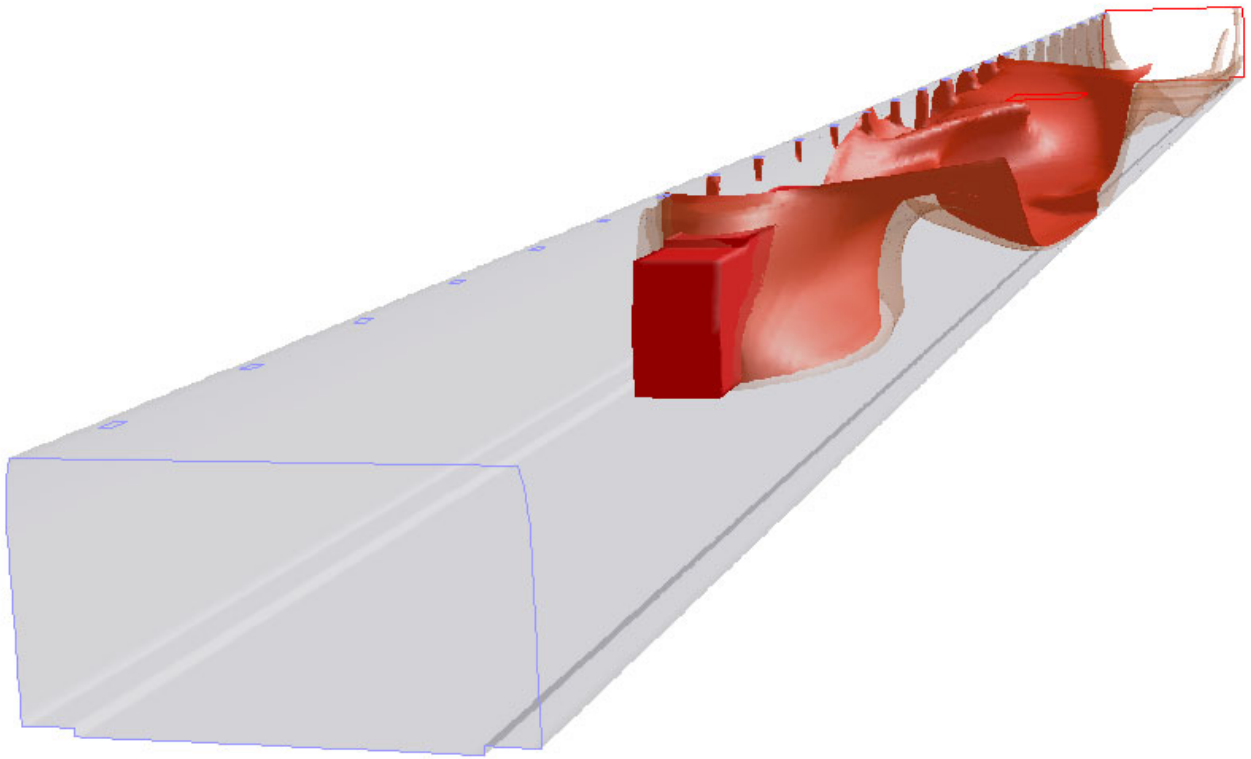

Figure B2.6: *Temperature isosurfaces for 350 [K] and 400 [K] (time=200s)*

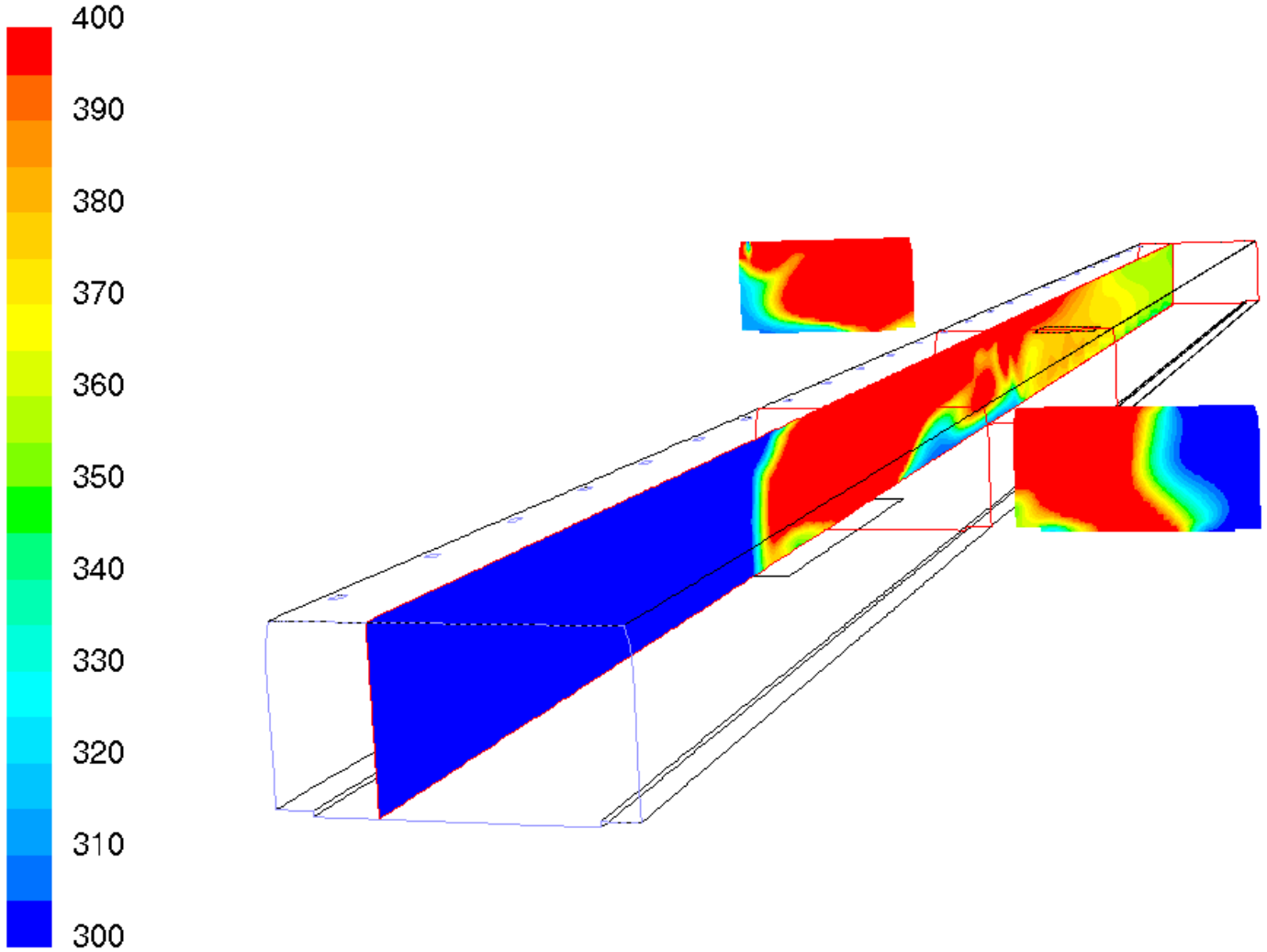

Figure B2.7: *Temperature distribution in different cut planes for scenario B2 (time=300s)*

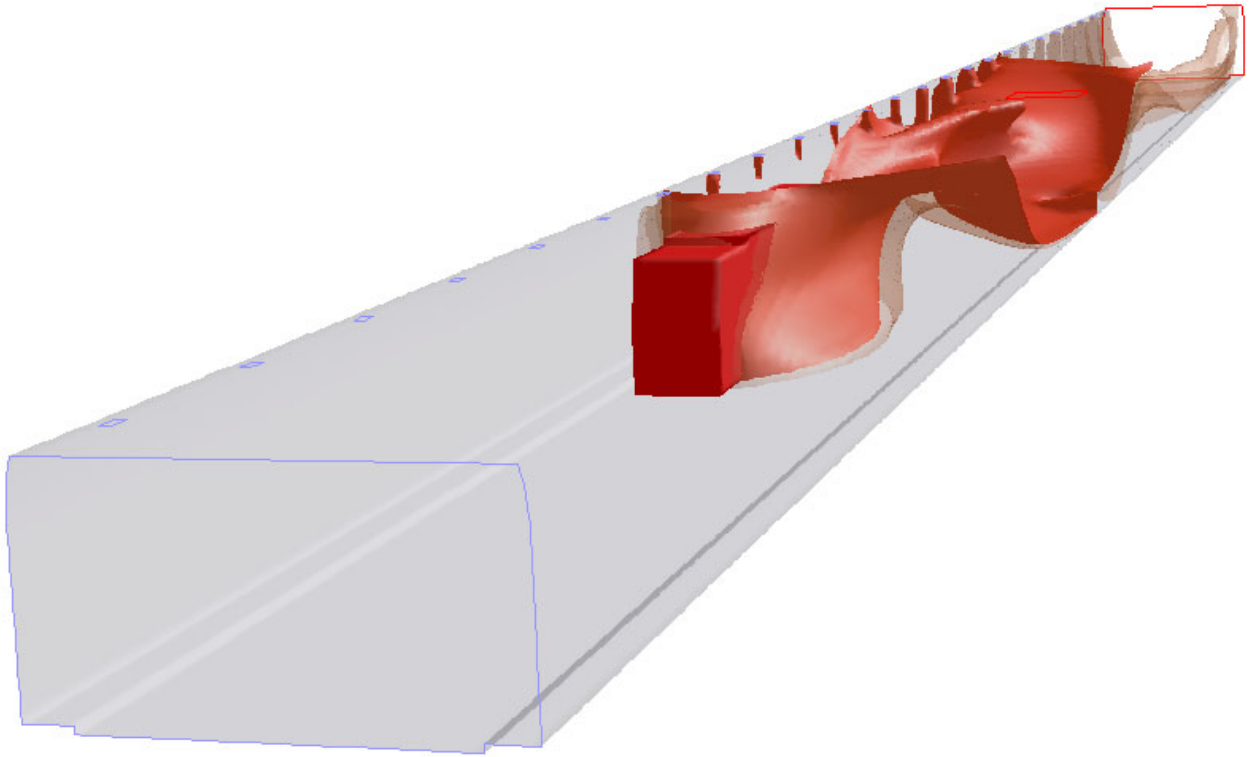

Figure B2.8: *Temperature isosurfaces for 350 [K] and 400 [K] (time=300s)*

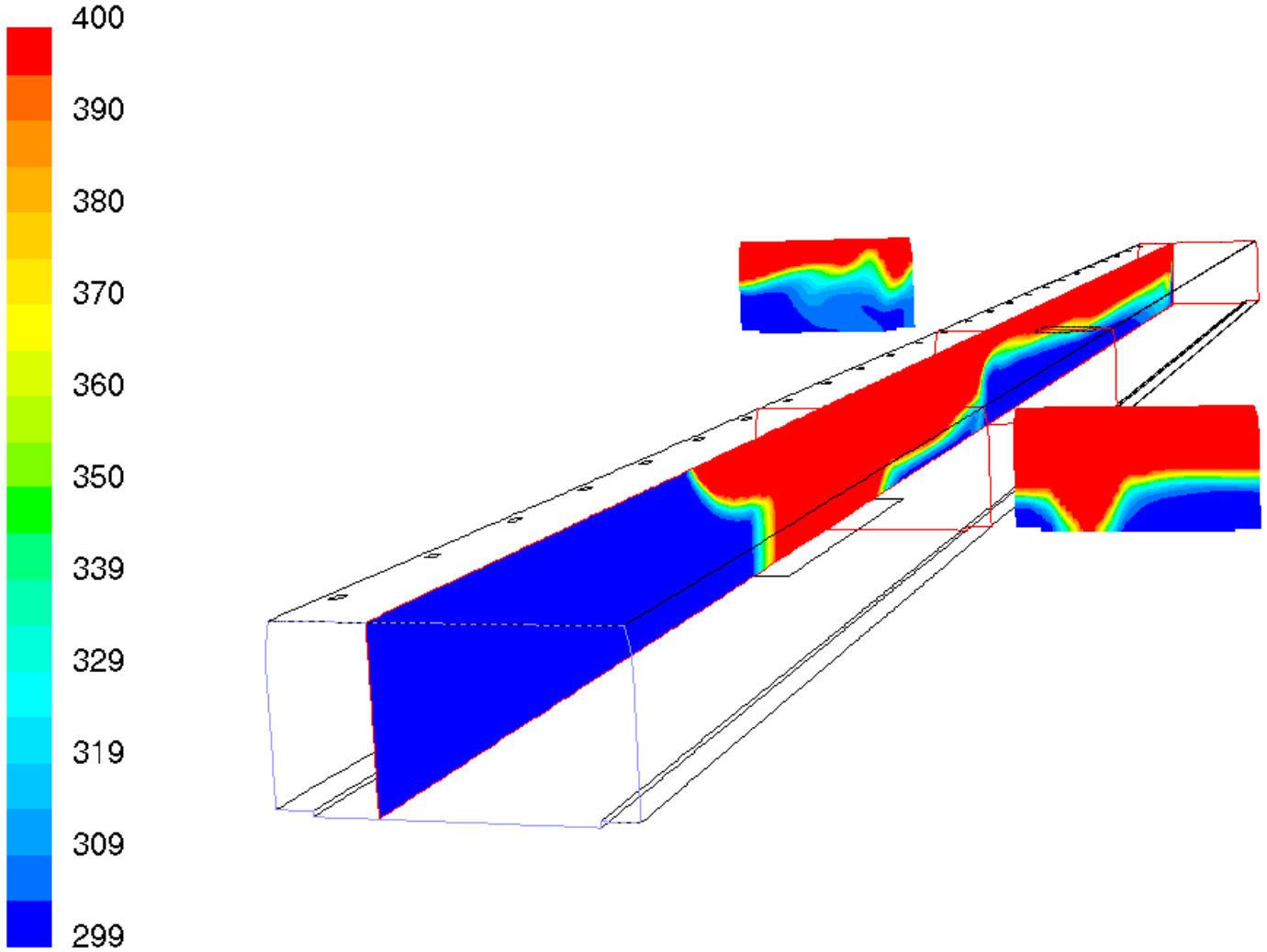

Figure B3.1: *Temperature distribution in different cut planes for scenario B3 (time=50s)*

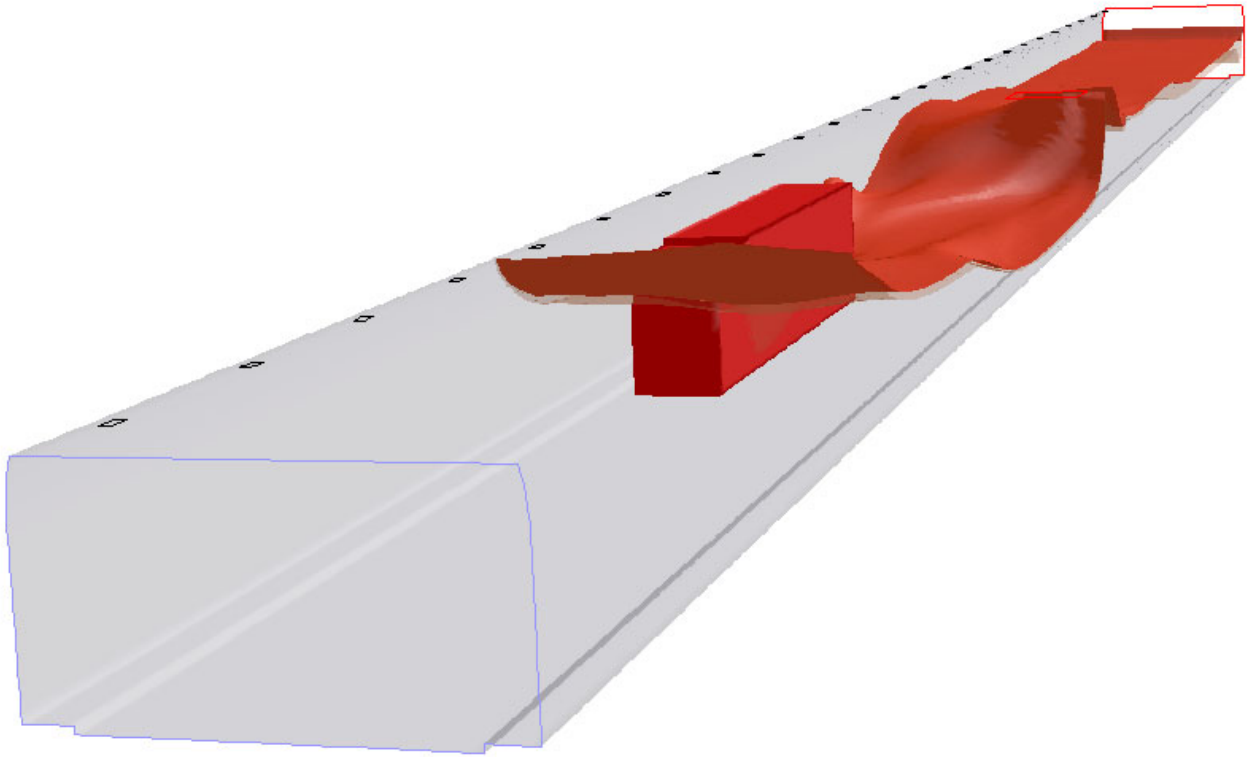

Figure B3.2: *Temperature isosurfaces for 350 [K] and 400 [K] (time=50s)*

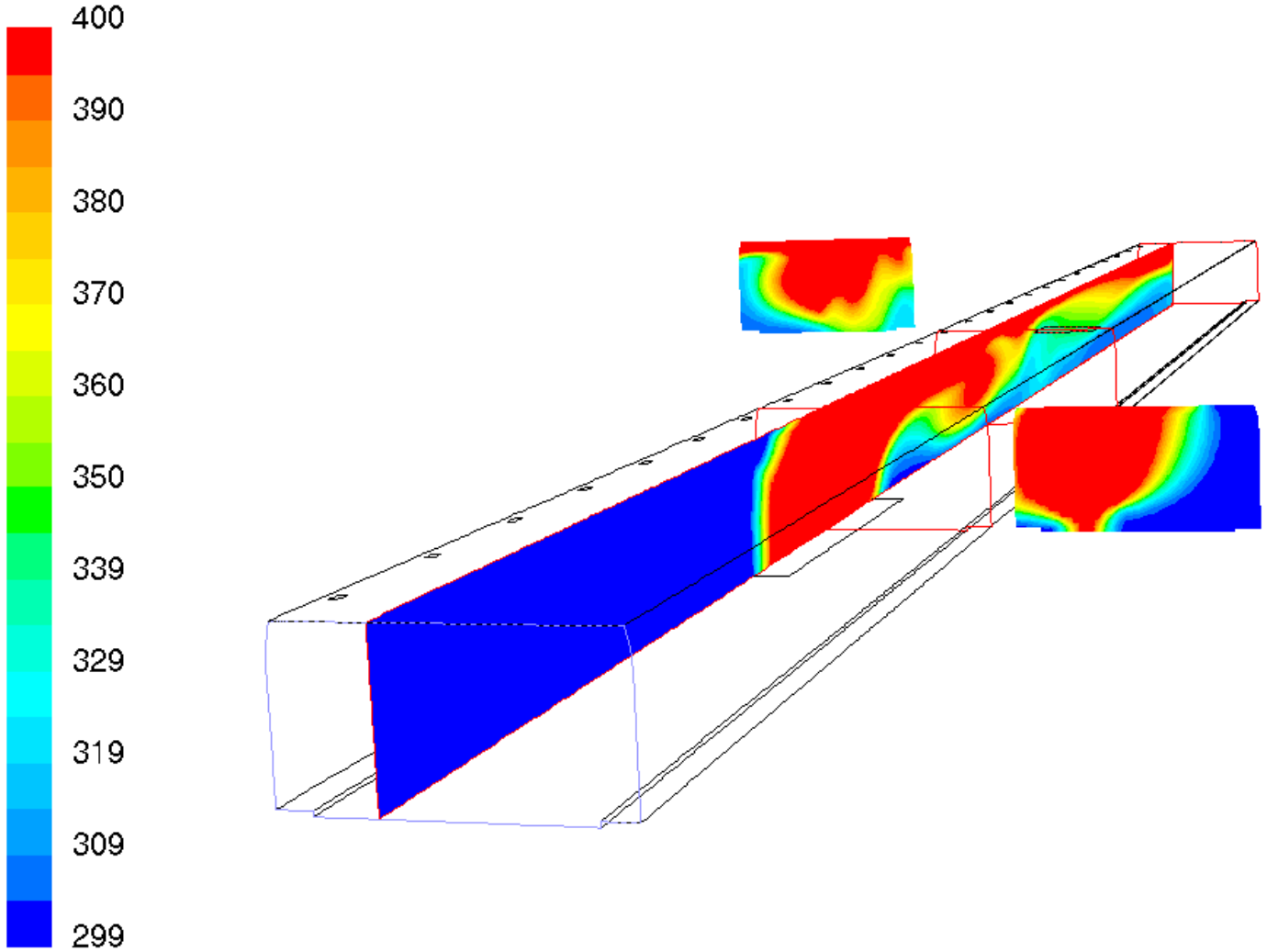

Figure B3.3: *Temperature distribution in different cut planes for scenario B3 (time=100s)*

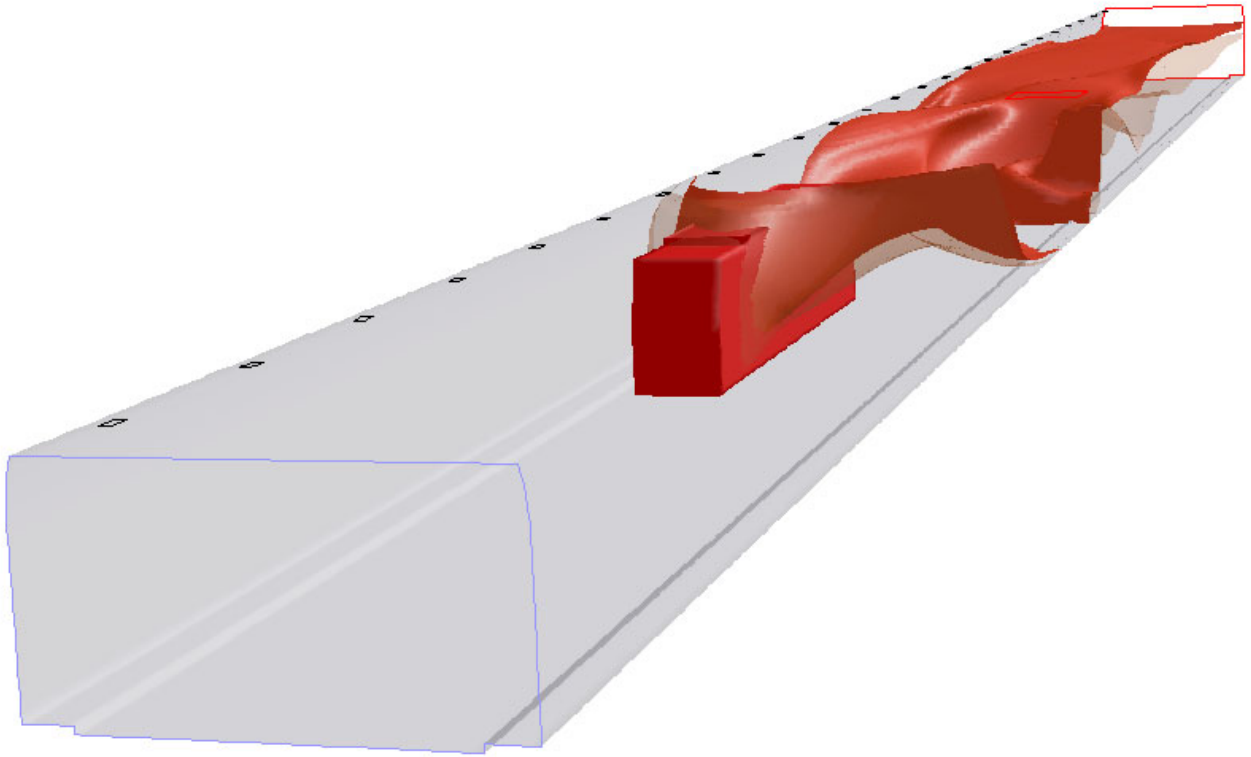

Figure B3.4: *Temperature isosurfaces for 350 [K] and 400 [K] (time=100s)*

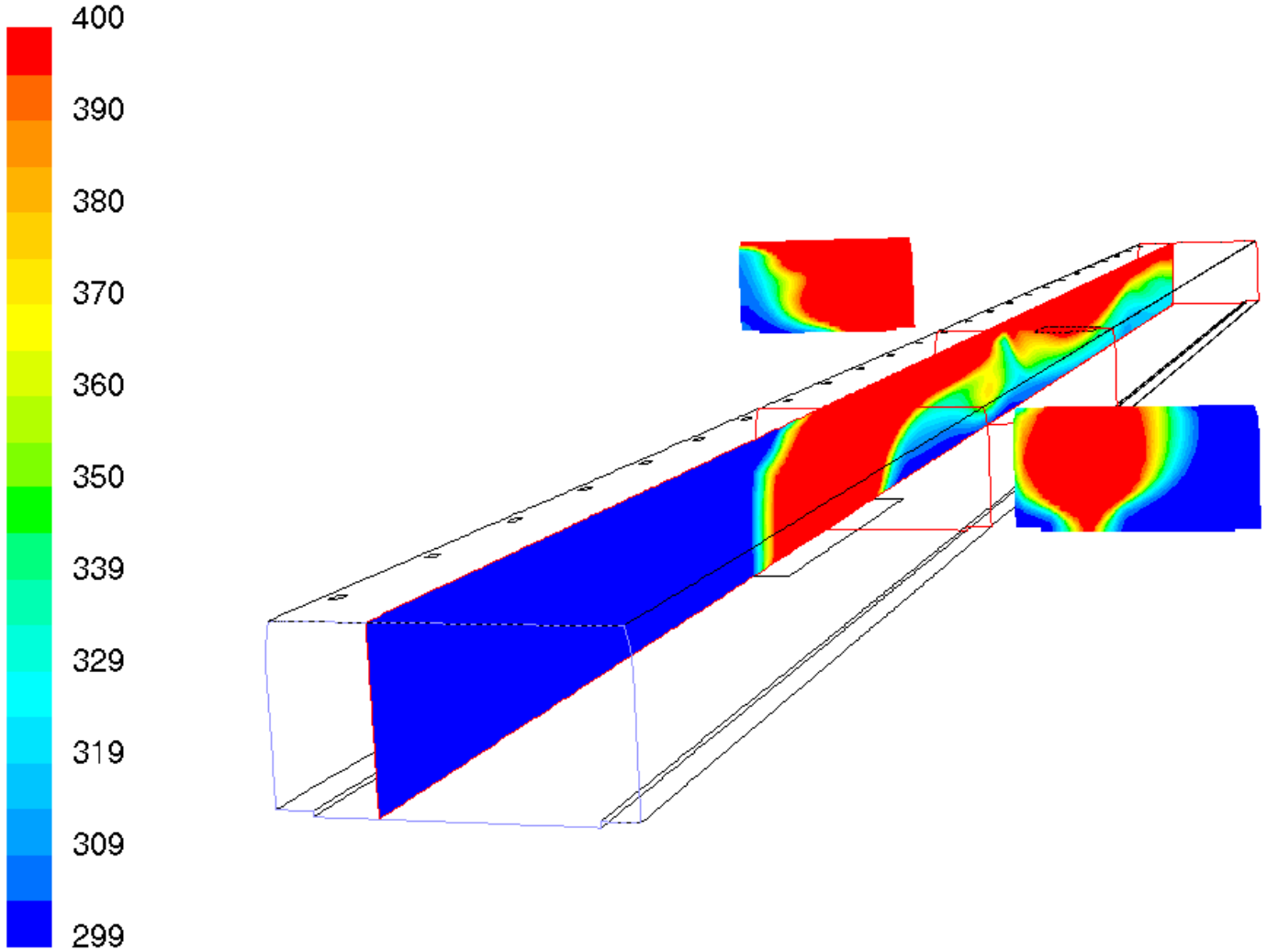

Figure B3.5: *Temperature distribution in different cut planes for scenario B3 (time=200s)*

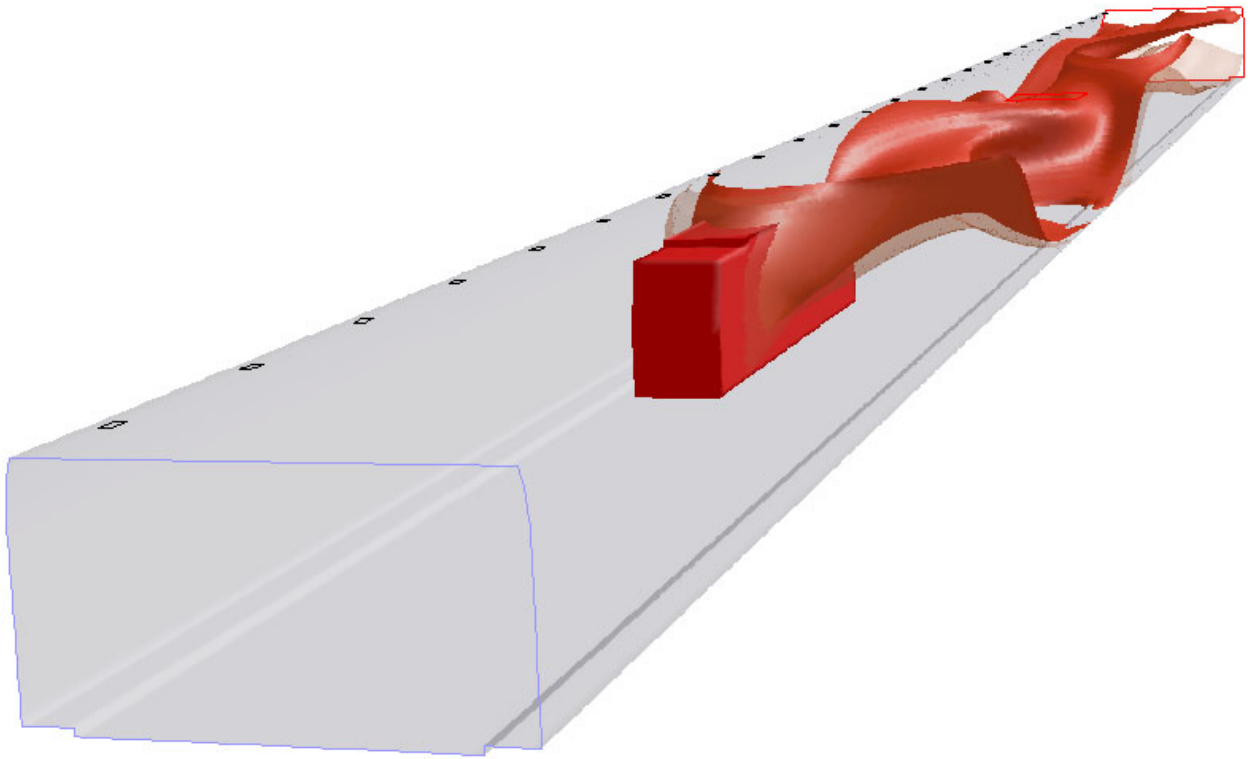

Figure B3.6: *Temperature isosurfaces for 350 [K] and 400 [K] (time=200s)*

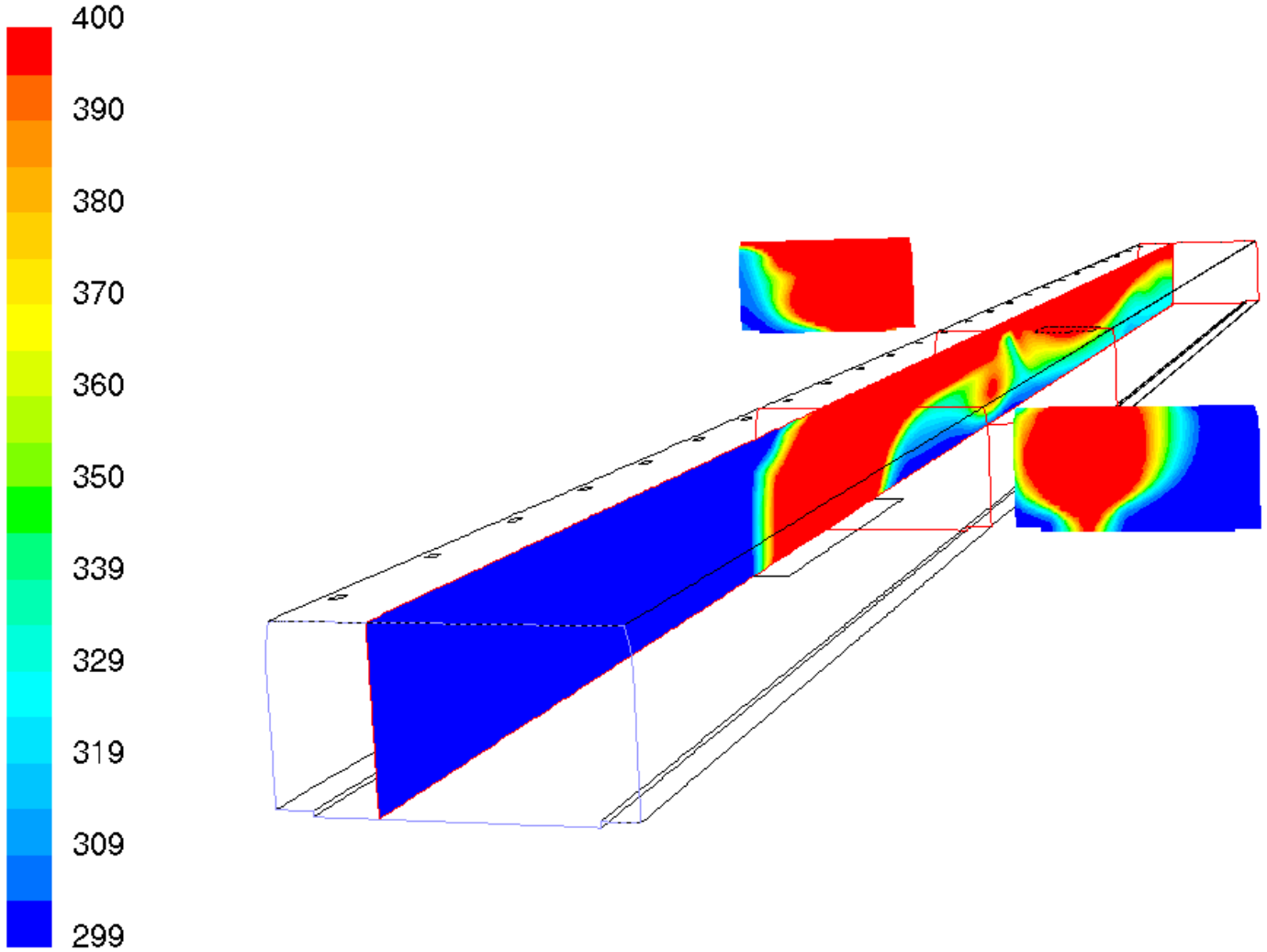

Figure B3.7: *Temperature distribution in different cut planes for scenario B3 (time=300s)*

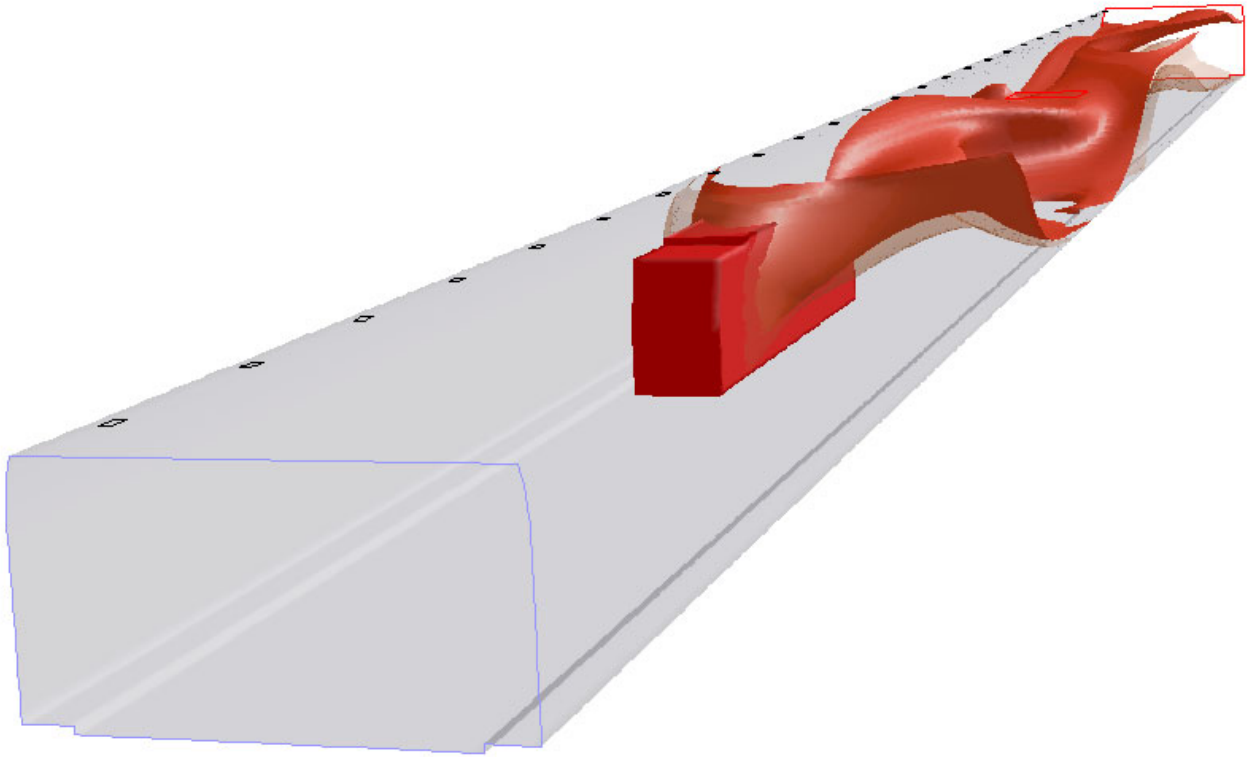

Figure B3.8: *Temperature isosurfaces for 350 [K] and 400 [K] (time=300s)*